Journal of Materials Chemistry A

ROYAL SOCIETY OF CHEMISTRY

REVIEW

View Article Online
View Journal | View Issue

Cite this: J. Mater. Chem. A, 2021, 9, 111

C-, N-Vacancy defect engineered polymeric carbon nitride towards photocatalysis: viewpoints and challenges

Abhinandan Kumar,[a] Pankaj Raizada,*[a] Ahmad Hosseini-Bandegharaei,[bc] Vijay Kumar Thakur,[d] Van-Huy Nguyen *[e] and Pardeep Singh*[a]

As an alluring metal-free polymeric semiconductor material, graphite-like carbon nitride (g-C_3N_4; abbreviated as GCN) has triggered a new impetus in the field of photocatalysis, mainly favoured from its fascinating physicochemical and photoelectronic structural features. However, certain inherent drawbacks, involving rapid reassembly of photocarriers, low specific surface area and insufficient optical absorption, limit the wide-range applicability of GCN. Generation of 0D point defects mainly by introducing vacancies (C and/or N) into the framework of GCN has spurred extensive consideration owing to their distinctive qualities to manoeuvre substantially, the optical absorption, radiative carrier isolation, and surface photoreactions. The present review endeavours to summarise a comprehensive study on vacancy defect engineered GCN. Starting from the basic introduction of defects and C/N vacancy modulated GCN, numerous advanced strategies for the controlled designing of vacancy rich GCN have been explored and discussed. Afterwards, light was thrown on the various substantial technologies which are useful for characterising and identifying the introduction of defects in GCN. The salient significance of defect engineering in GCN has been reviewed concerning its impact on optical absorption, charge isolation and surface photoreaction ability. Typically, the achievement of defect engineered GCN has been scrutinised toward various applications like photocatalytic water splitting, CO_2 conversion, N_2 fixation, pollutant degradation, and H_2O_2 production. Finally, the review ends with conclusions and vouchsafing future challenges and opportunities on the intriguing and emerging area of vacancy defect engineered GCN photocatalysts.

Received 26th August 2020
Accepted 19th November 2020

DOI: 10.1039/d0ta08384d

rsc.li/materials-a

1. Introduction

The rapid deterioration of fossil-fuel assisted energy resources with rising pollution levels, and drastic climate changes have intensified the insistence on exploiting advanced technologies for environmental restoration and alternate energy sources.[1–3] The ever-growing acceptance and appreciation of solar energy as an inexhaustible, renewable and clean energy source, and in solar light-driven energy conversion applications and pollutant mitigation is in the spotlight. Currently, one of the most intriguing solar light assisted applications is "Photocatalysis". In photocatalysis, the energy conversion phenomenon is carried out with semiconductor materials utilizing the synergistic effect of light photons and catalyst.[4,5] Photocatalysis is a rising green technology employed for the effective removal of effluents from wastewater and the generation of ideal hydrogen energy from water and sunlight.[6–8] The semiconductor photocatalysis is initiated with the absorption of solar light and subsequent production of photocarriers (electrons (e^-) and holes (h^+)). Hence, an efficient photocatalyst must possess enhanced photo-absorption range and superior isolation ability of photo-illuminated carriers.[9–12] However, many semiconductor photocatalysts suffer from low photo-efficiency and significantly high recombination of photocarriers, which severely hinder the overall quantum efficacy along with wide-scale applicability of photocatalysis.[13–17]

To boost the photoactivity of semiconductor photocatalysts, numerous strategies like structural modifications, morphology control, surface and interface engineering, and facet and defect engineering have been widely opted and recruited.[18–21] Out of all these strategies, defect engineering is an important strategy to design efficient photocatalysts.[22] Defects are usually classified based on the atomic structure of the defects or the effective position of defects in photocatalysts. Generally, based on

[a]School of Advanced Chemical Sciences, Shoolini University, Solan, HP, India, 173229. E-mail: pardeepchem@gmail.com; pankajchem1@gmail.com

[b]Department of Environmental Health Engineering, Faculty of Health, Sabzevar University of Medical Sciences, Sabzevar, Iran

[c]Department of Engineering, Islamic Azad University, Kashmar Branch, P.O. Box 161, Kashmar, Iran

[d]Biorefining and Advanced Materials Research Centre, Scotland's Rural College (SRUC), Edinburgh, UK

[e]Institute of Research and Development, Duy Tan University, Da Nang 550000, Vietnam. E-mail: nguyenvanhuy20@duytan.edu.vn

dimensionality, a semiconductor photocatalyst can be induced with (i) 0D point defects like heteroatom doping and vacancy generation, (ii) 1D line defects like screw and edge modulations, (iii) 2D planar defects like twin and grain boundaries and (iv) volume defects involving disorder in lattice or void generation as shown in Fig. 1a.[23] Comparatively, 0D point defects can be easily induced in a semiconductor photocatalyst without altering its structure to a large extent.[24] Moreover, point defects are also helpful to boost the conductivity of the semiconductor material by controlling the non-stoichiometric compositions unlike line or planar defects, which have a negligible effect on stoichiometry. Also, by the generation of voids and introducing

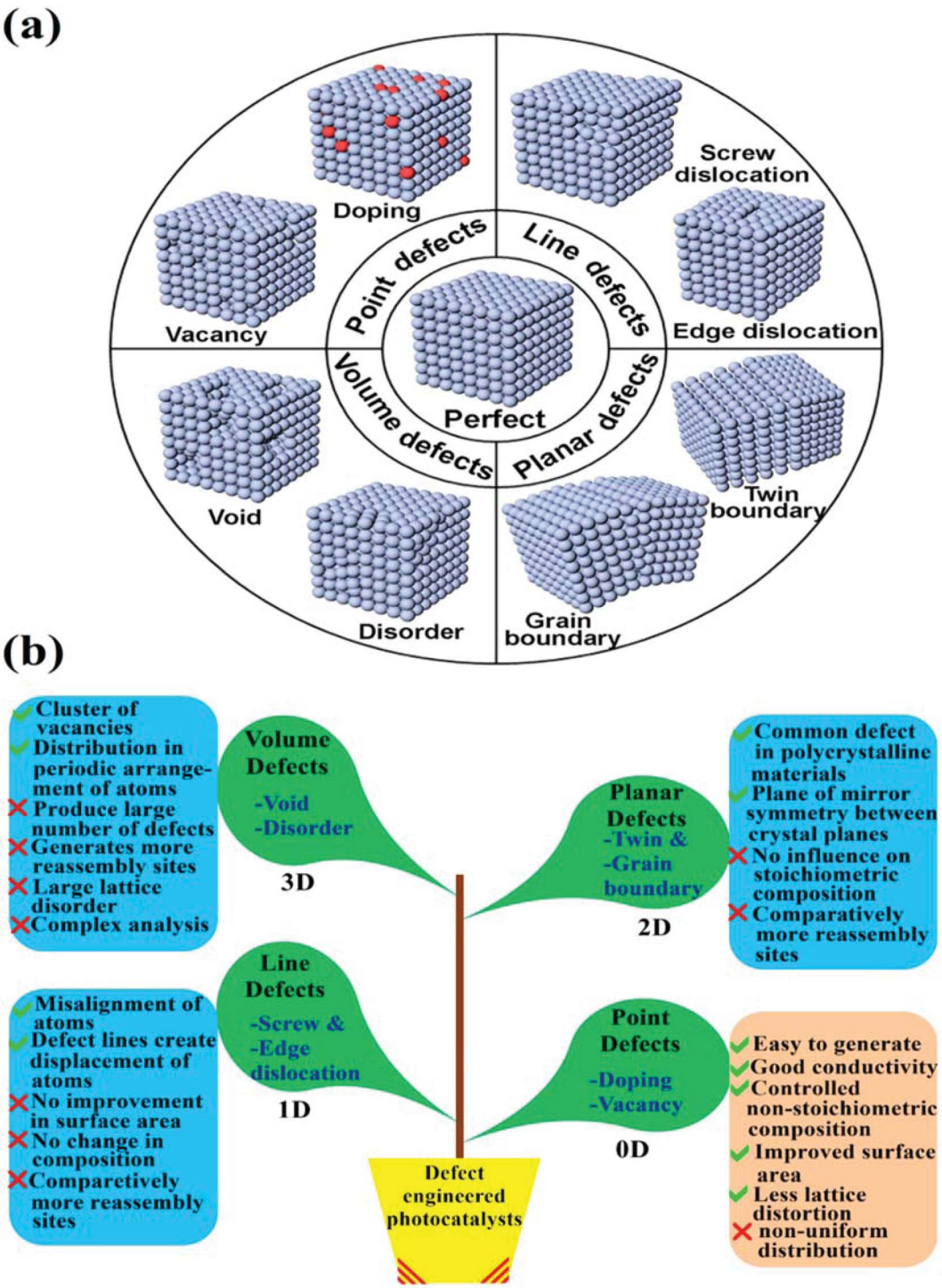

Fig. 1 (a) Schematic illustrating the types of common defects in photocatalysts based on dimensionality (adapted with permission under license no. 4840040907271, Copyright 2018 Elsevier).[23] (b) Diagrammatic representation of various advantages and disadvantages associated with different types of defect engineered photocatalysts.

disorder in the structural motifs of any photocatalyst, the probability of e^-–h^+ recombination sites increases substantially, resulting in deprived photocatalytic activity. Other than that, the lattice defects involving dislocations and distortions have a significant effect on the electronic configuration and physicochemical properties of the photocatalyst. On this account, dislocations and distortions can usually be created in 2D crystalline materials to stabilise the structure by reducing surface energy.[25] However, the surface distortion phenomenon has a notable effect on local atomic arrangements, including the bond angle, bond length, several coordinated atoms and interatomic distance and their generation in the crystal structure leading to the formation of atomic level vacancies.[26] Fig. 1b depicts certain advantages and disadvantages associated with various defects in a photocatalytic material. As a consequence, a comprehensive study of point defects is crucial for further exploration as well as for a better understanding of defect engineering involving line defects, planar defects and volume defects in semiconductor materials. Up to now, enormous research efforts have depicted the positive influence of 0D point defects (specifically vacancy generation) on overall photoactivity.[22,23,27,28]

Depending upon the loss of ions from the photocatalysts, vacancies generated can be categorised as anion vacancies, cation vacancies, and multiple vacancies. Generally, defect generation through anion vacancies by removing O, S, and N is common in semiconductor materials because of less formation energy.[23,29] Anion vacancies exert a positive influence on photocatalytic activity by modifying band alignments, electronic behaviour, and active surface sites on photocatalysts. By inducing an anion vacancy in a semiconductor photocatalyst, the bandgap of the pristine photocatalyst is modulated by the introduction of mid-gap states which extends the absorption of light by narrowing the bandgap energy. Therefore, anion vacancies are much more impactful to alter the bandgap energy of semiconductor materials. On the other hand, owing to fascinating features, generation of cation vacancies in photocatalysts is greatly appreciated by researchers.[30,31] Generation of cation vacancies can be extremely significant due to its ability to provide certain characteristic properties to photocatalysts. Of note, to introduce cation vacancies in any photocatalyst comparatively high energy and stability is required. There are several reports which depict cation vacancies in TiO_2 and ZnO by the removal of Ti^{4+} and Zn^{2+}, respectively.[32,33] Generally, monoatomic vacancies (cation/anion vacancies) are common and can be induced easily, but there are reports considering multi-defect engineered semiconductor substances which have been created by generating cation and anion vacancies simultaneously.[34,35] In such cases, the construction of anion and cation vacancies in a photocatalyst often leads to the formation of the p–n homojunction which causes superior exciton dissociation under the influence of a built-in field at the interface.[36] Consequently, construction of vacancy rich semiconductor photocatalysts seems to be an effective approach to simultaneously foster the isolation of charge carriers and increase the overall photoactivity.

Among photocatalytic materials, metal-free photocatalysts were significantly exploited due to their exceptional physicochemical stability and economic features in contrast with conventional oxides and sulphides. To date, numerous metal-free semiconductor materials involving heptazine-based polymeric melon (usually called carbon nitride (g-C_3N_4); will be referred to as GCN), elemental sulphur and phosphorus, and boron have been substantially explored.[37–40] However, the elemental semiconductor materials do not show much stability in the photocatalytic reaction atmosphere as they get easily oxidised either by sunlight, water or oxygen.[41] This fact severely obstructs their real-time applicability, as the photocatalytic process is carried out in the presence of light and moisture only.[42] Contrarily, GCN offers superior physicochemical stability and has facile tailoring routes utilizing economic precursors, nontoxic nature and appropriate electronic features which render GCN an ideal semiconductor material for diverse photocatalytic applications.[43,44] However, bulk GCN possesses certain inherent limitations like reassembly of surface-induced photocarriers, along with having fewer active surface sites and comparatively narrow bandgaps.[45–47] The modulation of photocatalytic properties includes the controlled alteration of bulk GCN to 2D structures, which substantially obstruct the reassembly procedure at the surface. Besides, structural manipulations like doping, defect engineering, the introduction of functional groups, and tailoring of different heterostructures have also been explored on a wide scale.[48,49]

Out of these strategies, introducing point defects *via* doping and vacancy generation in the structural unit of 2D GCN is a promising strategy for improving the photoactivity of GCN.[50] However, heteroatom doping is accompanied by certain inherent limitations such as (i) it is mainly beneficial to tune the bandgap alignment for amended optical absorption ability, (ii) identifying the spatial distribution of dopants is another crucial issue for effective modification of the electronic structure of the semiconductor photocatalyst and (iii) uniform distribution of heteroatoms throughout the whole structural unit is indispensable for effective bandgap tuning, while surface doping can partly modulate the bandgap by introducing some localised heteroatoms.[51] Thus, it is intriguing to explore the atomic level modification in GCN by C/N vacancy generation as depicted in Fig. 2. Because photocatalytic reactions occur at the surface of a photocatalyst, photoefficiency is greatly influenced by surface properties. Also, the rational creation of surface vacancies can induce lattice disorder, resulting in increased surface energy. Consequently, the as generated vacancies can act as additional reactive sites and catalyse the surface photoreactions more effectively.[52] Besides, exciton dissociation can be promoted by inducing surface vacancy defects due to defective energy state generation around vacant sites.[53] 2D GCN with a layered structure has hydrogen bonds between the strands of melon tectonic units with NH/NH_2 groups in each layer held together with weak van der Waals forces. This layered structural arrangement makes GCN a suitable candidate for the generation of vacancies through appropriate designing techniques. Of note, generally, it is easier to generate defects at edges, less coordinated steps, terraces and at corner atoms.[54] Therefore, controlled C/N-

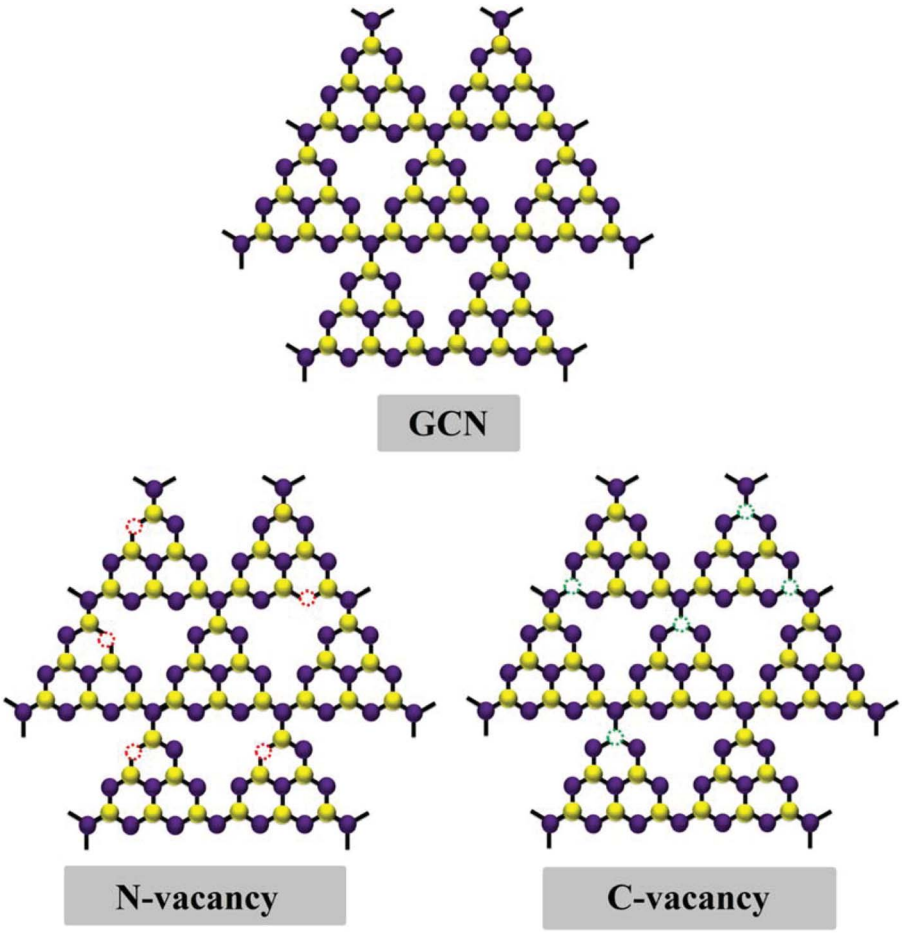

Fig. 2 Diagrammatic representation of GCN (above) and vacancy induced GCN sheets.

vacancy defects can be facilely generated in GCN by altering some in-plane triazine units without damaging the whole structure. For instance, Ren *et al.* illustrated the efficient role and the effective site for generating N-vacancies in GCN, upon modulating the structural properties from bulk to planar and corrugated structures.[55] The surface structure of GCN representing different N-atoms is depicted in Fig. 3a. The report suggested that, out of three types of N-atoms in hexagonal heptazine based GCN (bridged nitrogen (N_{3C1}), central nitrogen (N_{3C2}), and 2-fold coordination nitrogen (N_{2C})), the central ternary nitrogen N_{3C2} was the easiest to remove because of the lowest vacancy formation energy (0.67 eV). However, the vacancy formation energy for bridged N_{3C1} nitrogen was 1.95 eV and for 2-fold coordinated N_{2C} nitrogen was 0.92 eV, slightly higher than that of N_{3C2} but still much less than that of N_{3C1} nitrogen. The study further revealed that altering the structure through N-vacancies and corrugation confirmation in GCN synergistically improved the photocatalytic efficacy by boosting the optical absorption ability and radiative carrier isolation efficiency. In another study, Liu *et al.* utilised first principles density functional theory (DFT) calculations to scrutinise the effect of N-vacancies in modulating the energy levels (electronic structure) and, subsequently, the photocatalytic efficacy.[56] The atomic structure models of pristine GCN (CN) and N-vacancy generated GCN (CN-4) (Fig. 3b and c) depicted the origin of N-vacancies *via* removal of nitrogen from amino groups in tri-*s*-triazine rings. Fig. 3d and e show the movement of the VB and CB of the CN-4 photocatalyst towards more negative energy levels, resulting in a decreased bandgap of 2.50 eV as compared to 3.07 eV of CN. Moreover, the presence of N-vacancies created defect states around the Fermi levels originating from 2p orbitals of the C atom having dangling bonds around defective sites. Additionally, C-atoms around vacancy regions possessed electron-rich behaviour due to solitary electron pairs resulting from N-vacancies delocalised in the whole conjugated system. As a result, the CN-4 system showed improved electronic properties as demonstrated by differential charge density results in Fig. 3f and g.

Apart from N-vacancies, carbon vacancy generation in GCN can also modulate the catalytic features of GCN, resulting in superior photoefficacy. For instance, Liang *et al.* revealed the effect of C-vacancies on the photocatalytic performance of holey GCN by evaluating its performance for photocatalytic H_2 production.[57] An insight into X-ray photoelectron spectroscopy (XPS) results vouchsafed the loss of graphitic carbon species (the peak area ratio of N=C–N to C=C increased from 0.13 to 0.14) due to thermal treatment, resulting in superior conductivity and mobility of photocarriers. Moreover, generation of C-

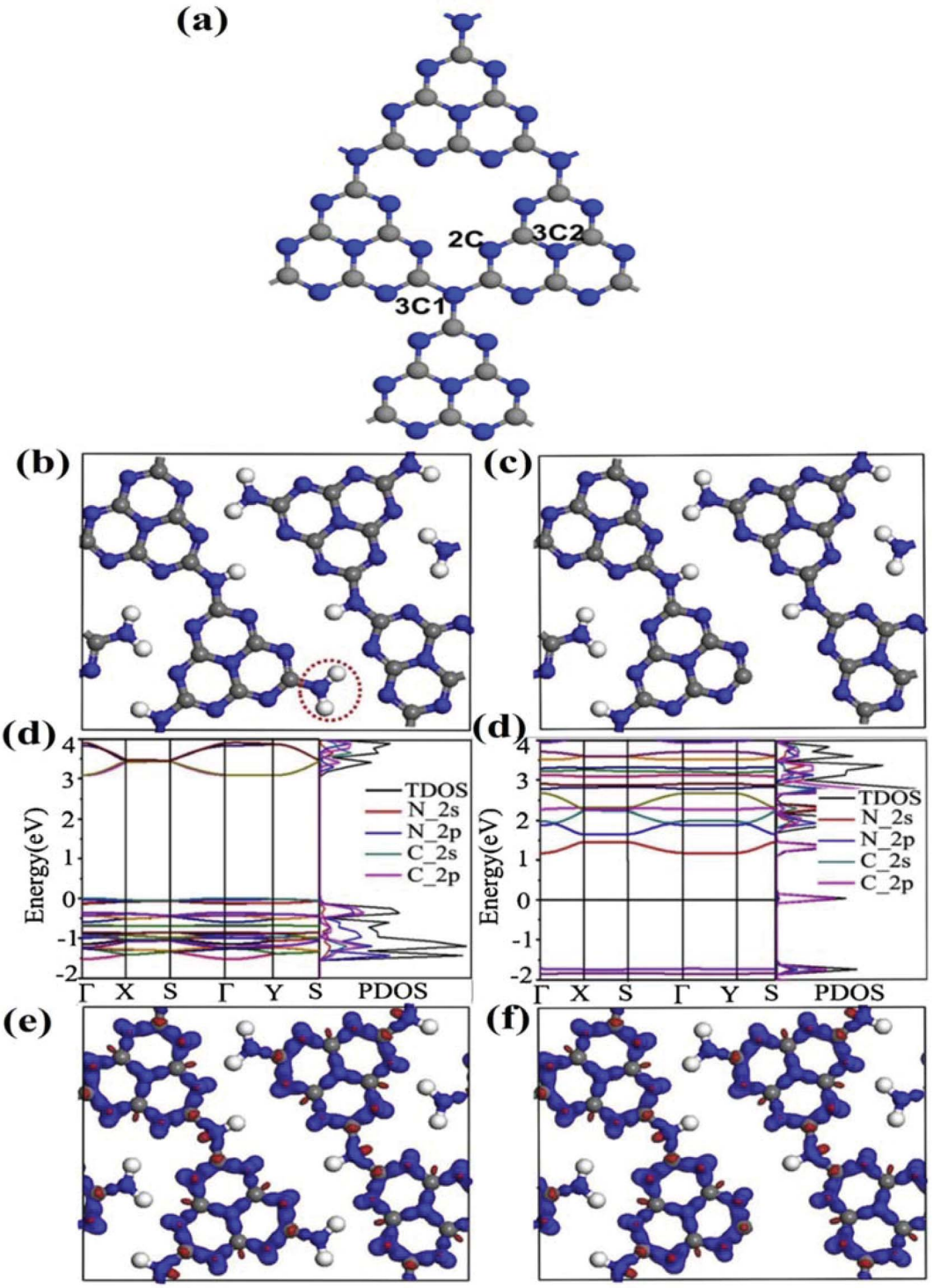

Fig. 3 (a) Surface structure of GCN representing different N-atoms (adapted with permission Copyright 2019 American Chemical Society).[55] Schematic representation of top view of the optimized (b) CN and (c) CN-4 configuration, color scheme: C, grey; N, blue; H, white. Band structure and density of states (DOS) of (d) CN and (e) CN-4. The differential charge density of (f) CN and (g) CN-4 (adapted with permission under license no. 4846640889986, Copyright 2020 Elsevier).[56]

vacancies resulted in transformation of the C=C bond in the heptazine ring into the N=C bond. C-Vacancies in holey GCN also ameliorated the light absorption ability and extended it into the near infra-red (NIR) region (800–1400 nm), caused by the multiple reflections of light in holes and vacant sites. Di *et al.* designed porous ultrathin GCN with confined surface C-vacancy defects having an average thickness of 0.9 nm, which substantially boost the isolation of radiative carriers for bulk as

well as for the surface.[58] The ultrathin structure, along with C-vacancy sites synergistically worked for the migration of carriers from bulk to the surface of the photocatalyst and captured them for further photocatalytic reactions. Thus, vacancy generation in GCN by removing C or N is equally alluring as it not only refines the visible light harnessing by introducing defective electronic states but also amends the isolation efficiency of radiative charge carriers along with superior surface reaction kinetics. However, theoretical studies involving DFT calculations showed that generation of C-vacancies narrows the bandgap energy and redshifts the optical absorption range, and N-vacancies induce defective midgap states in between the bandgap to promote visible light absorption ability and boost the isolation of photocarriers.[59] In the case of N-vacancies, the defective midgap states are generated due to the formation of N-vacancy related defect states (originating from the accumulation of extra electrons at C-atoms near vacancy sites in the GCN matrix) just below the conduction band minimum (CBM). Besides C-vacancies tuned the bandgap energy of GCN by shifting CBM positioning and improve the redox ability of GCN. Nevertheless, by reviewing the literature on C-/N-vacancy modified GCN we found that C-vacancy modified GCN is less explored which could be ascribed to the formation of less stable and more deformative structural arrangement of GCN caused by the removal of C-atoms.[59–61]

Hitherto, defect engineered photocatalysts have been widely explored owing to their fascinating features of improving overall photocatalytic efficacy. Various review articles have exploited the potential of defect engineering in the field of photocatalysis and represented defect engineered semiconductor substances as a promising method for efficient solar energy conversion applications.[58,62] For instance, Liu *et al.* presented an organised study of defect engineered photocatalysts and explained the introduction of defects with suitable characterisation techniques for improvement in photocatalytic water splitting.[63]

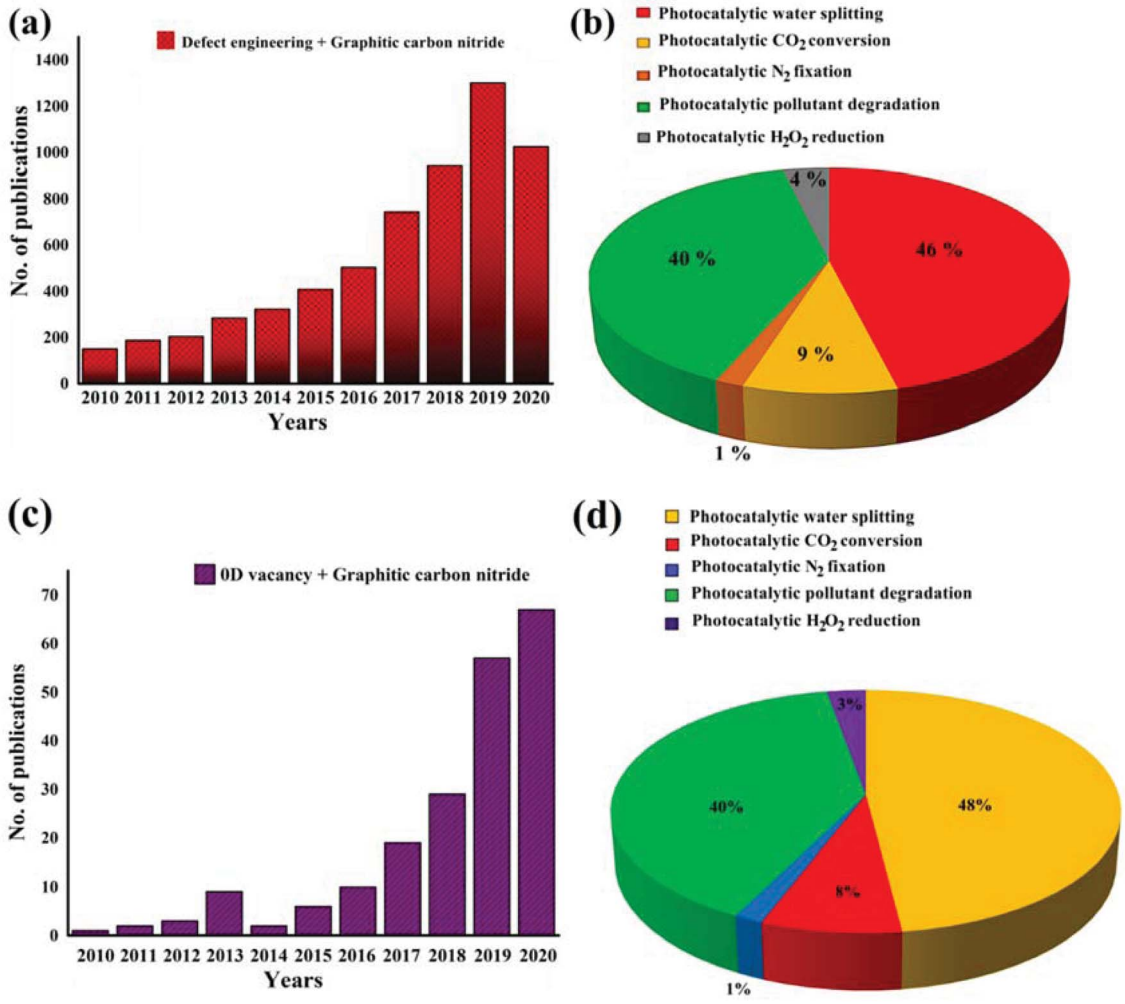

Fig. 4 Representation of (a) number of publications concerning the keyword "Defect engineering + Graphitic carbon nitride" published from 2010 to April 2020; (b) pie chart depicting various photocatalytic applications of defect engineered graphitic carbon nitride; (c) number of publications concerning the keyword "0D Vacancy + Graphitic carbon nitride" published from 2010 to April 2020; (d) pie chart depicting various photocatalytic applications of vacancy induced graphitic carbon nitride; the data are obtained from "Scopus" database.

Similarly, Ran *et al.* presented various defect induced photocatalytic materials for solar energy conversion and broadly discussed different aspects of defect engineering to modulate the photocatalytic performance.[64] Bai *et al.* also discussed defect engineering along with important functions of the defect as a potential strategy to manoeuvre systematically the basic steps involved in photocatalysis.[65] Other than this, Xiong *et al.* beautifully summarised tuning of various photoelectric parameters of 2D semiconductor materials by surface defect engineering and highlighted the important role of surface defects in versatile photocatalytic applications.[66] Even after significant research exploration in the field of defect engineered photocatalysts, we feel that necessary information is required on metal-free catalytic substances modulated by defect engineering so that we could systematically probe the design, impact and function of defects. Typically, defect modified GCN is doubtlessly a topic of interest as evidenced from the growing research papers (analysed by Scopus database) in indexed journals regarding keywords "Defect engineering + Graphitic carbon nitride" from 2010 to April 2020 (Fig. 4a). Moreover, modulation through defect engineering in optoelectronic and structural features of GCN, led to amended photo-efficiency in various photocatalytic applications as can be seen from the 'Scopus' data analysis results depicted in Fig. 4b. Similarly, to gain an insight into the research work on vacancy induced GCN, "0D vacancy + Graphitic carbon nitride" was the effective keyword used and the data were plotted from 2010 to April 2020, as shown by Fig. 4c, along with different photocatalytic applications (Fig. 4d).

Thus, inspired from the fascinating features and extensive research interest in the exploration of metal-free polymeric GCN, herein, we aim to provide a comprehensive overview involving recent advances in vacancy defect engineered GCN photocatalysts that are employed in various environmental and energy-related applications. Firstly, we started with a brief introduction of defect engineering in photocatalysis along with the impact of 0D point defects (mainly vacancies) on GCN photocatalysts. In the following section, we shortly summarised the classification of defects and influence of vacancy introduction in the GCN framework. Afterwards, we emphasised the role of various designing strategies involving thermal, chemical and other advanced treatment processes for the controlled generation of vacancy defects in GCN. Furthermore, for evaluation and characterisation of vacancy defects in the structural network of GCN, numerous advanced characterisation techniques including structural, morphological, chemical, optical, and electronic properties and computational studies were outlined. Then the significance of defect engineering in GCN with special focus on its influence on the optical, electronic and surface photoreactions was explored and highlighted. The role of vacancy defect engineered GCN in various photocatalytic applications like water splitting, CO_2 conversion, N_2 fixation, pollutant degradation and H_2O_2 production was systematically reviewed and summarised. Finally, the review ends with a summary which provides an insight into the challenges and future opportunities in the present field from our viewpoint.

2. Creation of vacancy defects in the g-C_3N_4 photocatalyst

Defects in a semiconductor photocatalyst can be generated *via* two modes, *i.e.* defect creation into pre-designed semiconductor photocatalysts and defect creation during the synthesis. Generation of defects in pre-synthesised photocatalysts is independent of the growth kinetics of the crystal and is widely opted for the creation of vacancies, voids, disorder as well as for the introduction of dopants. On the other hand, the generation of defects during the formation of photocatalytic material brings about the creation of bulk defects like dislocations and boundaries, which much rely on the growth kinetics of nanomaterials.[65] Considering the positive influence of vacancy generation for direct conversion of solar energy, it is imperative to discuss promising strategies to create vacancies in GCN. For a better understanding of the underlying photocatalytic mechanism induced by vacancy rich photocatalysts, the prerequisite is a generation of vacancies in a controlled atmosphere to foster synergy between defects and photoactivity. Of note, methods utilised for defect generation strictly relies on the type of defect induced in a photocatalyst. Thus, it is imperative to select a particular synthetic route for the generation of the desired defect in semiconductor photocatalysts. The detailed summary of different methods utilised for the synthesis of defect induced GCN is discussed as follows:

2.1 Thermal treatment

In general, the synthesis of GCN proceeds only through thermal treatment involving calcination and annealing of nitrogen-rich precursors. However, to synthesise defect rich GCN, there are several other strategies, which involve the use of other chemicals as precursors followed by thermal treatment. For instance, Sun *et al.* reported the fabrication of GCN, reduced GCN (RCN), oxygenated GCN (CNO) and reduced oxygenated GCN through thermal treatment.[67] A nitrogen vacancy was generated in the system through H_2 reduction, while oxygen was introduced with the help of thermal treatment (hydrothermal/condensation process). By creating a nitrogen vacancy in GCN, the conduction band (CB) energy was reduced from −0.75 eV to −0.5 eV by generating defective band levels just below the CB. On the other hand, the introduction of oxygen reduced the valance band (VB) from 2.05 eV to 2.30 eV by the formation of functional groups containing oxygen (C═O and C–O) which remarkably boosted the isolation efficacy. Consequently, the photoactivity and photocurrent density of RCNO, were about 8–9 times more than those of pristine GCN. Apart from that, pyrolysis of precursors under appropriate reaction environments (vacuum, airflow and inert atmosphere) plays a crucial role in defect generation. For instance, Li *et al.* demonstrated the formation of carbon vacancy modified C_3N_4 nanotubes (TN 500) for effective selective oxidation of NO to NO_3^- by pyrolysis of a mixture containing urea and melamine under an inert atmosphere of N_2.[68] The nano-tubular structured C_3N_4 with 20 μm length and a 1–2 μm diameter was obtained. The impact of the N_2 atmosphere during thermal treatment was clearly observed with the help of

Scanning Electron Microscopy (SEM), and Transmission Electron Microscopy (TEM) analyses, as depicted in Fig. 5. The inert atmosphere of N_2 significantly exfoliates bulk C_3N_4 (Fig. 5a–f) into thin structures with the introduction of defects *via* complete condensation of precursors. A conjecture vouchsafed that, with a slight modification in the calcination environment, the formation of defects in GCN can be facilitated. Other than N_2, argon gas flow was also utilised to generate a carbon vacancy in GCN. Carbon vacancy induced GCN was fabricated by Li *et al.* through the calcination of melamine up to 520 °C under the inert atmosphere of argon gas in a tube furnace.[69] The report suggested that C vacancies in GCN led to exposed amino nitrogen which facilitated the photocatalytic production rate of H_2O_2 by avoiding the use of any organic scavengers. The construction of C-vacancies in GCN accompanied by the appearance of amino nitrogen is depicted in Fig. 6a and b. Similarly, Chu *et al.* created nitrogen vacancies in GCN (NV-C_3N_4) by the direct calcination of urea and melamine under airflow followed by liquid exfoliation.[70] Furthermore, an Ar environment was introduced to generate nitrogen vacancies in GCN. In order to amend the active surface sites, nitrogen vacancies in GCN were filled by S dopants introduced by annealing of previously prepared samples and resulted in a sample was labelled S-NV-C_3N_4. The complete synthesis scheme representing the formation of vacancy generation and introduction of S dopants is presented in Fig. 6c. A deep insight into TEM analysis (Fig. 6d–f) of bare GCN (C_3N_4), NV-C_3N_4 and S-NV-C_3N_4 revealed that all the samples displayed a crumpled sheet-like structure. However, due to the generation of N-vacancies, the long-range ordered atomic arrangement of C_3N_4 was damaged, resulting in a comparatively more wrinkled structure. However, incorporation of the S-dopant in NV-C_3N_4 exhibited no apparent change in the morphology of NV-C_3N_4 and showed an almost similar crimpled structure (Fig. 6f).

Consequently, thermal treatment is a widely approached versatile strategy for generating vacancies in GCN. By only controlling the thermal conditions and avoiding the use of any extra additives like templates and chemical reagents, properties of GCN can be significantly varied based on the requirement along with morphological modulations. However, attaining a well-ordered structural framework or defective structure by controlling the temperature or duration of one-step thermal

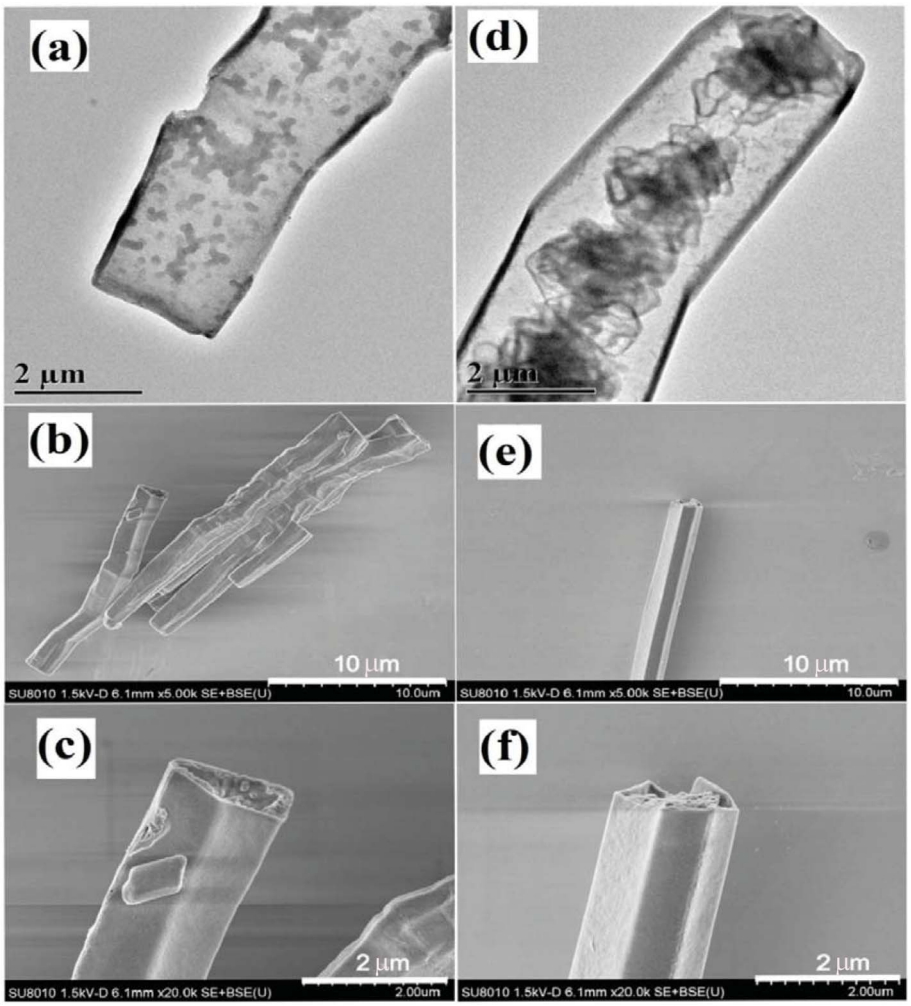

Fig. 5 TEM and SEM images obtained from (a–c) bare GCN (T 500) and (d–f) defect induced GCN from different magnifications depicting the effect of N_2 atmosphere during thermal treatment (adapted with permission under license no. 4775711061628, Copyright 2020 Elsevier).[68]

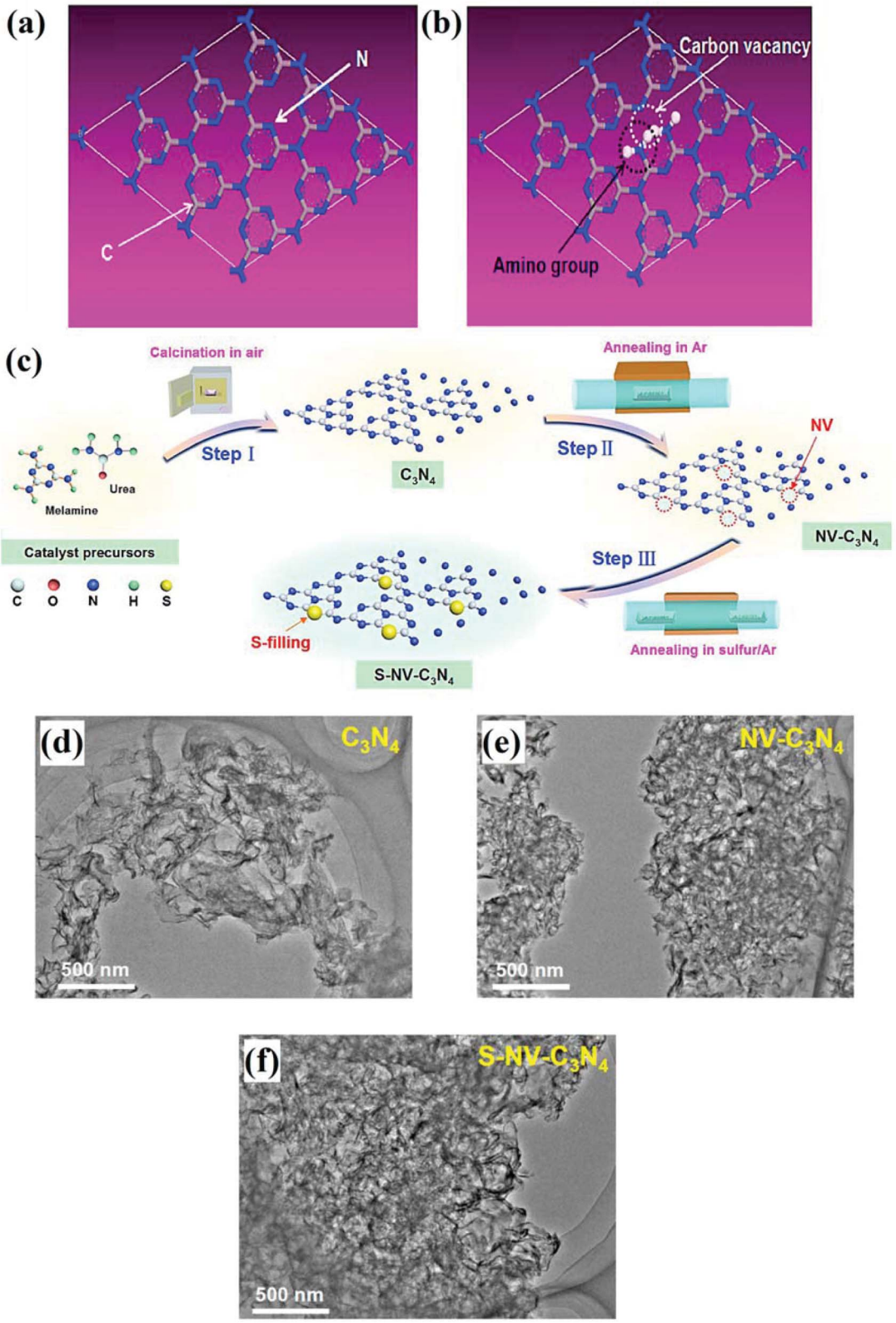

Fig. 6 Schematic representation of (a) structural unit of GCN and (b) presence of C-vacancy and amino group in GCN (reproduced with permission under license no. 4802920609594, Copyright 2016 Elsevier).[69] (c) A schematic insight into the synthesis route for the formation of S-NV-C_3N_4, TEM images of: (d) C_3N_4, (e) NV-C_3N_4 and (f) S-NV-C_3N_4 (adapted with permission under license no. 4923570778416, Copyright 2020 Elsevier).[70]

treatment is practically difficult. Additionally, post-thermal treatment of GCN in order to induce vacancy defects causes structural deformation due to high energy consumption leading to a reduced production rate of photocatalysts.[71] By changing the atmospheric conditions, the challenge mentioned above can be overcome yet, precise distribution and controlled generation of vacancy defects *via* thermal treatment still need further exploration.

2.2 Chemical treatment

Thermal treatment of different chemicals like molten salts (LiCl, NaCl, KCl, $NaBH_4$, $NaHCO_3$ *etc.*) and organic acids (oxalic acid, tartaric acid and hydrofluoric acid) is a fascinating route for generating vacancy defects in GCN.[72,73] Incorporating appropriate *in situ* chemical environments based on the formation of vacancies can create surface defects in GCN which can effectively boost the photoactivity of GCN. Acid treatment of GCN or its precursors is one of the most opted chemical treatment processes for developing vacancy defects in GCN. For instance, treatment of GCN precursors with a weak acid like tartaric acid (TA) induced a chemical reaction with amino groups which lead to the formation of defects on the surface of GCN, while TA decomposed into CO_2 and H_2O at high temperatures. Inspired by this, Shi *et al.* designed nitrogen defective 2D GCN with N vacancies positioned at both tricoordinated N atoms.[74] Typically, to generate N vacancies, TA was mixed into an aqueous solution containing dicyandiamide, and the resulting mixture was calcined at 550 °C for 3 h. The study further revealed that the introduction of nitrogen defects in GCN particularly helped to generate active reaction sites and boosted dissociation of radiative carriers which in turn improved the photocatalytic CO evolution efficiency (56.9 μmol g^{-1} h^{-1}). In another study, defective nitrogen GCN (CN-HAc) was fabricated through thermal condensation of melamine feedstock treated with acetic acid as depicted in Fig. 7a.[75] Nitrogen vacancy defects in GCN led to optimal electronic band structures, extended visible light-harvesting ability, and amended isolation of photoinduced excitons. As a result, the vacancy defect engineered GCN photocatalyst exhibited improved photocatalytic discolouration of RhB along with superior H_2 evolution. In order to improve the visible light harnessing ability of GCN, carbon and defect co-modulated GCN was tailored by Wu *et al.*, exploiting facile calcination of oxalic acid treated melamine feedstock.[76] The defect rich GCN (C_xCN) led to a porous morphology with a modified active surface area as compared to pristine GCN. Moreover, to confirm the extended absorption of visible light and to analyse the modification in bandgap (Fig. 7b and c), DFT calculations were performed as shown in Fig. 7d and e. From DFT analysis, it was inferred that defect induced GCN (Fig. 7d) with suitable band energy alignments (Fig. 7e) displayed better photodegradation efficacy under visible light exposure.

It is a well known fact that defects in GCN are intrinsic and sometimes if not controlled are detrimental to photoactivity by acting as reassembly sites for photoinduced excitons.[77] To address this issue, scientists have worked to control/remodel vacancy defects in GCN. For instance, Lin *et al.* modified the introduction of defects in GCN by treating it with a solution containing hydrofluoric acid and ethanol which was further subjected to autoclave conditions and heated for 6 h keeping the temperature at 140 °C.[78] The study further manifested that by utilizing solvothermal treatment, the number of defects in GCN can be controlled. Besides, the action of fluorine stimulates nitrogen-vacancy generation, which in turn acted as an active reaction centre and boosted the photoactivity of the sample for H_2 production by 13 times from bulk GCN. From high-resolution TEM analysis, it was observed that the pristine GCN obtained through the calcination of dicyandiamide and the NH_4Cl template (referred as CNS) showed pleated silk veil nanosheets with a crinkly structure (Fig. 7f). The introduction of the fluorine impurity and subsequent N-vacancies through solvothermal treatment (Et-CNS) and fluorine assisted solvothermal treatment (F-CNS) had no significant impact on the crinkled morphology as shown in Fig. 7g and h, respectively. However, the substantially decreased size of Et-CNS and F-CNS nanosheets was due to the polycondensation induced by fluorination and solvothermal treatment.

In another study, an interesting methodology was applied to generate nitrogen vacancies along with the introduction of oxygen dopants, resulting in the formation of a porous structure.[79] Typically, strongly oxidative ammonium persulphate ($(NH_4)_2S_2O_8$) was used to treat dicyandiamide thermally, which not only control the polycondensation to induce nitrogen vacancies but also provided a porous structure to GCN (p-CN2) by the involvement of oxygen dopants. This synergic treatment refined the electronic features of GCN by changing π band states along with lone-pair electrons and the transitions between them. Besides, separation of carriers was considerably augmented by introducing impurity levels (facilitate electron excitation), and favourable transitions between the as-resulted highest occupied molecular orbitals (HOMOs) and the lowest unoccupied molecular orbitals (LUMOs). The whole synthesis scheme of nitrogen-deficient oxygen doped GCN is depicted in Fig. 8a. Through TEM analysis, an evident change in the morphology of p-CN2 treated with ammonium persulphate was observed which showed thinner nanosheets with a more porous structure (Fig. 8c) as compared to bare GCN (Fig. 8b). Also, the brighter image and thin morphology of p-CN2 were due to the increased interlayer stacking distance caused by chemical treatment. Thus, a series of chemical treatments followed by thermal operation leads to the formation of typical defect rich GCN photocatalysts with desirable features which are captivating in photocatalysis. The use of additional chemicals which are less stable and metal-free provides different atmospheres during calcination, which helps to exfoliate 2D nanosheets of GCN along with the creation of defects. The use of chemicals which liberate ammonia during calcination induces a specific reaction environment, which is helpful to generate vacancy defects in porous GCN nanosheets.[57] However, the involvement of molten salts boosts the diffusion of feedstocks by acting as a highly reactive medium and reduces the temperature range of reaction.[72] Moreover, the process of copolymerization is significantly enhanced by fostering the slow deamination process

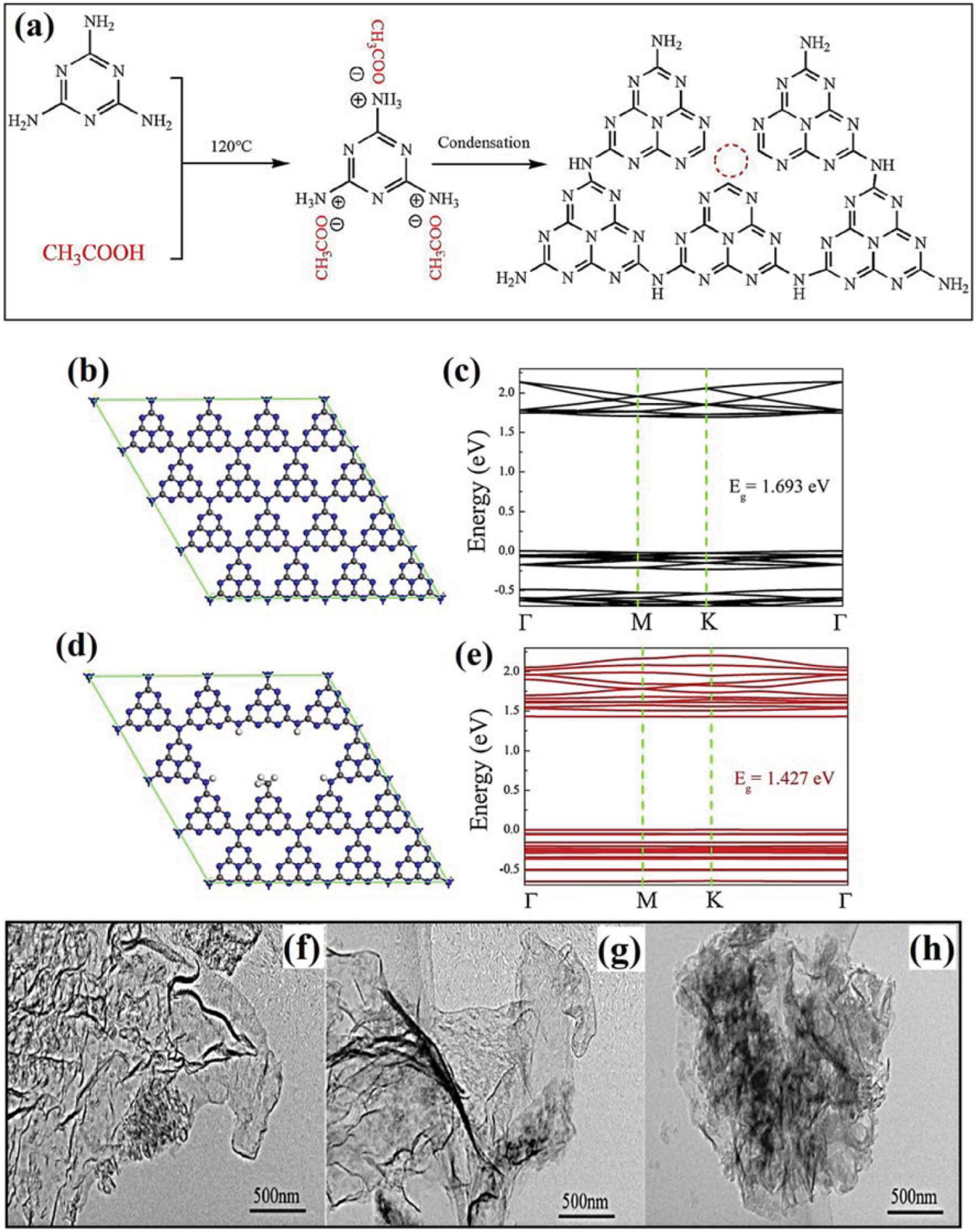

Fig. 7 (a) Schematic illustrating the formation mechanism of N-deficient CN-HAc (reprinted with permission under license no. 4776010206434, Copyright 2017 Elsevier).[75] Schematic representation of (b) theoretical model of GCN and (c) band structure of GCN; (d) theoretical model of C_xCN and (e) its band structure obtained from DFT calculations (reprinted with permission under license no. 477685063636999, Copyright 2020 Elsevier).[76] TEM images of: (f) CNS, (g) Et-CNS and (h) F-CNS (reproduced with permission under license no. 4923670696920, Copyright 2020 Elsevier).[78]

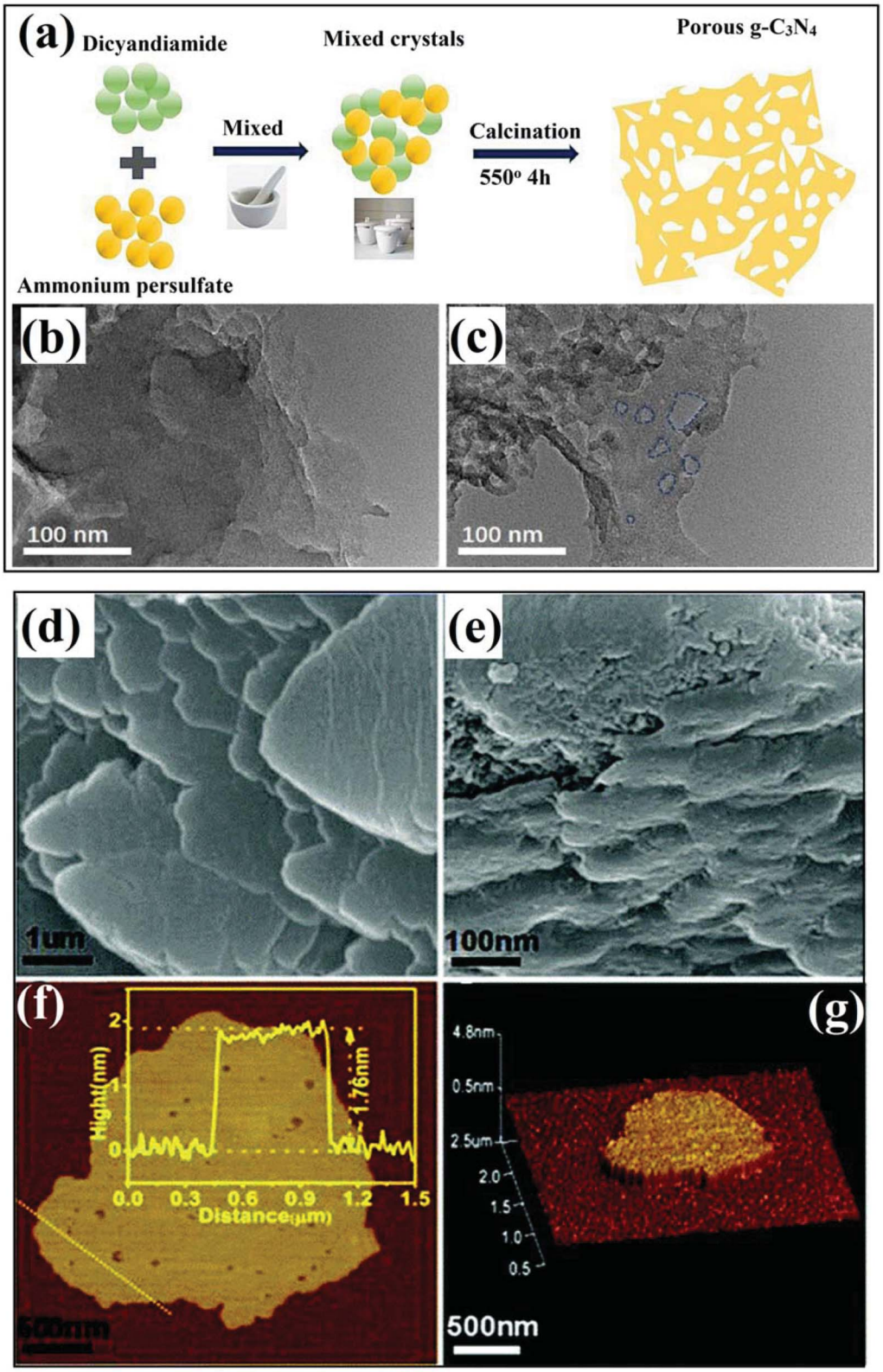

Fig. 8 (a) Schematic illustrating the formation of vacancy defect modified porous GCN sample (p-CN2) (b) TEM image of bulk GCN (g-C_3N_4) and (c) TEM image of p-CN2 (adapted with permission under license no. 4924060325465, Copyright 2019 Elsevier).[79] (d) SEM image of bulk GCN; (e) SEM image of DCNNS sample; (f) AFM analysis with corresponding height (inset) of DCNNS and; (g) 3D image of DCNNS-450 sample (adapted with permission under license no. 1031838-1, Copyright 2018 Royal Society of Chemistry).[80]

resulting in improved stacking distance between the layers of GCN with a controlled generation of defects.[73] Thus, chemical treatment of suitable raw material in order to achieve a unique polycondensation process along with defect creation is a fascinating approach with substantial scope for further exploration.

2.3 Other treatment methods

In addition to thermal treatment and chemical treatment, there are undoubtedly other approaches which are significantly helpful for the controlled generation of vacancy defects in GCN. For instance, Xu *et al.* utilised a system involving ultrasonic disruption process used to exfoliate 2D photocatalytic material.[80] The typical process involved the exfoliation of previously synthesised GCN (using melamine precursor) by using an ultrasound probe for 5 h, which yielded GCN nanosheets. The as-obtained nanosheets were further treated in a hot air oven, and the dried sample was calcined in a mixture of a H_2 (10%)/N_2 environment. The effective treatment process resulted in soft and loose agglomerates in defective sample DCNNS-450 (Fig. 8d) as compared to pristine GCN with relatively stable agglomerates (Fig. 8e). Furthermore, precise analysis concerning thickness and morphology of the DCNNS-450 sample was scrutinised through tapping atomic force microscopy (AFM) as depicted in Fig. 8f and g. The results inferred that the height of random nanosheets (two) was ~1.76 nm (Fig. 8f), confirmed from a 3D image of DCNNS-450 in Fig. 8g. In another study, an N-vacancy tailored GCN sample was prepared through a modified hydrogen reduction method during thermal treatment which involved vacancy creation in pre-synthesised samples.[81] Treatment with H_2 led to homogeneous modulation with N-vacancies due to significant interaction between H_2 and interlayers of GCN nanosheets. Typically, the GCN nanosheet sample was introduced in a porcelain boat and subjected to heat treatment (540 °C at a ramp of 5 °C min^{-1}) in a H_2/Ar: 50%/50% environment. The as-obtained sample was enriched with N-vacancies, which helped to break the intrinsic electronic state spreading, resulting in disordered energy interfaces around the defective sites. Consequently, the maximum energy difference of 0.36 eV was sufficient enough to produce hot excitons by their dissociation.

Other than this, microwave-assisted treatment and ball milling processes have also been considered for manufacturing defect rich GCN photocatalysts. Utilising the microwave heating process for fabricating advanced photocatalytic materials substantially accelerates reaction kinetics by providing direct energy to the reactants and lowers the energy consumption rate.[82] Treating N-rich precursors with microwave radiation boosts the collision rate of molecules and enhances the pyrolysis process leading to defect modified GCN in a few minutes. On the other hand, the complexity of bond activation and surface defect generation through the ball milling method restricts its wide-scale applicability which needs further clarification.[83]

Summarily, various synthetic techniques have been utilized for the successful generation of vacancy defects in GCN. However, the existing methods exhibit particular inherent bottlenecks in controlled defect designing and mass production. Tailoring of vacancy defect modulated GCN with a unique structural motif is difficult since the study on the impact of temperature variation and involvement of different chemicals is limited. Additionally, it is challenging to control simultaneously the type, quantity and exact location of the defects with present synthetic routes. What is more, the chances of introducing extra impurities through chemical treatment are exceptionally high. As a result, the co-existence of impurity defects and intrinsic defects substantially impedes the identification and scrutiny of the impact of defect generation on photocatalytic activity. Thus, it is highly desirable to tailor efficient GCN photocatalysts with vacancy defects in order to attain high photoefficacy.

3. Characterisation of vacancy defects in the g-C_3N_4 photocatalyst

As reviewed earlier, generation of defects seemed to be an effective approach to modulate the overall photo-efficacy of GCN, but characterizing those defects is equally important to gain insight at atomic levels. However, it is still a tricky task to study the relationship between the introduction of defects at the atomic level and the underlying photocatalytic properties. Moreover, to establish a better understanding of designing the route to alter the atomic structure, it is necessary to exploit the number of defects induced in the semiconductor photocatalyst. To date, researchers have utilised numerous characterisation techniques to investigate the location of vacancy defects and their respective concentration in GCN as summarised below.

Various characterisation methods involving structural, morphological, chemical, optical, electronic properties and computational studies through first-principles studies are vastly used to investigate the introduction of vacancy defects in GCN. Precisely, to analyse the position and type of defect in the GCN photocatalyst, selection of suitable characterisation techniques plays a crucial role.[11,54] In order to analyse surface-induced defects and defects in the bulk, SEM and TEM analyses are preferred, respectively. For instance, the high energy electron beam in TEM can analyse the defects generated in the bulk as well as at the surface of the photocatalyst without differentiating them. Atomic force microscopy (AFM) and SEM can significantly examine surface defects in the GCN photocatalyst. Besides, scanning transmission electron microscopy (STEM) is an optimal approach for comparative analysis of bulk and surface-induced defects.[84] Moreover, structural changes in GCN due to the introduction of vacancy defects can be analysed with the help of X-ray diffraction (XRD) analysis. It is a well-known fact that by generating vacancy defects in GCN, its chemical and optical features, as well as electronic properties, get significantly modulated, resulting in superior photoactivity. For effective inspection of chemical changes produced in GCN due to defect engineering, XPS and Fourier transformation infrared (FTIR) spectroscopic analysis are very advantageous. Besides, optical and electronic properties of the vacancy defect induced GCN sample can be investigated through UV-visible, electrochemical impedance, and photoluminescence (PL)

spectroscopic techniques, respectively. Other than microscopic and spectroscopic techniques, computational modelling methods have also been employed to study the electronic band structure of vacancy defect induced GCN. The detailed explanation of these characterisation methods illustrating the formation of vacancy defects in GCN is summarised as follows:

Shi *et al.* fabricated a defect induced GCN (CN) coupled $KNbO_3$ (KNO) (KNO/CN*x*) system and analysed its structural, chemical as well as morphological changes with the help of XRD, FTIR, and SEM techniques, respectively as depicted in Fig. 9a–d.[85] The impact of N vacancies on the actual structural motif of GCN was investigated and explained by variation in XRD peaks (Fig. 9a). Diffraction peaks of pure GCN were recorded at 13.1° and 27.4°, ascribed to interlaminar reflection between (100) and (002) aromatic planes of the graphitic structure. In comparison, in the case of vacancy defect modified GCN, a slight variation in the (002) plane was observed, and the intensity of the peak attributed to the (100) plane decreased significantly. A disturbance caused this structural variation in a planar arrangement of GCN due to N vacancies. Similarly, chemical analysis through FTIR depicted an extra vibration band in defect induced GCN at 2177 cm^{-1} due to dominating asymmetric stretching vibration of underlying –C≡N groups, suggesting the presence of N vacancies (Fig. 9b). From SEM images, variation in morphology of N vacancy rich GCN was observed as shown in Fig. 9c and d. Pure GCN exhibited a dense structure with irregular arrangement carrying lower surface area and less active sites for photocatalytic reactions (Fig. 9c). On the other hand, defective GCN with N-vacancies displayed a comparatively loose structure with the presence of voids at the surface, which simultaneously boosted the surface area and visible light absorption (Fig. 9d). Moreover, other analysis techniques used to investigate the chemical composition of a sample, involving XPS and electron spin resonance (ESR) spectroscopy played a significant role in the characterisation of defect rich photocatalysts. For instance, Wang *et al.* investigated the presence of C/N vacancies in GCN nanosheets by comparing the results of elemental analysis (EA) through XPS and ESR spectroscopy.[59] XPS results illustrated that defect modified GCN samples (CN) with C/N atomic ratio 1.437 (CN4) exhibited an extra peak in C 1s spectra at 286.1 eV, indicating the presence of the C/N vacancies on heptazine edges or –the C≡N group. On the other hand, N 1s spectra inferred that the intensity of peak at 286.1 eV increased with increasing ion irradiation fluence (He^+), supporting the presence of N-vacancies. However, EA analysis indicated that the central vacancy atom in GCN is N, not carbon and increased intensity of C was due to deviation in –the C≡N group as shown in Fig. 10a–e. To verify this result, the electron paramagnetic resonance spectroscopy (EPR) experiment was performed, as shown in Fig. 10f. With the help of EPR,

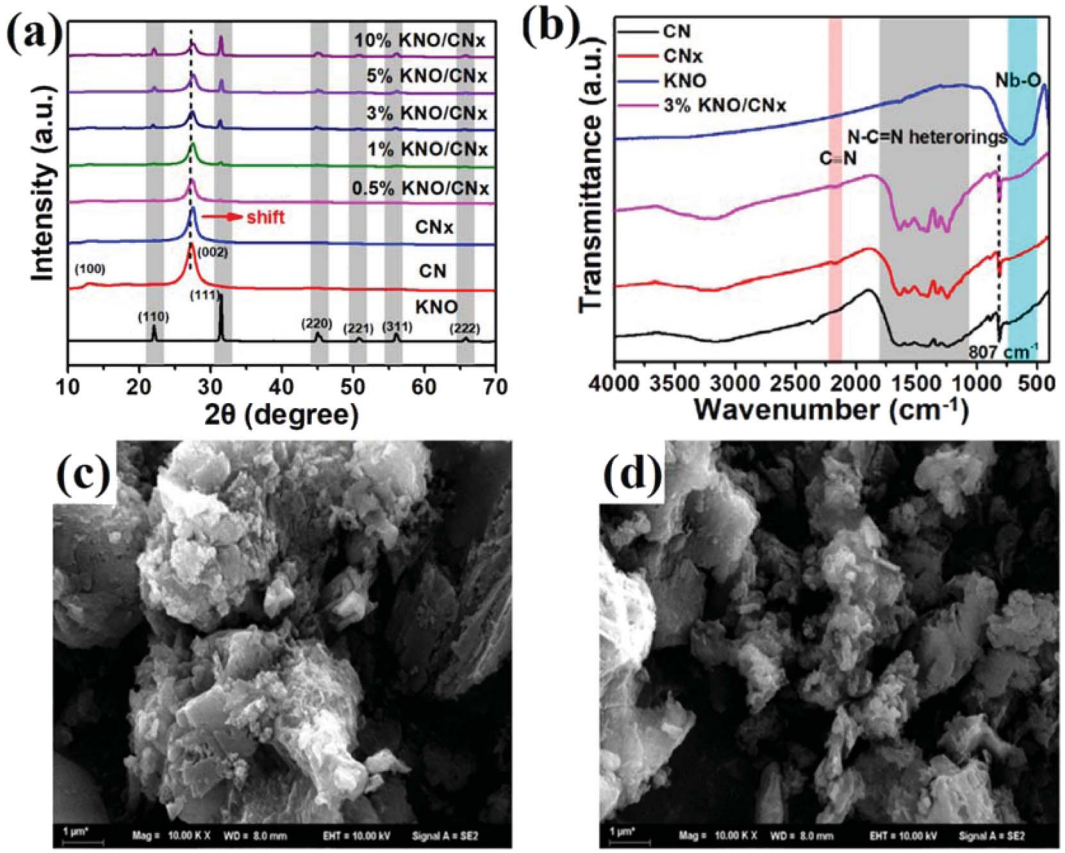

Fig. 9 Schematic illustrating the: (a) XRD patterns of KNO/CN*x* photocatalytic system; (b) FTIR spectrum of KNO/CN*x* photocatalytic system. SEM images of; (c) CN and (d) CN*x* sample (reproduced with permission under license no. 4781120550794, Copyright 2020 Wiley).[85]

the Lorentzian line was observed at $g = 2.0037$, which depicted the presence of unpaired electrons. Moreover, vacancy defects in GCN can smartly increase the unpaired electrons at the C atom of heptazine units. Additionally, by combining the results of EPR and XPS, the presence of dual defects in GCN was successfully confirmed.

Vacancy defects in GCN are helpful to generate active sites as well as the enlarged surface area to promote its photocatalytic performance as inspected by various studies. Moreover, the enhancement in optical as well as electronic properties of defect rich GCN is another fascinating feature which boosted the photoefficacy as analysed by appropriate characterisation techniques. To support this statement, Li *et al.* illustrated the difference in light absorption by GCN and vacancy defect modified GCN (C_v-gCN) by UV-vis absorption analysis as depicted in Fig. 10g.[86] Experimental results suggested that the diffusion reflectance spectroscopy (DRS) curves of both pristine GCN and defect induced GCN are somewhat similar, but defective GCN showed a small decrease (25 nm) in absorption (blue shifted). As a consequence, the bandgap energy of vacancy modulated GCN was increased by 0.16 eV possibly due to the presence of carbon vacancies. Variation in the electronic properties of the samples was compared with the help of EIS spectroscopic analysis, as depicted in Fig. 10h and i. As discussed before, the introduction of vacancies aids to boost the migration and isolation of carriers. In order to verify this statement,

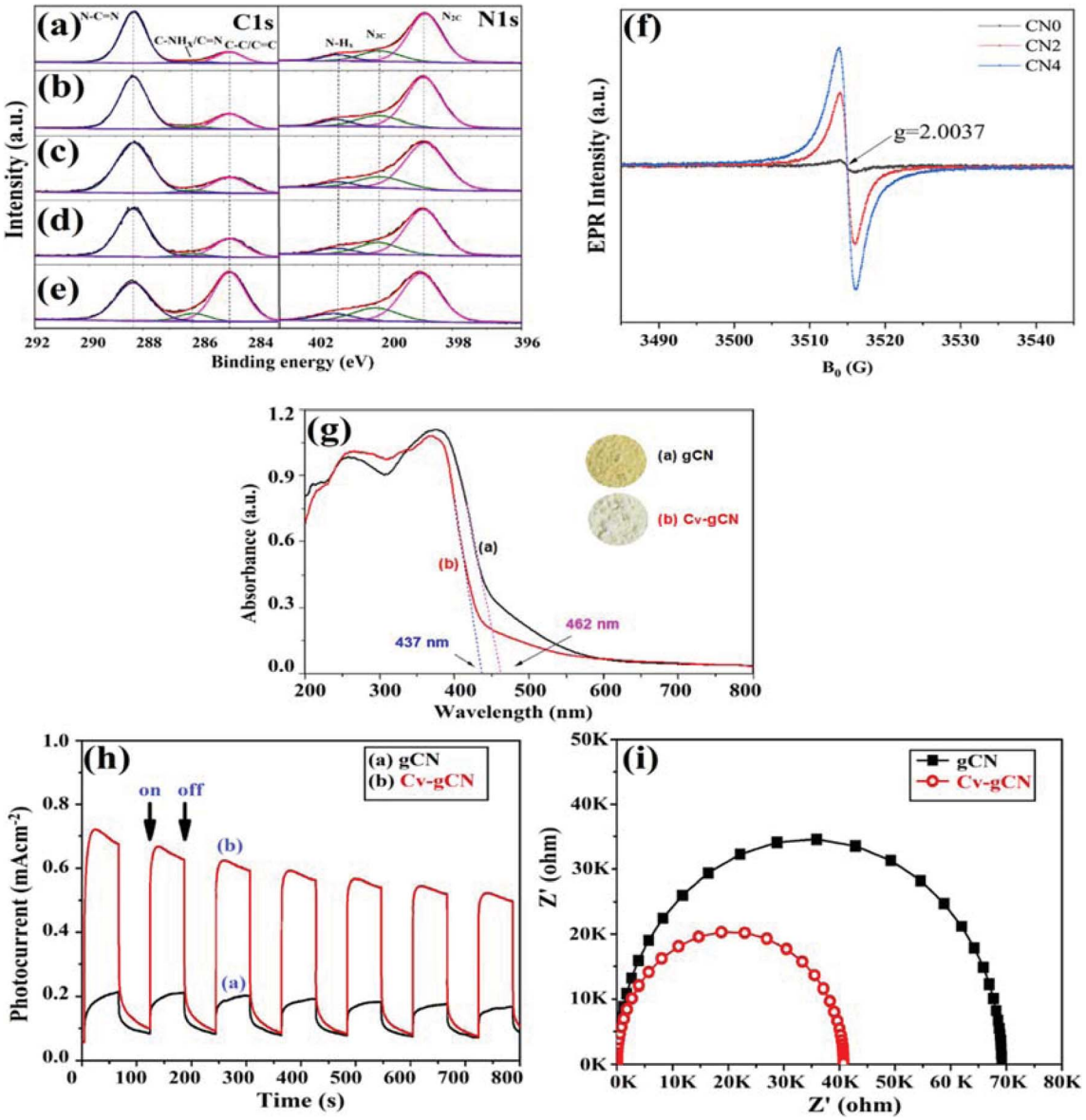

Fig. 10 Schematic representation of the XPS spectra of C 1s and N 1s orbitals for (a) pristine GCN (CN0) and the defective samples with distinct C/N ratio [(b) CN1, (c) CN2, (d) CN3, and (e) CN4, respectively]. (f) EPR spectra are representing the CN and defect induced CN samples (adapted with permission under license no. 4781250556536, Copyright 2019 Wiley).[59] Schematic representation of (g) UV-vis diffuse reflectance spectra of pristine GCN and C_v-gCN; (h) time-dependent photocurrent analysis; and (i) EIS Nyquist plots (adapted with permission under license no. 482075074553, Copyright 2018 Elsevier).[86]

photocurrent responses of defective GCN with C-vacancies and bare GCN were analysed, as shown in Fig. 10h. The results depicted that the recorded photocurrent of bare GCN was exceptionally low due to rapid reassembly of photocarriers. However, vacancy rich GCN displayed comparatively high photoresponse values depicting delayed reassembly of radiative excitons. To further confirm the effective separation of photocarriers in the case of defect induced GCN, EIS analysis was performed, which illustrated a noteworthy difference in the Nyquist plots, as shown in Fig. 10i. The arc radius of defect induced GCN obtained in Nyquist plots was much smaller than that of pristine GCN inferring rapid migration and isolation of photoinduced carriers after the creation of C vacancies. Thus, vacancy generation can be an effective strategy to foster the space separation of radiative carriers as well as to harvest solar light.

Other than microscopic/spectroscopic analysis techniques, a computational investigation approach to study the impact of vacancy defect generation in GCN can synergistically help to understand electronic band-structure variation as well as dissociation of photocarriers in GCN. For instance, Mo *et al.* reported first principles investigation studies to illustrate the effect of N vacancies to modulate the electronic band structure of GCN.[87] N-Vacancy defects in the GCN structural framework were introduced by the treatment of pristine GCN in the selenium vapour environment. DFT calculations inferred that the formation of defect states (DSs) due to the introduction of N vacancies expanded the bandgap of defective GCN, which resulted in improved photocatalytic activity. Atomic structures of GCN containing one N vacancy and band structures of pristine GCN as well as defective GCN are shown in Fig. 11a and b. From Fig. 11b, the bandgap of pristine GCN was found to be 2.61 eV which matched the literature value. However, after introducing N vacancies in GCN, a C–C bond was formed around a vacant region which changed the shape of hexagonal rings into a pentagon (Fig. 11a). The formation of DS in the band levels of GCN was introduced by the p state of C and N atoms present around a defective site. As a consequence of DS, the migration path for photoinduced excitons decreased due to the lowering of bandgap energy from 2.61 eV to 2.54 eV as shown in Fig. 11c. Liu *et al.* investigated the influence of C and N vacancies in GCN *via* first-principles calculations with hybrid functional theory.[88] Their investigation included the study of vacancy generation in GCN by removing carbon atoms

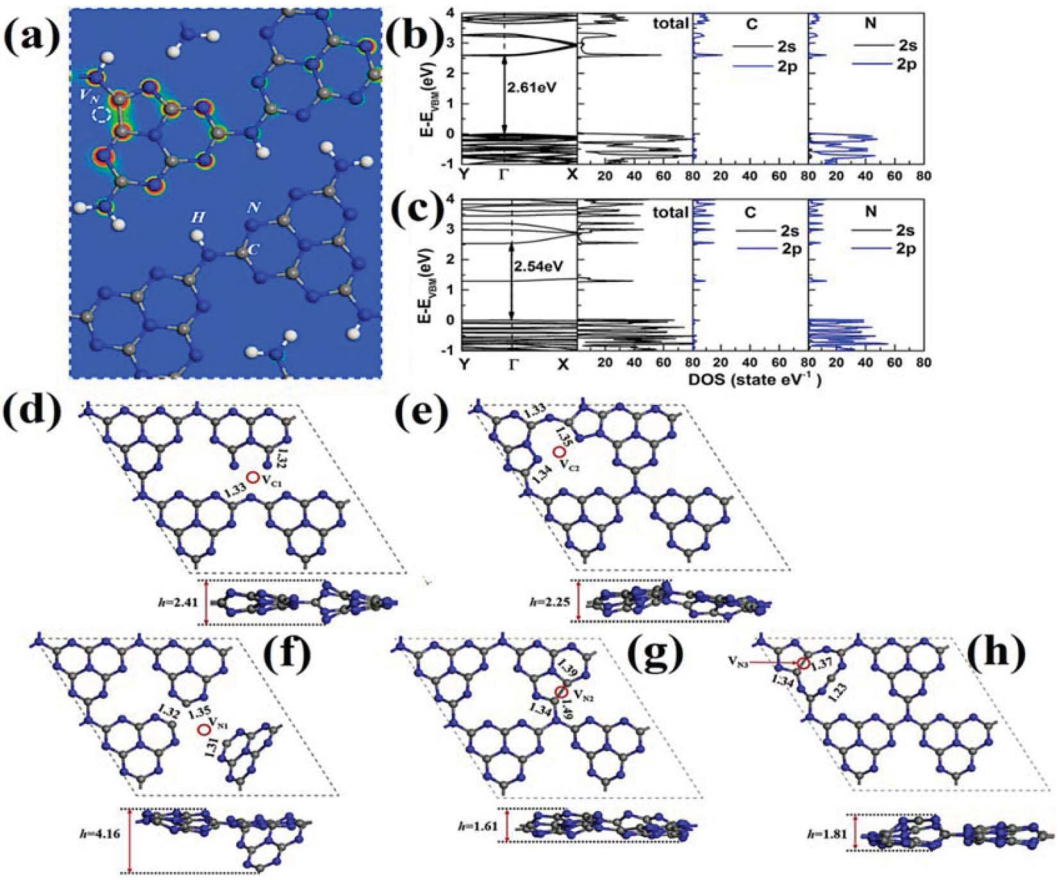

Fig. 11 (a) Schematic illustrating the calculated band structures of one N-vacancy induced GCN. (b) and (c) represents band structures along with DOS studies of GCN and defect induced GCN (reprinted with permission under license no. 4798050795202, Copyright 2019 Elsevier).[87] Top and side views of modulated GCN illustrating vacancies at (d) V_{C1}, (e) V_{C2}, (f) V_{N1}, (g) V_{N2}, and (h) V_{N3} with their respective bond length around vacancy site showing through the red circle and buckling height *h* (reprinted with permission under license no. 4818801289489437, Copyright 2020 Elsevier).[88]

Table 1 Summary of various characterisation techniques with their advantages and disadvantages used to identify vacancy defects in GCN

Characterisation technique	Advantage	Disadvantage
HRTEM/STEM	Surface reorganisation due to vacancy defect generation	The amount and exact position of vacancy defects cannot be measured
AFM	Identification of surface and subsurface vacancy defects	
EA	Identification of the elemental composition	Position and concentration of vacancy defects cannot be measured
XPS	Used to evaluate defect type, chemical state, composition, vacancy concentration and band-structure	Limited testing depth to few nanometres, it can only reflect semi-quantified information of surface vacancies
ESR	Sensitive to identify single electron trapped vacancy	It can only partially identify the density of vacancies through peak intensity
DFT	Identification of charge distribution around the vacancy region and to calculate energy bandgap positioning	The band-gap underestimation of standard density-functional methods and subsequent errors in calculating defect-related levels

from positions C1 or C2 or the removal of nitrogen atoms from N1, N2, or N3 positions as depicted in Fig. 11d–h. The structural distortion was clearly observed when a single atom of C (V_{C1} or V_{C2}) was removed from GCN, bringing about a significant increase (2.41 Å) and a decrease (2.25 Å) in buckling height as compared with a pristine sample by V_{C1} and V_{C2}, respectively (Fig. 11d and e). Moreover, generation of N-vacancies by removing N1, N2 and N3 atoms in GCN led to even more prominent structural distortions with soared buckling height to 4.16, 1.62 and 1.82 Å with V_{N1}, V_{N2} and V_{N3}, respectively as shown in Fig. 11f–h. Consequently, structural tuning of GCN with defect engineering substantially amend animated, optical and electronic features for increaseted photocatalytic performance. Table 1 summarises various characterisation techniques with their advantages and disadvantages for identifying vacancy defects in GCN.

4. Role of vacancy defects in boosting the photocatalytic activity of g-C_3N_4

Formation of controlled vacancy defects in GCN and their appropriate characterisation can lead to improved photocatalytic performance by modulating various features involving electronic, optical and structural properties. Effectiveness of vacancy defect generation in GCN towards various photocatalytic applications is quite evident, and mechanistic insight to understand their potential is critically important. The following section will highlight the significance of vacancy defect generation in GCN, which can further be utilised to tailor defect induced GCN photocatalysts with superior photocatalytic properties.

4.1 Extending visible light absorption

It is a well-known fact that absorption of light strictly relies on bandgap energy of the photocatalyst material. Precisely, a semiconductor photocatalyst can only absorb energy equal to or greater than its bandgap energy. After absorption of photons, the electrons are excited to a higher energy CB and involve in reduction reactions, leaving behind holes in the VB of the semiconductor where they participate in oxidation reactions. Depending upon bandgap energies of photocatalysts, a semiconductor material with broad bandgap energy can only absorb solar light in the UV region (λ < 420 nm) which involves only about 5% of the total solar spectrum.[89–91] On the other hand, semiconductor materials, which have small bandgap energy, could display light absorption in the visible (420 < λ < 780 nm) or NIR regions (780 < λ < 2500 nm) which accounts for about 43% and 52% of the total solar spectrum, respectively. Moreover, a semiconductor photocatalyst with inappropriate potential edges (positive VB potential and more negative CB edge potential) hinders overall redox abilities of the system. Vacancy defect engineered photocatalysts can overcome this barrier by the superior harnessing of solar light as vacancy generation induce midgap defective states which modulate the electronic structure and extend the light absorption region.[92] Precisely, through vacancy generation, defect induced sites with weaker bonding obstruct splitting of bonding and anti-bonding orbitals and generate defective midgap states resulting in reduced excitation distance and in turn increase the light absorption region.

In order to understand the synergy of narrowed bandgap and extended light absorption, Yang *et al.* utilised the hard template method with the high pressure and high temperature (HPHT) technique to synthesise N-vacancy induced GCN.[93] The resulting vacancy defect rich GCN sample displayed reduced interlayered distance, up-shifted VB and down-shifted CB edge potential. As a result, N-vacancy mediated GCN exhibited extended visible light absorption (Fig. 12a) due to a significantly narrowed bandgap of 1.88 eV (Fig. 12b). Fig. 12a depicts the redshift in absorption from bulk GCN to defect induced GCN, which was red (inset image) and showed a maximum absorption of 660 nm. Furthermore, the graphs from $(\alpha h\nu)^{1/2}$ *vs.* photon energy showed a substantial decrease in bandgap energy, and the vacancy modified GCN sample (PNCN-2) exhibited a bandgap energy of 1.88 eV. At the same time, Zhao *et al.* explained the synergy of introducing N-vacancy defects and boron doping simultaneously in GCN engineered

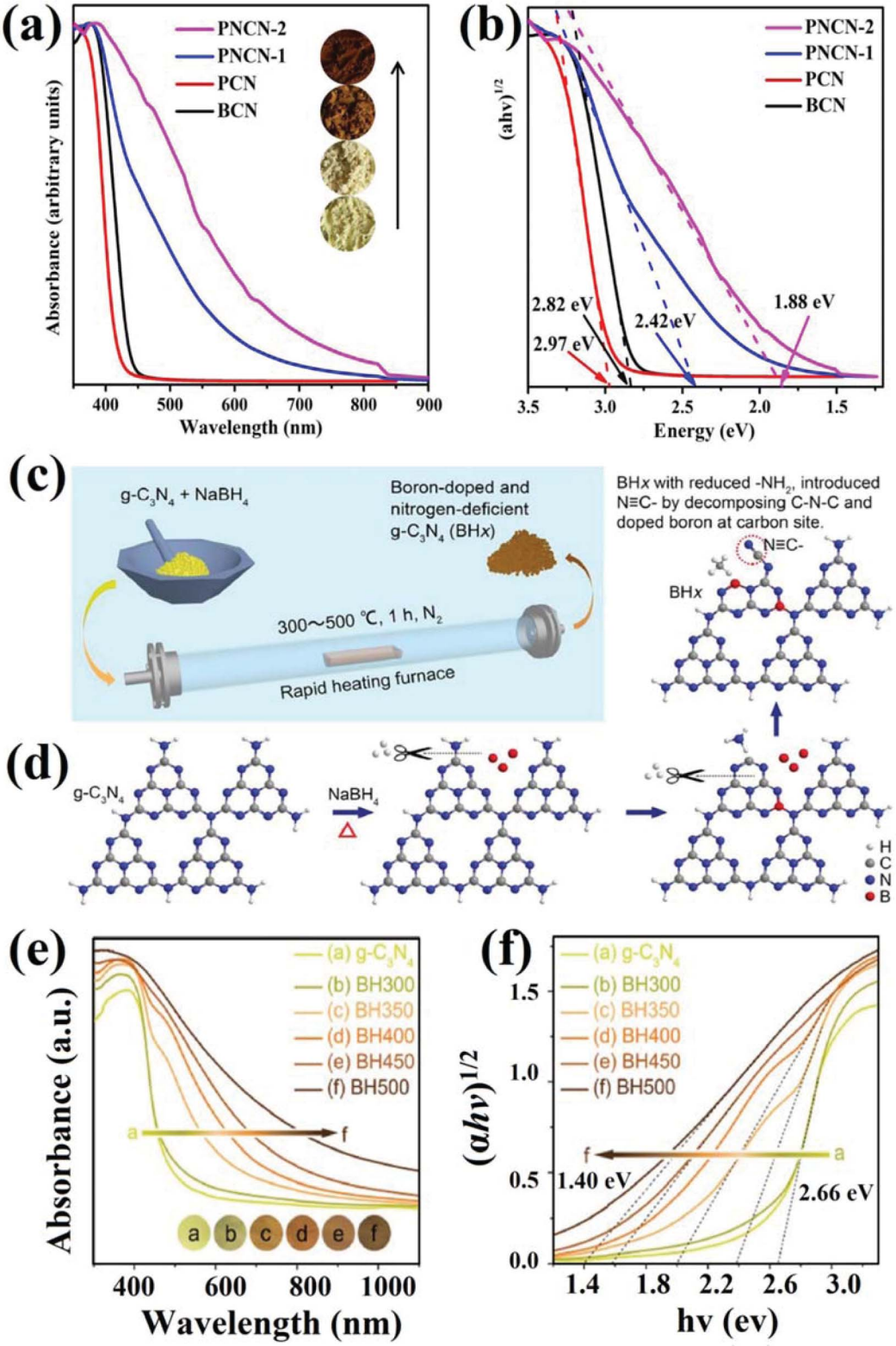

Fig. 12 Schematic illustration of (a) UV-vis DRS spectra and (b) plots representing $(\alpha h\nu)^{1/2}$ *vs.* photon energy (adapted with permission under license no. 4792401424595, Copyright 2020 Elsevier).[93] (c) Diagrammatic representation of the synthesis mechanism of defective BH*x* sample and (d) possible changes in the structural framework of GCN by thermal treatment. Schematic representation of (e) UV-vis DRS plots of various defect induced BH*x* samples prepared under different temperatures and (f) plots depicting the transformed Kubelka–Munk function *vs.* energy (adapted with permission under license no. 4792910600654, Copyright 2019 Wiley).[94]

via calcination of GCN with $NaBH_4$ under an inert atmosphere of N_2 at different temperature ranges as shown in Fig. 12c.[94] It was observed that through synergism of boron doping and N-vacancy in GCN (BH*x*), the electronic structure and optical absorption was remarkably optimised resulting in improved photocatalytic efficacy. N-Vacancies were introduced by thermal treatment of GCN with $NaBH_4$ and the possible changes in heptazine tectonic units of GCN are displayed in Fig. 12d. The enhancement in optical absorption by different samples was observed through UV-vis diffuse reflectance spectroscopic analysis which depicted the increased redshift as the temperature increased to 500 °C (Fig. 12e). Moreover, the enhancement in absorption suggested a noteworthy contribution of boron doping as well as N-vacancies to tune the bandgap energy from 2.66 eV (pristine GCN) to 1.40 eV (defect induced GCN) by introducing defective midgap states (Fig. 12f).

In a similar study extended visible light absorption was achieved by simultaneous incorporation of N-vacancies and subsequent iodine doping into the mesoporous structure of GCN.[95] The process involved thermolysis of glucose and NH_4I, which provided superior exfoliation of iodine doped GCN, N-vacancy induced GCN by releasing N-rich dynamic gases and improved light harnessing due to introduction of DS just below the CB edge. The presence of the midgap state acted as a reservoir which facilitated the trapping of radiative e^- in defective GCN. Enhancement in light absorption abilities of vacancy defect modified GCN was scrutinised by UV-vis DRS spectroscopy which confirmed a superior harnessing range by showing a broadband tail (Urbach tails) red-shifted towards the visible range due to the presence of N-vacancies. Of note, the appearance of the Urbach tail is due to the presence of defective electronic states lying inside the bandgap (intraband or midgap states) as a result of defect engineering.[96] The presence of midgap states was evaluated by combining results from UV-vis DRS analysis and VB XPS spectra which showed the position of the midgap state for bare GCN at −44 V and N-vacancy modified GCN at −21 V (*vs.* NHE), respectively. As a result, the existence of intraband or midgap states facilitated electron excitation from the VB to the midgap state of N-vacancy modified GCN and broadened absorption in the visible region. Thus, through appropriate modulation of the bandgap energy by the introduction of vacancies, light absorption ability of GCN can be considerably enhanced, leading to optimal photocatalytic efficacy.

4.2 Rapid transfer and isolation of photogenerated electron–hole pairs

Generally, efficient migration and separation of photoinduced excitons play a crucial role in maintaining the redox abilities as well as photocatalytic efficacy of the semiconductor materials. Dissociation of radiative carriers usually proceeds through random pathways in a semiconductor photocatalyst during the photocatalytic process under visible light illumination. However, the whole photocatalytic process is greatly hindered by reassembly of photo-illuminated excitons as only a few photocarriers reach the surface of a photocatalyst to participate in redox reactions.[97,98] In order to avoid reassembly and to boost the photocatalytic efficacy of GCN, the introduction of controlled defects is one of the most appropriate strategies as defects can also act as a recombination centre for photoinduced excitons. Noteworthily, the introduction of defective electronic states in between the bandgap of a semiconductor not only fosters the light-harvesting abilities but also provides significant routes for energetic relaxation of photocarriers within the energy bandgap and stimulates carrier dynamics. Defective electronic states instigated from surface defects in a semiconductor photocatalyst are known as "trap-states" or "surface-states". However, migration and isolation modes of bulk as well as surface defects, are different.[99] Xue *et al.* reported a facile technique to foster the dissociation of photocarriers by generating N-defects in GCN by the introduction of cyano groups through alkali-assisted thermal treatment of urea (represented as NC-g-C_3N_4).[100] A study suggested that the introduction of cyano groups substantially suppresses the reassembly of photocarriers by acting as a sink to photo-illuminated e^- of defective GCN. The charge carrier dynamics and suppressed reassembly were analysed with PL studies as shown in Fig. 13a and b. Fig. 13a depicted continuous PL spectra which indicated deprived reassembly of photocarriers in defect induced GCN by showing a less intense curve than pristine GCN. On the other hand, time-resolved PL spectra (Fig. 13b) suggested that the intensity lifetime (τ) of defect modified GCN was 14.15 μs which is knowingly higher than that of pure GCN (12.23 μs). An increased lifetime of excitons suggested superior isolation and hence improved photocatalytic efficacy. Furthermore, photocurrent responses and EIS analysis were used to investigate the charge separation efficiency of photocatalysts. Photocurrent responses of both NC-g-C_3N_4 and pristine GCN were observed to be optimistic after specific on–off cycles. However, NC-g-C_3N_4 showed significantly enhanced photocurrent intensity suggesting a superior separation of photoinduced excitons (Fig. 13c). Results from EIS spectroscopic analysis also confirmed effective charge carrier isolation in NC-g-C_3N_4 by showing a comparatively smaller arc size of NC-g-C_3N_4 in the dark (Fig. 13d) as well as under the exposure of light (Fig. 13e). Liao *et al.* introduced N-vacancy defects in the GCN framework by thermally treating GCN in a hydrogen environment and utilised its potential for effective photo-oxidation of NO.[101] Hydrogen treatment partially removed surficial nitrogen from the GCN network and reduced bandgap energy resulting in increased optical properties as well as improved charge carrier kinetics. The concentration of photocarriers participating in catalytic photoreactions determines the overall photoactivity of a system, which strictly relies on optimal charge carrier separation. Further investigation on dissociation kinetics of photocarriers induced by GCN enriched with N-defects (CN-H-*T*) was explored by PL, surface photovoltage and time-resolved fluorescence analysis. From PL, the quenched PL spectrum of defective GCN was observed indicating suppressed reassembly of photocarriers (Fig. 13f). Furthermore, the defect modulated GCN sample (CN-H-600) displayed a significantly intense SPV response, as depicted in Fig. 13g. Similarly, time-resolved fluorescence spectra (nanosecond) of CN-H-600 represented longer lifetime (6.18 ns) of

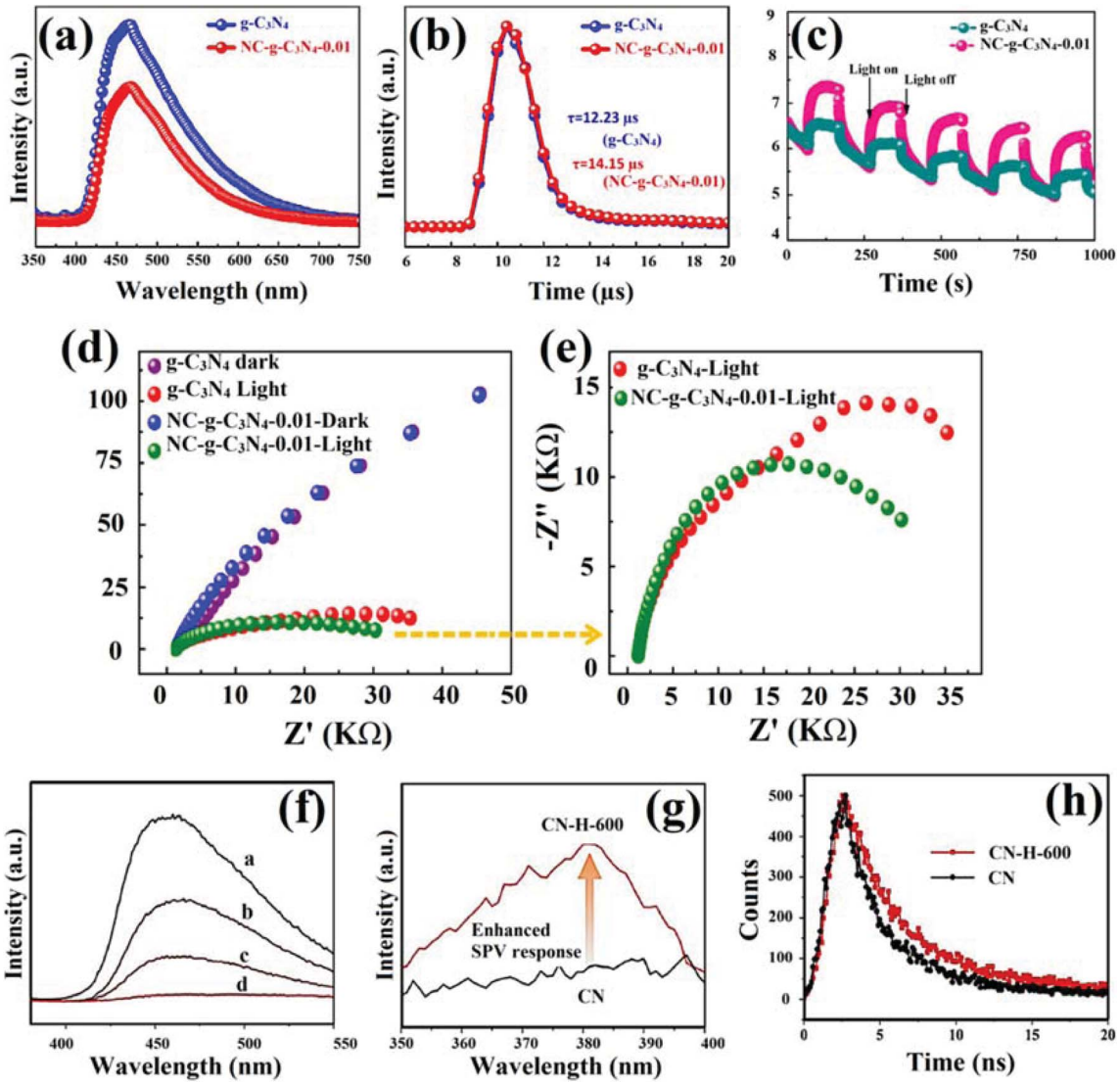

Fig. 13 Schematic representation of (a) steady photoluminescence (PL); (b) time-resolved PL decay analysis; (c) photocurrent responses, (d and e) EIS curves of GCN and defect induced GCN (NC-g-C_3N_4-0.01) (reproduced with permission under license no. 4798050559416, Copyright 2019 Elsevier).[100] Schematic representation of (f) PL spectra of different defect induced GCN samples (CN-H-600) in a particular order – CN-H-600, CN-H-550, CN-H-500, CN from top to bottom; (g) surface photovoltage spectra; and (h) time-resolved fluorescence spectra (at nanosecond-level) observed at room temperature (reproduced with permission under license no. 4821200816869, Copyright 2020 Elsevier).[101]

photoinduced carriers than that of pristine GCN (1.89 ns) (Fig. 13h). The separation and suppressed recombination of excitons were further explained by the fact that during the photo-excitation process electrons get migrated to defective N-sites resulting in the formation of localised electron conduction. The process mentioned above substantially deprived reassembly of photocarriers by modulating in-plane electron migration in GCN. As a result, isolated carriers can contribute effectively in photoinduced redox reactions before reassembly and boost the photoactivity of GCN.

Although defect engineered single component systems have shown significant improvement in charge migration, and lower recombination, space charge isolation of carriers by forming semiconductor hybrids is another fascinating approach with optimal outcomes. By constructing hybrid junctions, spatial separation of photocarriers at different photocatalysts is achieved through interfacial transference.[102,103] In such systems, defect engineering can be executed either on the interfaces of photocatalysts or on the adjoined supporting material, which can remarkably modulate charge separation kinetics. For instance, Tay *et al.* coupled N-vacancy enriched GCN with two-phase TiO_2 (anatase/brookite) nanoparticles (NPs) along with three-phase TiO_2 (anatase/brookite/rutile) to form different heterojunction systems and compared their photocatalytic performances for photocatalytic H_2 production.[104] Photocatalytic studies revealed that two-phase TiO_2 exhibited better photocatalytic H_2 production than the three-phase system due to superior radiative exciton dissociation as well as an appropriate CB edge. Furthermore, in order to utilise the effectiveness of charge separation, band edge potentials of semiconductor

photocatalysts must be more cathodic than H_2 reduction potential. Effectiveness of coupling defective GCN with two-phase TiO_2 for suppressed recombination was explained based on band offset of adjoined photocatalysts. The smaller CB offset between coupled semiconductor system leads to rapid interfacial migration of electrons due to significantly increased wave function overlap. Defect generation lowered the bandgap energy of GCN, and as a result, the CB offset of defective GCN with brookite TiO_2 was observed to be 0.07 eV. Thus, with a more favourable CB offset alignment of defect modified GCN

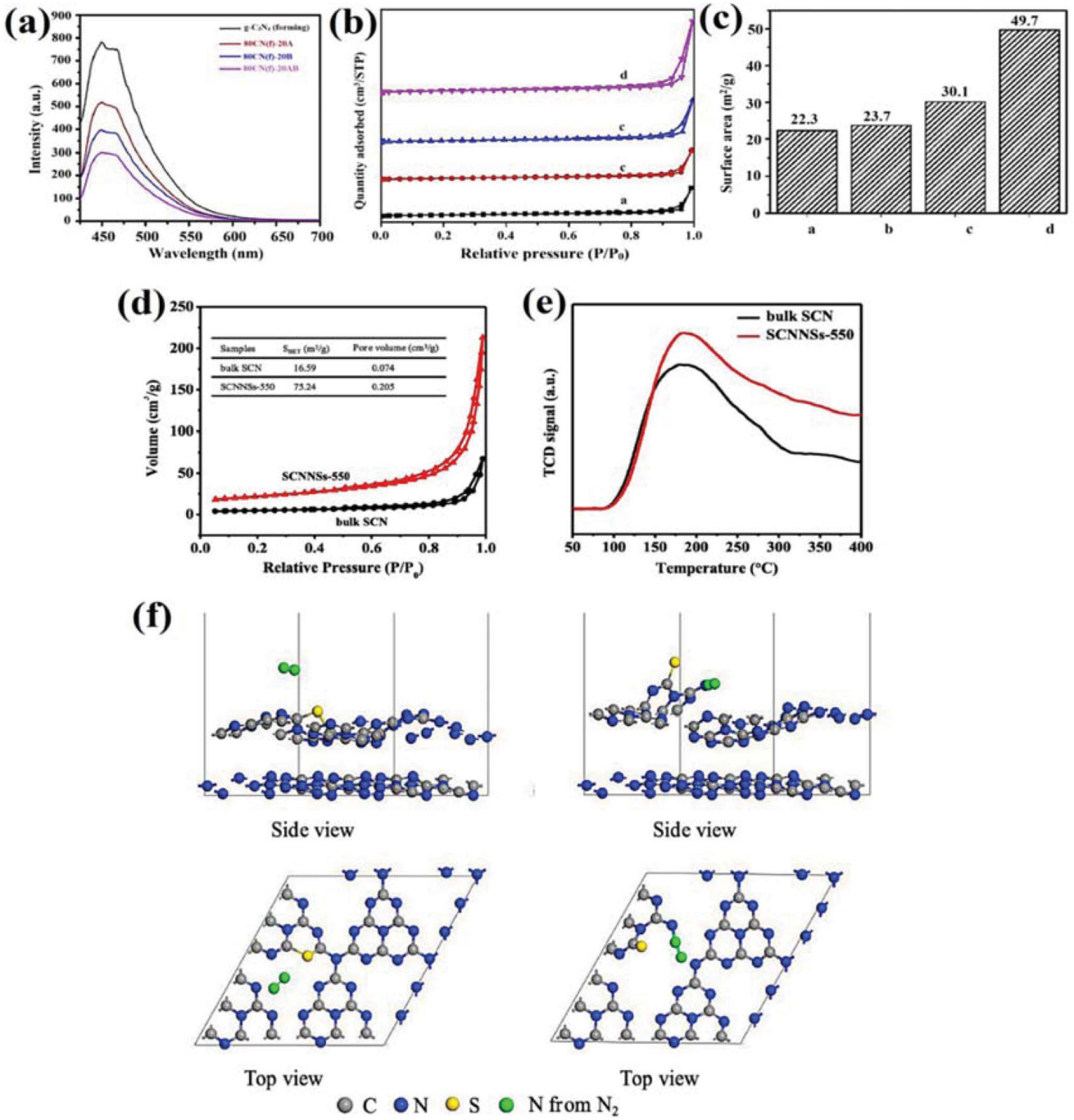

Fig. 14 (a) Schematic illustrating the PL spectra of g-C_3N_4 forming and 80 wt% of g-C_3N_4 forming with anatase, brookite, and two-phase anatase/brookite TiO_2 (reprinted with permission under license no. 4800200745195, Copyright 2016 Elsevier).[104] Schematic representation of (b) N_2 adsorption–desorption isotherm; and (c) BET histogram of different samples, namely: a-bg-CN, b-NVCN-1, c-NVCN-2 and d-NVCN-3 (reprinted with permission under license no. 4801480649105, Copyright 2019 Elsevier).[112] Diagrammatic illustration of (d) N_2 adsorption–desorption isotherms along with corresponding pore volume in the inset; (e) N_2-TPD spectra of bulk SCN and SCNNSs-550; and (f) side and top view of modulated geometry of N_2 adsorption models on bulk SCN (left side) and SCNNSs-550 (right side) (reprinted with permission under license no. 4802920063823).[113]

with brookite TiO_2, the rate of electron transfer was considerably enhanced as depicted by PL analysis (Fig. 14a). In another example, plasmonic Au NPs were coupled with defect induced crumpled GCN nanolayers synthesised *via* an alkali-supported post-calcination pathway to promote the dissociation kinetics of carriers and modify the photoactivity.[105] It was observed that GCN with N-vacancies showed relatively more substantial contacts with Au NPs and, as a result, Au NPs co-existing as Au and $Au^{(\delta-)}$ chemical states fostered plasmonic properties of the system. This synergistic coupling led to optimal light harvesting along with improved charge separation kinetics, collectively resulting in boosted photoefficacy. Precisely, a unique combination of defective GCN with co-existed Au and $Au^{(\delta-)}$ chemical states fostered light absorption through surfaced plasmonic resonance and injected photo-illuminated electrons to GCN. As a whole, vacancy defect engineering in metal-free GCN seems to provide superior dissociation of excitons to amend overall photoactivity.

4.3 Increasing surface photoreaction kinetics

As reviewed earlier, vacancy defect creation in GCN serves as a key strategy to amend not only light absorption ability but also foster the charge carrier kinetics. However, photoactivity of a semiconductor material is greatly influenced by the unavailability of appropriate active sites and poor adsorption abilities.[106–108] Due to low surface reaction kinetics, the unused photocarriers can either get recombined or get involved in unwanted photoreactions. Vacancy engineering in GCN can considerably improve the photocatalytic surface reactions by modulating surface properties of semiconductor material. Surface vacancy defects in a semiconductor photocatalyst synergistically enhance the adsorption as well as activation of reactant species. For instance, generation of defects on the surface of a photocatalyst induces the adsorption through electrostatic force of interaction between oppositely charged defective surface and reactant molecules.[109] Also, by the introduction of point defects, activation of adsorbed species (by surface-induced photocarriers) as well as surface photoreactions (by vacancies and dopants) can be simultaneously increased.[110] Along with that, defect modified surfaces can enhance the selectivity of products by providing distinct reaction pathways due to the significant difference in adsorption and dissociation routes.[111] Liang *et al.* modulated GCN by creating distinct nitrogen-vacancy density and provide physicochemical insights for the effect of N-vacancies on H_2 generation and pollutant degradation.[112] Generation of vacancy defects in GCN effectively manoeuvres the surface of GCN by providing porous surfaces and altered specific surface areas with exposed active sites. Defect engineering not only modulated surface sites but also improved the charge diffusion on the surface to boost the photocatalytic performance. To evaluate the porous structure of GCN, the N_2 adsorption–desorption isotherm was utilised, which demonstrated a type-IV adsorption isotherm (Fig. 14b). Moreover, N-vacancy induced GCN calcined at an optimal temperature of 650 °C (represented as NVCN-3) displayed the highest surface area of 49.7 $m^2\ g^{-1}$ (Fig. 14c) with increased pore volume and mean diameter, thus offering superior reactive sites for photocatalytic surface reactions.

To enhance the absorption and to improve the photo-assisted N_2 fixation performance of GCN, Cao *et al.* designed ultrathin porous GCN nanosheets doped with sulphur (represented as SCNNSs) having a large specific surface area induced by C-vacancies.[113] The as-obtained porous sheets of GCN modulated by sulphur doping and C-vacancies showed exceptional photoefficacy due to ubiquitously present active surface reaction sites as well as superior charge isolation ability. Fig. 14d depicts an increased surface area of the SCNN sample (75.24 $m^2\ g^{-1}$) with 0.205 $cm^3\ g^{-1}$ pore volume, which is significantly more than that of bulk GCN. As a result, exposed surface sites induced due to C-vacancy and S-doping fostered adsorption of N_2 onto the surface of SCNNSs and accelerated N_2 fixation kinetics. In order to investigate the effect of C-vacancies on photo-assisted N_2 fixation, N_2 temperature-programmed desorption (TDP) analysis was carried out as depicted in Fig. 14e. For bulk GCN and SCNNSs, one peak was observed at 175 °C and other at ~270 °C representing physical and chemisorption of N_2 samples, respectively. Moreover, SCNNS samples showed relatively stronger physical adsorption attributed to the increased exposed surface area and superior chemisorption due to the presence of C-vacancies. Further investigation proved that adsorption of N_2 was facilitated over defective sites having C-vacancies with an adsorption energy of −0.665 eV, which was 1.99 times higher than that of bulk GCN (Fig. 14f). Thus, chemisorption was supported over the C-vacancy region in SCNNSs as compared to bulk GCN. In a similar study, C-vacancy modified GCN exhibited a superior rate of H_2O_2 production under the exposure of visible light.[69] The introduction of C-vacancies in GCN modified the route of H_2O_2 generation from two-step indirect reduction (single electron) to one-step direct reduction (two-electron). The extent of O_2 adsorption on the photocatalyst surface is proportional to the exposed surface area, and defective GCN showed a relatively higher surface area (9.4 $m^2\ g^{-1}$) than bare GCN (8.8 $m^2\ g^{-1}$) as shown in Fig. 15a. TPD investigations revealed that defect modified GCN exhibited more muscular chemisorption strength of O_2 since it acted as a Lewis acid containing a single electron and the nitrogen atoms of amino groups at defect sites behaved as a Lewis base (Fig. 15b). Of note, chemical adsorption regions are generally referred to as reaction centres used to activate adsorbates. As a result, molecular oxygen can be easily reduced on defect induced GCN as supported by linear sweep voltammetry (LSV) analysis. Fig. 15c showed that the LSV curve for the oxygen reduction reaction of defect induced GCN was higher than that of GCN, suggesting superior activation of molecular oxygen by carbon vacancies (Fig. 15d).

In order to improve surface adsorption and to activate the adsorbates, hybridising defect rich photocatalysts with co-catalysts or conducting materials is another effective strategy.[104–106] Precisely, incorporation of conducting material with a semiconductor photocatalyst acts as trapping site for photoexcited excitons to boost their isolation and serves as redox reaction sites.[105,114,115] Exploration of metal-free conducting material with superior features to enhance optical as well as

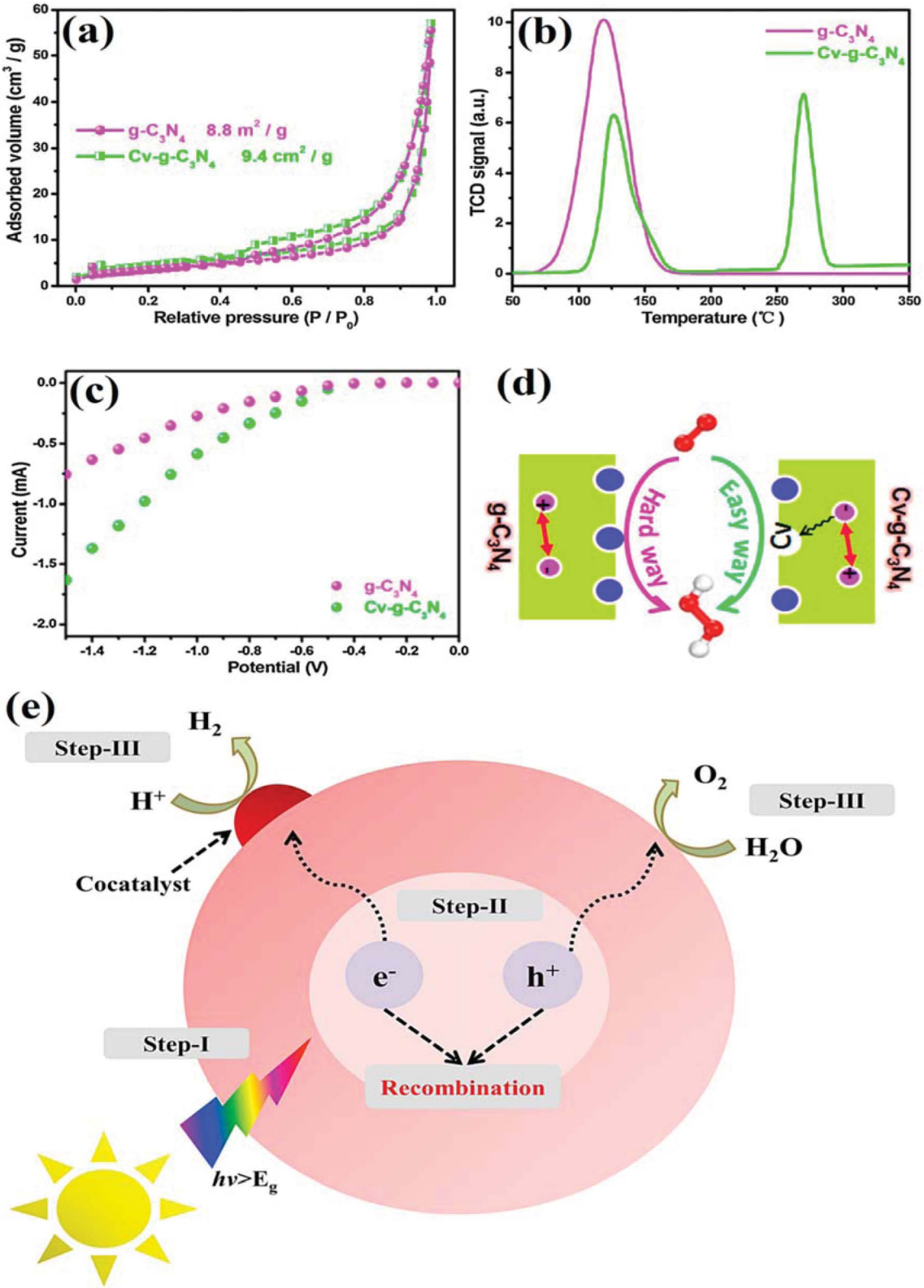

Fig. 15 Schematic illustration of (a) N_2 adsorption–desorption isotherms of GCN and vacancy induced GCN (C_v-g-C_3N_4); (b) TPD spectra of GCN and C_v-g-C_3N_4; (c) linear sweep voltammetry (LSV) curves of GCN and C_v-g-C_3N_4; and (d) representation of facile molecular reduction on C_v-g-C_3N_4 by C-vacancy (adapted with permission under license no. 4802920609594, Copyright 2016 Elsevier).[69] (e) Primary mechanism showing the steps of photocatalytic water splitting under solar light illumination.

electronic properties of defect rich semiconductor photocatalysts is a fascinating approach. Inspired by this, Liu *et al.* designed N-doped carbon quantum dot (NCD) modulated defect induced GCN (DCN) *via* the impregnation method and utilised it for dual applications.[116] The resulting hybrid 1% NCD/DCN was reported to possess a porous ultrathin structure containing a superior specific surface area with sufficient exposed active sites for photocatalytic reactions. Moreover, the synergic coupling of N-vacancy modified GCN with NVDs not only increased the visible light absorption due to the up-conversion phenomenon but also fostered the separation of photoinduced excitons. As a result, the hybrid system containing DCN and a metal-free co-catalyst exhibited improved photocatalytic performance.

Summarily, defect engineering significantly modulated each photocatalytic step to amend the overall photocatalytic efficacy of GCN. The three main consecutive photocatalytic steps, namely optical absorption, charge separation and surface photoreactions are complimentary and can be facilely modified through the generation of vacancy defects. Notably, the overall photoactivity of any semiconductor photocatalyst strictly relies on these steps and through an appropriate approach, all the three steps can be consistently promoted to achieve superior performance.

5. Photocatalytic applications

Previously discussed analyses suggested that defect engineered GCN exhibited tuned optoelectronic properties, improved charge-carrier kinetics, and amended surface photoreactions to accelerate various photocatalytic applications substantially. The following section will systematically summarise the role of defect engineered GCN photocatalysts in different photocatalytic applications involving solar to fuel energy conversions and removal of pollutants.

5.1 Water splitting

Photocatalytic water splitting under the exposure of solar light has been dramatically exploited as an efficient approach for H_2 generation after the breakthrough discovery by Honda and Fujishima in 1967.[15,117–120] Generally, the photocatalytic water splitting phenomenon as illustrated in Fig. 15e, can be summarised by the following three steps: (I) absorption of a photon by a semiconductor photocatalyst which causes excitation of electrons from the lower energy VB to the CB, leaving holes behind; (II) interfacial migration and isolation of photocarriers to the surface of the photocatalyst; (III) participation of photocarriers in a redox reaction to dissociate water into H_2 and O_2. Therefore, it is essential that the band edge positioning of the photocatalysts must be suitable to trigger the water splitting reaction. Precisely, the CB of a photocatalyst should lie at more negative potential than the redox potential of H^+/H_2 (0 V *vs.* NHE) and the VB edge potential should be more favourable than the redox potential of O_2/H_2O (1.23 V *vs.* NHE).[121] The process of water splitting by the involvement of photocarriers can be presented *via* the following redox reactions:

$$2H_2O(l) \rightarrow O_2(g) + 2H_2(g),\ E^0 = 1.23\ V,\ \Delta G^0 = +237\ kJ\ mol^{-1} \quad (1)$$

The oxidation and reduction half-cell reactions occurring at the anode and cathode, respectively at low pH can be represented as:

$$2H_2O(l) + 4h^+ \rightarrow O_2(g) + 4H^+(aq),\ E^0_{ox} = 1.23\ eV \quad (2)$$

$$2H^+ + 2e^- \rightarrow H_2,\ E^0_{Red} = 0\ eV \quad (3)$$

Thus, extra photon energy should be supplied by the photocatalyst in order to overcome the energy barrier of 1.23 eV for the facile functioning of the photocatalysis process. However, inappropriate band edge potentials and recombination of photoexcited carriers drastically hinder the overall photocatalytic efficiency. As reviewed in the previous section, defect engineering significantly stimulates the three necessary sequential steps of photocatalysis and improves the photocatalytic performance of semiconductor material. In that regard, Liu *et al.* smartly reconstructed GCN by utilizing molten salt post-treatment and fostered polycondensation and deamination which resulted in the N-defective structure ($g\text{-}C_3N_x$) enriched with superior optoelectronic features, higher conductivity and improved charge separation ability.[60] The synergism between optimal polymerisation, narrowed bandgap energy, and effective isolation of photocarriers fostered the H_2 production extent up to 403 μmol h^{-1}, 2.2 times higher than pristine GCN (Fig. 16a and b). The presence of N-vacancies in the $g\text{-}C_3N_x$ sample was evaluated with the tuned bandgap alignment (lowering of CBM positioning) evaluated through XPS analysis which was attributed to the redistribution of electrons to the carbon atoms situated at vacancy sites. In a similar study, Shan *et al.* fabricated N-vacancy rich tubular GCN with increased π-conjugation *via* thermal-polymerisation of pyridinium modulated H-bonding melamine–cyanuric acid supramolecular (PHMCS) precursor formed by hydrothermal treatment of melamine mixed with ionic liquid (pyridinium alkaline) (represented as AIL-2.0-CN).[122] The presence of the pyridinium alkaline ionic liquid helped in the conversion of melamine to cyanuric acid for the formation of PHMCS, generation of N-vacancies and tuning the electronic band structure of the as-synthesised GCN sample. Synergistic alteration in bulk GCN resulted in the increased photocatalytic H_2 evolution rate of 1284 μmol g^{-1} h^{-1} (having 4.2% of quantum efficiency at $\lambda > 420$ m) which was about 13.6 times higher than bulk GCN (B-CN). The enhanced H_2 evolution rate was due to the presence of electron-rich N-groups, which acted as the electron donor, while conjugated aromatic rings acted as the electron acceptor. As a result of acceptor–donor interactions, the charge carrier transference and excitation process were significantly stimulated. On the other hand, the presence of N-vacancies modulated the electronic band structure along with suppressed recombination of excitons. The comparative rate of H_2 generation and the process of H_2 evolution over modulated tubular GCN are shown in Fig. 16c and d. Thus, a fascinating approach of tuning the conjugation and polymerisation with defect engineering can substantially accelerate the photocatalytic performance of GCN.

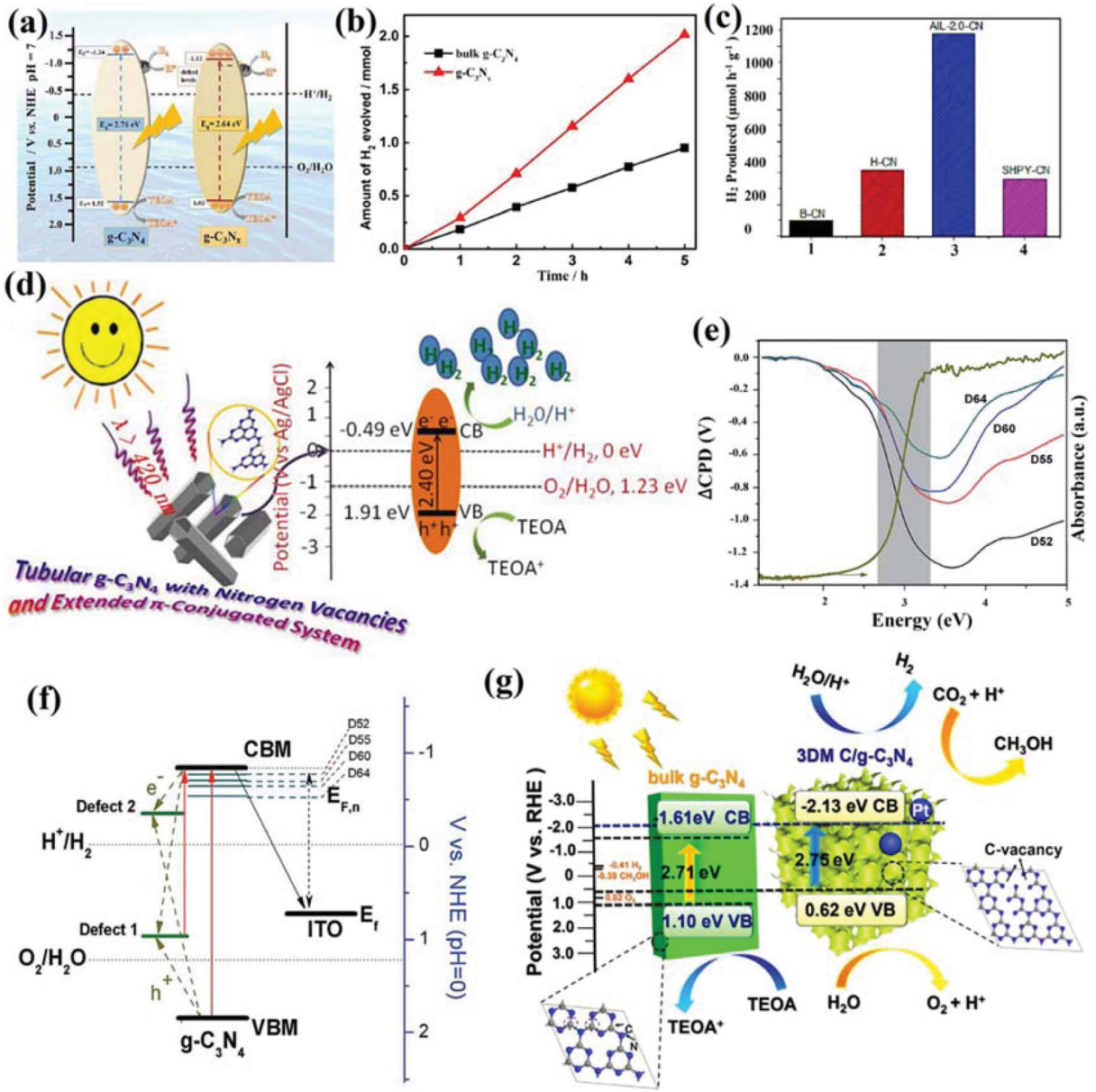

Fig. 16 (a) Schematic illustrating the optical absorption and charge separation mechanism by bare GCN and defect induced GCN (g-C_3N_x) and (b) time courses of photocatalytic H_2 production rate over bulk GCN and g-C_3N_x (reproduced with permission under license no. 4804321472963, Copyright 2018 Elsevier).[60] (c) Schematic representation of the rate of photocatalytic H_2 production over different samples involving B-CN, H-CN, AIL-2.0-CN, and SHPY-CN and (d) mechanistic insight into the process of photocatalytic H_2 production over tubular GCN sample with N-vacancies and extended π conjugation (reproduced with permission under license no. 4804820092564, Copyright 2019 Wiley).[122] (e) SPV spectra of different defect induced samples obtained by thermal treatment at various temperatures (D64 – 640 °C, D60 – 600 °C, D55 – 550 °C and D52 – 520 °C) on ITO substrate *vs.* UV-vis spectrum of D52 sample. The grey bar depicts the optical bandgap of the material. (f) Schematics of energy level diagram of GCN with defective states (defect 1 at +97 V and defect 2 at −0.38 V) and ITO (+0.76 V) (reproduced with permission under license no. 1027568-1, Copyright 2014 Royal Society of Chemistry).[123] (g) Schematics of possible band structures of g-C_3N_4 and 3DM C/g-C_3N_4 and the probable photocatalytic process of H_2 production and CO_2 reduction (reproduced with permission under license no. 4852401137294, Copyright 2020 Elsevier).[125]

As discussed earlier, the generation of defects sometimes act as a recombination site for the photoinduced excitons and inhibits the overall photocatalytic performance. By identifying the energy levels and chemical behaviour of defects, their generation can be significantly controlled, and the aforementioned problem can be addressed. For example, Wu *et al.* utilised surface photovoltage (SPV) spectroscopy along with specific other techniques to investigate the effects of thermal treatment on defect generation in GCN.[123] The report revealed significantly deprived photoactivity of GCN for H_2 evolution with increasing temperature from 520–640 °C. For SPV detection, GCN suspension was coated over Indium Tin Oxide (ITO)

covered glass at room temperature. H_2 evolution experiments were performed using 20 vol% methanol solution (sacrificial agent) with a Pt co-catalyst subjected to light exposure. SPV analysis inferred the monoatomic loss of photovoltage with increasing temperature due to the loss of photocarriers which lowered the quasi-Fermi energy level of the irradiated sample as shown in Fig. 16e and f. A sub-gap photovoltage property was achieved due to the introduction of defective states at +0.97 V and −0.38 V. The synergy of built-in electronic states fostered migration of photocarriers and accelerated the photocatalytic H_2 production. Other than thermal treatment, the self-assembly method was also utilised to form GCN having distinct morphologies with N-defects which not only exhibited enlarged π–π conjugation but also possessed thinner lamellar structures and increased the rate of H_2 evolution by 8910.7 μmol g^{-1}, about 9.9 times higher than pristine GCN.[124] In a fascinating study, Wang *et al.* constructed C-vacancy modified 3D macroporous GCN (3DM C/g-C_3N_4) using a polymethylmethacrylate template to expand surface reaction sites and extend visible light absorption.[125] The resulting sample exhibited exceptional photocatalytic performance for H_2 generation and CO_2 reduction, as depicted in Fig. 16g. Thin walls of 3DM C/gC_3N_4 enticed migration of excitons ensuing reduced reassembly. Besides, the increased surface area of 71.3 m^2 g^{-1} due to the construction of macropores additionally helped to stimulate the rate of H_2 production to 1.0 μmol m^{-2} h^{-1} inferring the significance of active surface sites. The macroporous structure also acted as different surface sites by accommodating reaction molecules at the inner surface region, while C-vacant sites served as traps to capture photo-illuminated electrons and synergistically enhance the photoefficacy of 3DM C/g-C_3N_4. Combining C-vacancies with the holey structure formation with in-plane holes in GCN is another unique approach to increase the rate of photocatalytic H_2 production.[57] The resulting sample of holey GCN with C-vacancies (HGCN) showed a higher specific surface area with exposed active edges, reaction sites and fast cross-plane diffusion kinetics of photocarriers which remarkably enhance the photocatalytic efficacy. Also, collective results from DRS and Mott–Schottky analysis confirmed the extended visible light response with low flat potential and high donor density providing thermodynamically favourable photoreaction kinetics. In contrast with bulk GCN (BGCN), the HGCN photocatalyst exhibited a superior H_2 production rate of 82.9 μmol h^{-1} which was about 20 times higher than BGCN. In a similar study, surface C-vacancies and subsequent P-dopants were introduced in GCN *via* thermal polymerization of sodium pyrophosphate assisted hydrothermal treatment of melamine.[126] The resulting rod-like morphology with C-vacancies boosted the photocatalytic H_2 production rate due to extended visible light absorption caused by multiple reflections and superior charge separation induced by C-vacancies and P-doping. The presence of P-atom and C-vacancies in the structural motifs of GCN was confirmed by lowering of C 1s binding energy from 288.2 eV to 288 eV owing to increased electron density by the incorporation of P-atoms and C-vacancies which was inconsistent with the results obtained from simulation studies. As a whole, despite significant advances and achievements in this visibly driven photocatalytic field, the pilot scale applications still need appropriate designing and characterisation strategies to overcome the present challenges in this area. For instance, there are very few reports on C-vacancy induced GCN for photocatalytic H_2 generation. Moreover, the criteria of C/N-vacancy generation in GCN and its influence on rate of photocatalytic H_2 generation are still not clear. Thus, substantial research input which clarify the influential aspects of C-/N-vacancy generation in GCN is highly anticipated.

5.2 CO_2 conversion

Elevating global concerns about climate change due to increasing CO_2 levels demand an efficient approach for solar conversion of CO_2 into value-added products and fuels.[127–131] GCN with suitable reduction potential value along with the appropriate introduction of defects can substantially improve the photo-assisted selective conversion of CO_2. As depicted in Fig. 17a, visibly driven photocatalytic conversion of CO_2 mainly involves the following steps: (1) adsorption of CO_2 molecules and reductants on the surface of the photocatalyst; (2) generation of photocarriers after the absorption of visible light; (3) migration of photo-illuminated excitons on the surface of semiconductor material; (4) surface photocatalytic reactions between adsorbents and the photocarriers; (5) desorption of photo-reaction products followed by re-adsorption of reactants.[132] However, for the spontaneous conversion of CO_2 (ΔG = negative), the supplied potential should be more negative than the standard reduction potential required. The formal redox potential values (*vs.* NHE at pH = 7) which facilitate photocatalytic CO_2 reduction reactions are given in eqn (4)–(10).

$$CO_2 + 2H^+ + 2e^- \rightarrow HCOOH,\ E^0 = -0.61\ V \quad (4)$$

$$CO_2 + 2H^+ + 2e^- \rightarrow CO + H_2O,\ E^0 = -0.53\ V \quad (5)$$

$$CO_2 + 4H^+ + 4e^- \rightarrow HCHO + H_2O,\ E^0 = -0.48\ V \quad (6)$$

$$CO_2 + 6H^+ + 6e^- \rightarrow CH_3OH + H_2O,\ E^0 = -0.38\ V \quad (7)$$

$$CO_2 + 8H^+ + 8e^- \rightarrow CH_4 + 2H_2O,\ E^0 = -0.24\ V \quad (8)$$

$$2H^+ + 2e^- \rightarrow H_2,\ E^0 = -0.41\ V \quad (9)$$

$$2H_2O + 4H^+ \rightarrow O_2 + 4H^+,\ E^0 = +0.82\ V \quad (10)$$

Thus, a semiconductor photocatalyst must ensure the apt redox potential values for the accelerated photocatalytic CO_2 conversion phenomenon. For accomplishing this task, Tang *et al.* induced N-vacancies by disrupting the π–π interactions between adjacent GCN layers *via* the NH_4Cl gas template treatment and resulted in a few atomic layers of GCN nanosheets (*ca.* 1.6 nm) displaying superior photocatalytic performance.[133] The defective GCN induced with N-vacancies at different temperatures exhibited tuned electronic features with varying bandgap energies as depicted in Fig. 17b. Moreover, by introducing N-vacancy in GCN, the reduction ability was improved due to the upshifting of CB edge potential. Also, the

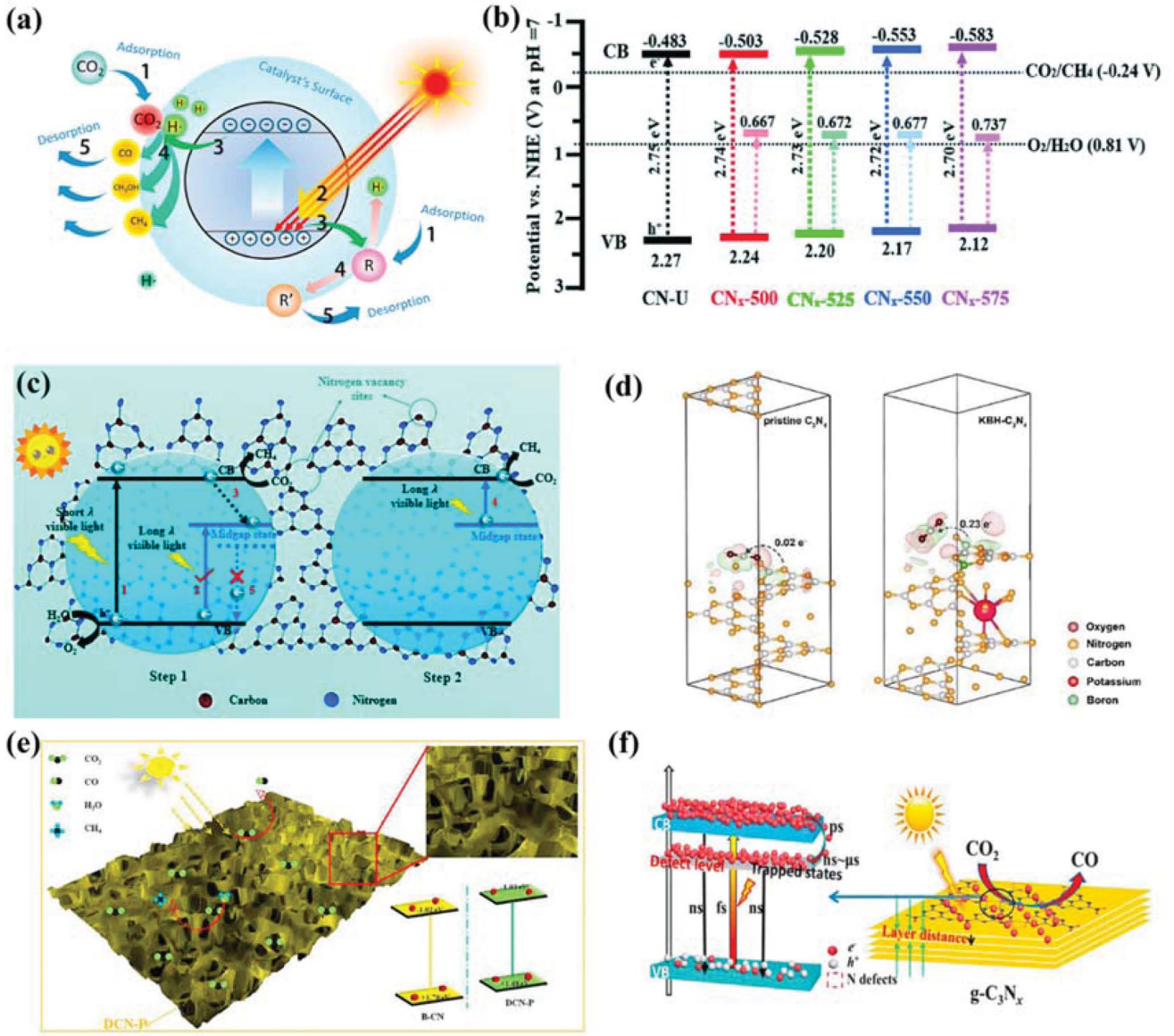

Fig. 17 (a) Mechanistic insight into the steps of photocatalytic CO_2 reduction with CO, CH_3OH, and CH_4 as possible CO_2 photoreduction products (adapted with permission under license no. 4806980481211, Copyright 2018 Elsevier).[132] (b) Schematic illustrating the electronic band configuration for distinct defect induced GCN samples (CN_x-*T*) prepared by varying temperature conditions (CN-U represents defect-free GCN), with lighter color shades depicting the midgap defective states. (c) Schematic representation of nitrogen defective GCN atomic layers for photocatalytic CO_2 reduction into CH_4 (adapted with permission under license no. 1028195-1, Copyright 2013 Royal Society of Chemistry).[133] (d) CO_2 adsorption configurations on pristine GCN (left) and KBH-C_3N_4 (right) after optimization. Charge distribution difference of CO_2 adsorption (optimized) on KBH-C_3N_4 slab with pink color depicting the gathering of electrons and green the depletion (adapted with permission under license no. 4806991318028, Copyright 2019 Elsevier).[134] (e) Schematic of dynamic process representing the generation of photocarriers and photocatalytic CO production by defect induced GCN (g-C_3N_x) under solar light illumination (adapted with permission under license no. 4807001209003, Copyright 2019 Wiley).[135] (f) Mechanistic illustration of charge transfer and photocatalytic CO_2 reduction process by defect induced DCN-P sample (adapted with permission under license no. 4807000887848, Copyright 2020 Elsevier).[136]

presence of defective midgap states just below the CB edge (formed by unpaired electrons at C-atoms) not only reduces electron excitation distance with suppressed reassembly of photocarriers but also resulted in GCN with extended optical absorption to the NIR region. Photocatalytic conversion of CO_2 into CH_4 by defective GCN with optimal N-vacancies (CN_x-550) was found to be 2.93 μmol g^{-1} with an apparent quantum yield of 0.089% which was 3.16 times more than bare GCN. The possible mechanism of CO_2 photoreduction into CH_4 by defect induced GCN is depicted in Fig. 17c. Generally, the photocatalytic CO_2 reduction was greatly influenced by low surface adsorption of CO_2 as well as deprived availability of photocarriers to accelerate photoreactions. Precisely, the untuned electronic band structure and unavailability of electron donation sites play a crucial role in affecting the CO_2 photoreduction ability. Wang *et al.* designed B and K co-doped GCN with the

generation of controlled N-vacancies (KBH-C_3N_4) which showed electron-rich surface sites along with the tuned electronic structure to simultaneously boost the adsorption and activation of CO_2.[134] As a result, the KBH-C_3N_4 exhibited a 5 h photocatalytic CH_4 and CO production rate of 5.93 μmol g^{-1} and 3.16 μmol g^{-1}, respectively utilizing CO_2 and H_2O as feedstocks by avoiding the use of any hole scavenger. The CO_2 adsorption process was measured by slab models of both GCN and KBH-C_3N_4, as shown in Fig. 17d. The observations indicated deprived adsorption energy of CO_2 at a favourable position of GCN (−0.093 eV) which is four times less than that of KBH-C_3N_4 (−0.361 eV). Moreover, defective sample, *i.e.* KBH-C_3N_4, exhibited superior migration of electrons at the surface (observed by Bader charge analyses) which substantially nurtured the activation followed by the reduction of CO_2.

As discussed earlier, the synergic virtue of defect engineering in achieving effective visible light absorption, charge isolation and superior surface sites instigated the exploration of fascinating routes for the designing of high-performance semiconductor photocatalysts. For example, the generation of N-vacancies at two different positions in GCN typically at uncondensed terminal NH_x sites and tricoordinated N-atoms, significantly improved the lifespan of photo-illuminated carriers.[135] Moreover, the deprived stacking distance between the layers of GCN nanosheets facilitated the transmission of charge carriers onto the GCN surface. This appropriate arrangement with the introduction of defects (Fig. 17e) resulted in improved CO_2 photoreduction into CO (56.9 μmol g^{-1} h^{-1}), roughly eight times more than pure GCN. Typically, after the ultrafast time scale (ps) isolation of photocarriers, the geminate reassembly and bimolecular reassembly (ns–μs) were significantly overruled. For further stimulating the separation of excitons, N-defects acted as trapping sites (for both long-lived (μs) and shortly lived (ns) photocarriers), while the thin layer nanosheets facilitated easy migration of carriers for their participation in surface photoreduction reactions. In a similar study, Ma *et al.* reported porous, N-vacancy modified GCN (DCN-P) with superior reaction sites, efficient CO_2 adsorption ability and a modulated electronic bandgap structure which displayed significantly enhanced photoreduction of CO_2 into CO (19.7 μmol g^{-1}) and CH_4 (μmol g^{-1}).[136] The process of CO_2 reduction by DCN-P under visible light exposure is depicted in Fig. 17f, and the reduction reactions are given by eqn (11)–(15) as follows:

$$\text{DCN-P} + \text{photon} \rightarrow e^- + h^+ \quad (11)$$

$$CO_2(g) + e^- \rightarrow CO_2^*(\text{activated}) \quad (12)$$

$$H_2O \rightarrow H^+ + OH^- \quad (13)$$

$$CO_2^*(\text{activated}) + 2H^+ + 2e^- \rightarrow CO + 2H_2O \quad (14)$$

$$CO_2^*(\text{activated}) + 4H^+ + 8e^- \rightarrow CH_4 + 2H_2O \quad (15)$$

On the other hand, C-vacancies in GCN helped to reduce the exciton effect, which helped to dissociate more charge carriers and boosted the generation of active species for superior adsorption and activation of CO_2.[137] Precisely, the EPR spectroscopic analysis revealed $^{\bullet}O_2^-$ radicals as reactive species involved in photoconversion of CO_2 into CO, which was facilitated by the inhibited exciton effect and accelerated generation of photocarriers by C-vacancy induced GCN (GCN510). However, in the case of pristine GCN, the presence of the conspicuous exciton effect fostered the generation of singlet oxygen ($^1O_2$) rather than $^{\bullet}O_2^-$ radicals due to a deprived generation of photocarriers leading to a reduced rate of CO_2 photoconversion. Besides, combined results from TPD analysis and DFT calculations helped to scrutinise the impact of C-vacancies on the CO_2 adsorption phenomenon. Both the analysis confirmed two stable adsorption configurations with a superior adsorption energy of −0.463 eV in the case of GCN510, which was notably high from pristine GCN (−0.183 eV). Thus, in light of the importance of CO_2 adsorption capacity on the surface of GCN, generation of intrinsic active sites could be a more practical approach. For instance, increasing intrinsic amino groups in GCN along with the generation of vacancy defects can simultaneously improve CO_2 adsorption/activation and surface photoreduction kinetics. In that regard, Sun *et al.* smartly designed GCN enriched with intrinsic CO_2 adsorption sites by forming more amino groups and involving electron promoters by generating C-vacancies and incorporating K-ions through KOH assisted chemical activation.[138] The elemental analysis helped to achieve an optimal amount of amino groups in GCN by using KOH treatment which also confirmed the removal of C2 carbon (carbon of tri-*s*-triazine rings) resulting in the formation of C-defects. The sample with an optimal ratio of amino groups and K and C-defects (0.1K-AUCN) showed about 7.7 times higher CO_2 adsorption (∼3.5 wt%) than the untreated GCN (UCN). Thus, the process of photoreduction of CO_2 to useful hydrocarbons strictly depends on tuned bandgap alignments, adsorption ability, activation by surface electrons and subsequent desorption of products. On that note, defect engineering of GCN semiconductor photocatalysts seems to be a promising strategy for a synergistic increment in optoelectronic features and adsorption/activation kinetics required for efficient CO_2 conversion. However, more stringent efforts are required to attain real-time applicability and understanding of mechanistic insight in terms of C-/N-vacancy creation and its subsequent influence on photo-assisted CO_2 reduction.

5.3 N_2 fixation

Currently, the reduction of N_2 into NH_3 is mostly carried out by the Haber–Bosch process in the industry, which is a highly cost-ineffective route demanding high temperature and pressure conditions.[139,140] Under such circumstances, the exploitation of more sustainable and environmentally friendly techniques for N_2 fixation is highly thriving. A photocatalytic N_2 fixation is a fascinating approach for the synthesis of ammonia under near-ambient circumstances.[141,142] Moreover, photocatalysts modulated by defect engineering provide even better photocatalytic N_2 fixation efficiency as it provides remarkable physicochemical features to overcome intrinsic bottlenecks. It is a well-known fact

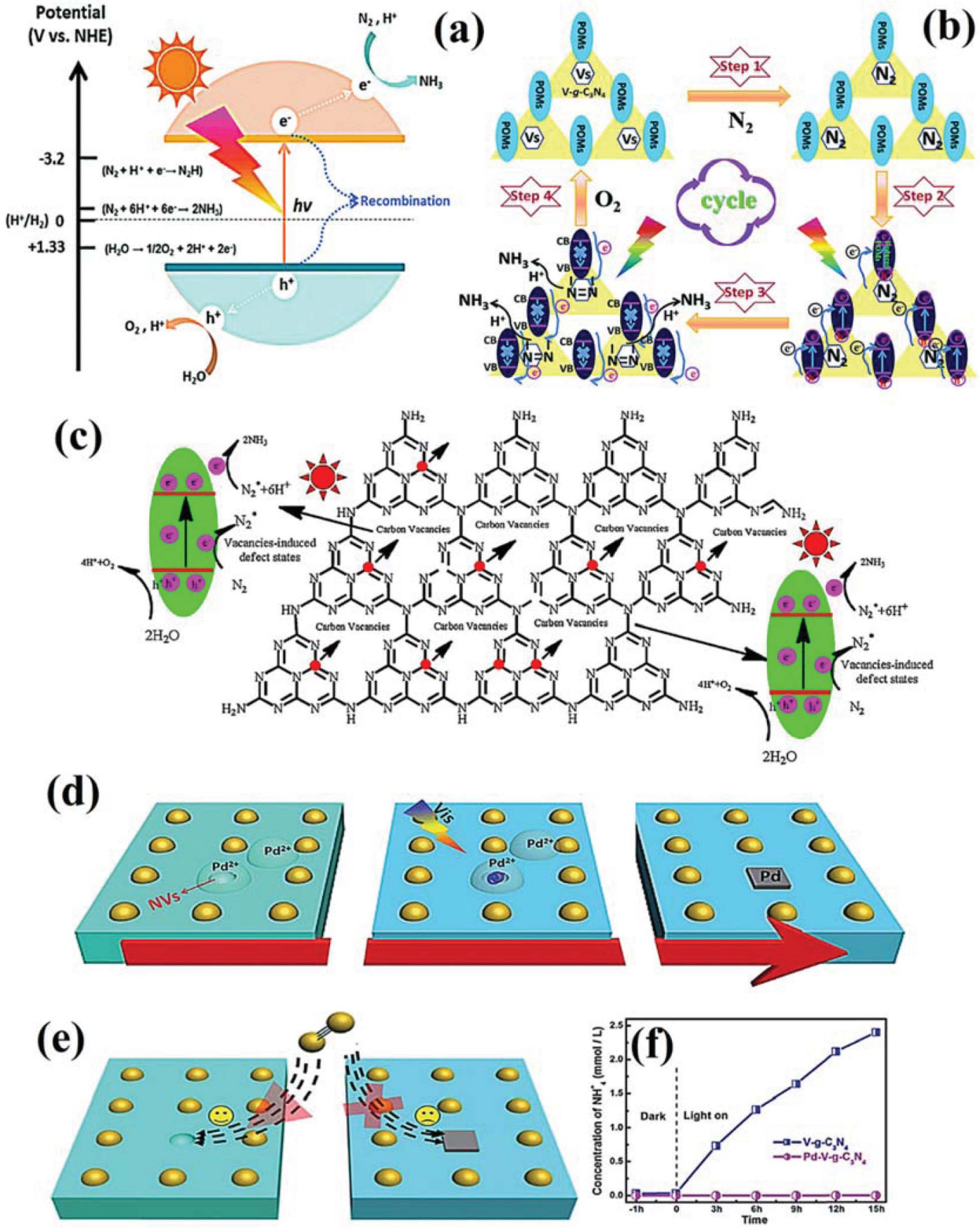

Fig. 18 (a) Schematics of semiconductor driven photocatalytic N_2 fixation into NH_3 with redox potential scale depicting water splitting and dinitrogen hydrogenation (reprinted with permission under license no. 1029338-1, Copyright 2018 Royal Society of Chemistry).[143] (b) Illustrating the process of photocatalytic N_2 fixation by V-g-C_3N_4 and POMs system (reprinted with permission under license no. 1028622-2, Copyright 2019 Royal Society of Chemistry).[144] (c) Mechanistic insight into the photocatalytic N_2 fixation using defect induced HGCN sample (reprinted with permission under license no. 4810761467174, Copyright 2020 Elsevier).[145] Schematic illustration of (d) selective deposition of Pd NPs onto N-vacancy induced GCN (V-g-C_3N_4); (e) N_2 will not be adsorbed on the Pd NPs due to considerable work function; (f) Pd loading can significantly suppress the rate of photocatalytic N_2 fixation (reprinted with permission under license no. 1028628-1, Copyright 2015 Royal Society of Chemistry).[146]

that photocatalytic redox reactions much depend upon reduction potentials of adsorbates along with band-edge positioning of semiconductor photocatalysts (Fig. 18a). For instance, CB edge potential should be located at a more negative position than the reduction potential required for N_2 hydrogenation, whereas VB potential should be at a more positive position than that of oxygen evolution potential.[143] Based on this, the formal reduction potentials (V *vs.* NHE at pH = 7) corresponding to the hydrogenation reactions involved in photocatalytic N_2 fixation can be presented *via* eqn (16)–(24) as follows:

$$H_2O \rightarrow 1/2O_2 + 2H^+ + 2e^-,\ E^0 = 0.81\ V \quad (16)$$

$$2H^+ + 2e^- \rightarrow H_2,\ E^0 = -0.42\ V \quad (17)$$

$$N_2 + e^- \rightarrow N_2^-,\ E^0 = -4.16\ V \quad (18)$$

$$N_2 + H^+ + e^- \rightarrow N_2H,\ E^0 = -3.2\ V \quad (19)$$

$$N_2 + 2H^+ + 2e^- \rightarrow N_2H_2,\ E^0 = -1.10\ V \quad (20)$$

$$N_2 + 4H^+ + 4e^- \rightarrow N_2H_4,\ E^0 = -0.36\ V \quad (21)$$

$$N_2 + 5H^+ + 4e^- \rightarrow N_2H_5^+,\ E^0 = -0.23\ V \quad (22)$$

$$N_2 + 6H^+ + 6e^- \rightarrow 2NH_3,\ E^0 = 0.55\ V \quad (23)$$

$$N_2 + 8H^+ + 8e^- \rightarrow 2NH_4^+,\ E^0 = 0.27\ V \quad (24)$$

Of note, it is of utmost interest to maintain the small bandgap energy of semiconductor photocatalysts to increase visible light absorption and to avoid the reassembly of photocarriers. So far, both of these conditions can be fulfilled by defect engineered GCN as reviewed earlier. For instance, Li *et al.* reported a Dawson-type polyoxometalate (POM) based N-vacancy induced GCN (V-g-C_3N_4) (POM@V-g-C_3N_4) nanohybrid, which exhibited remarkable performance in the activation and subsequent dissociation of N_2.[144] Excellent N_2 reduction efficacy (214.6 μmol L^{-1} h^{-1}) was caused by extended optical absorption (200–900 nm), higher N_2 activation by POM and suppressed recombination of photocarriers. The main steps involved in the process of photoassisted N_2 reduction (Fig. 18b) were: (i) adsorption of N_2 by V-g-C_3N_4; (ii) generation of abundant photocarriers by POMs under the exposure of light; (iii) activation of N_2 molecules by surface-induced carriers and subsequent formation of NH_3 by combining with protons; (iv) reformation of POMs by reacting with oxidants (O_2) to maintain the sustainability. Ge *et al.* reported C-vacancy induced holey GCN nanosheets (HGN) prepared from the thermal treatment of bulk GCN (BGCN) for optimal photoreduction of N_2 into NH_4^+ with a maximum efficiency of about 25.54 mg g_{cat}^{-1} L^{-1} h^{-1}.[145] Photofixation of N_2 was performed using hole scavengers under visible light illumination, as shown in Fig. 18c. The defective structure of HGCN accelerated N_2 adsorption and its reduction through surface migrated electrons by converting it into a transient charged electronic state N_2^* with a relatively lower energy barrier for the photoreduction reactions.

The N_2 photofixation performance of bulk GCN is greatly influenced by defect engineering, especially by generating N-vacancies in the structural units of GCN. Precisely, N-vacancies in GCN facilely improve the selective adsorption of molecular nitrogen followed by its activation as the N-vacancies and the N-atom of N_2 share shape and size complementarity. Additionally, altered optical and electronic features along with superior interfacial migration of electrons to improve photoreduction ability boost the overall photocatalytic performance. To prove this statement, Dong *et al.* compared the photofixation ability of vacancy defected GCN (V-g-C_3N_4) with Pd loaded V-g-C_3N_4 (Fig. 18d–f).[146] The study proved the adsorbed Pd selectively occupied N-vacant positions containing photo-illuminated electrons on the surface of V-g-C_3N_4, as shown in Fig. 18d. Due to the considerable work function of platinum metal, N_2 molecules were unable to be adsorbed (Fig. 18e). Consequently, blocked N_2 adsorption sites (N-vacancies) on the V-g-C_3N_4 surface by modification of Pd, photoreduction of N_2 considerably decreased (Fig. 18f). Thus, N_2 adsorption occurs mainly on N-vacant sites in the V-g-C_3N_4 where surface-induced electrons enhanced the selective photofixation efficacy. Other than N-vacancies, the formation of C-vacancies in porous nanosheets of sulphur doped GCN (SCNNSs) also accelerated the adsorption and photoreduction of N_2 with a maximum rate of 5.99 mM g_{cat}^{-1} h^{-1} in 4 h under the exposure of visible light.[113] Typically, photoinduced CB electrons in SCNNSs were captured by C-vacancies which were further transferred to surface adsorbed N_2 to form NH_4^+ and H_2O from the reaction mixture and provided protons for the photoreduction reaction. In a similar study, the formation of an ultrathin structure with surface C-defects generated *via* a high-temperature peeling process endowed GCN with superior N_2 adsorption and subsequent conversion into ammonia (54 μmol L^{-1}) without involving any sacrificial agent and co-catalyst.[147] Generation of surface C-vacancies and the ultrathin structure of GCN benefitted the diffusion of charge carriers to surface active sites resulting in efficient adsorption/activation of N_2 and its subsequent conversion into ammonia. Consequently, from the above-reviewed literature, it is quite evident that unique architecture effects and controlled defect formation greatly manoeuvre surface adsorption sites along with electronic features in GCN for significant amendment in N_2 photoreduction efficacy. On the one hand, the size and shape symmetry of N-vacancies and N-atoms of N_2 facilitated the adsorption and activation kinetics beneficial for photocatalytic N_2 conversion. On the other hand, surface C-vacancies promote charge carrier kinetics and act as active centres for photo-reduction reactions.

5.4 Pollutant mitigation

Rampant industrial activities are playing a significant role in increasing recalcitrant pollutants in the environment, leading to adversely growing environmental concerns which have become a pressing global challenge. The advanced oxidation process (AOP) involving heterogeneous photocatalysis driven under visible light exposure is a fascinating technique for the photocatalytic oxidation of aqueous as well as gas-phase

pollutants.[148–152] Precisely, the critical feature of heterogeneous photocatalysis is photoassisted oxidation of pollutants to benign substances.[153] The mechanistic insight involving the generation of excitons and the subsequent photodegradation of pollutants are depicted by eqn (25)–(31):[154]

$$GCN + h\nu \rightarrow e_{CB}^{-} + h\nu_{VB}^{+} \quad (25)$$

$$h\nu_{VB}^{+} + OH_{surface}^{-} \rightarrow OH^{\bullet} \quad (26)$$

$$h\nu_{VB}^{+} + H_2O_{adsorbed} \rightarrow OH^{\bullet} + H^{+} \quad (27)$$

$$e_{CB}^{-} + O_{adsorbed} \rightarrow O_2^{\bullet -} \quad (28)$$

$$h\nu_{VB}^{+} + \text{pollutants} \rightarrow \text{oxidation products} \quad (29)$$

$$OH^{\bullet} + \text{pollutants} \rightarrow \text{degradation products} \quad (30)$$

$$e_{CB}^{-} + \text{pollutants} \rightarrow \text{reduction products} \quad (31)$$

Hitherto, significant research efforts have been involved in developing superior techniques to modify the photocatalytic features of semiconductor material, and defect engineering is one the most promising approaches. For example, Wang *et al.* designed porous GCN nanosheets by installing N-vacancies (D-g-C_3N_4) *via* a simple polymerisation process and the as-synthesised defected sample exhibited a 7.45 fold higher rate for meropenem (MER) degradation, as compared with a conventional GCN sample.[78] A possible photocatalytic degradation mechanism for MER facilitated by an optimal defect rich D3-g-C_3N_4 sample is shown in Fig. 19a. Instalment of N_{2C} vacancy defects manifested midgap states which suppressed the reassembly of excitons providing superior photocatalytic efficiency. Also, a porous structure with 5 mm thickness shortened the migration distance for photocarriers and stimulated the surface photoreactions. In a fascinating study, Yang *et al.* facilely promoted the electronic features of GCN by P and Cl co-doping along with the construction of N-vacancies *via* thermal condensation techniques.[155] The as-designed defective sample ClPCN-2 showed remarkable performance for the photodegradation of rhodamine B (RhB) and norfloxacin (NOR). The optoelectronic analysis proved that introducing P and Cl in the network structure of GCN along with N-deficiencies resulted in more negative CB potential, which assisted the formation of $^{\bullet}O_2^{-}$ radicals. The existence of P (by replacing graphitic C) and Cl (interstitial position) in the tri-*s*-triazine framework with N-vacancies is depicted in Fig. 19b. Boosted electronic properties, as well as photocatalytic performance, were attributed to the following reasons: (i) modulated p-conjugation in triazine rings due to the presence of N-vacancies and π–π conjugation, (ii) generation of P^{+} centres due to P–N bond polarisation and delocalisation of unpaired electrons, (iii) strong reduction potential of CB to generate $^{\bullet}O_2^{-}$ radicals, and (iv) availability of abundant electrons to participate in reduction reactions due to N-vacancies. Photocatalytic degradation of RhB and NOR by the defective ClPCN-2 sample is depicted in Fig. 19c. Zhang *et al.* smartly utilised the synergism between N-vacancies and C-dots decorated GCN (represented as C-dot@ND-g-C_3N_4) to amplify overall photocatalytic efficacy for degradation of ciprofloxacin (CIP).[156] Introduction of N-vacancies aided visible light harnessing ability by tuning the bandgap energy (found to be 2.64 eV) and simultaneously enriched charge separation. On the other hand, incorporation of C-dots acted as an efficient channel for capturing and migration of excitons providing sufficient availability to combine with oxygen. Moreover, scavenging results revealed that $^{\bullet}O_2^{-}$ scanning transmission electron microscopy (STEM) was an optimal approach for radicals while $^{\bullet}OH$ radicals worked as the main reactive species. These radical/reactive species were responsible for the CIP degradation, which was 2.5 times higher than GCN. The mechanistic mode of radiative exciton dissociation and CIP degradation is depicted in Fig. 19d.

Other than aqueous pollutants, oxides of nitrogen (NO_x) are the most common gaseous pollutants which are being transformed and removed using solar energy triggered photocatalysis. Photoinduced carriers can oxidise gaseous NO_x into particulate phase nitrates and help to purify air.[157,158] Defect engineered GCN was also exploited to utilise its potential for efficient removal of NO_x. For instance, Wang *et al.* constructed tubular GCN with N-vacancies and porous wall structures through an *in situ* soft chemical route for photo-assisted removal of NO.[159] ESR investigations revealed that $^{\bullet}O_2^{-}$ radicals played a crucial role in the photocatalytic removal of NO. From DFT calculations, the mode and energies of O_2 and NO adsorption on GCN and N-vacancy induced GCN was inferred as presented in Fig. 19e–h. Thermodynamically, molecular O_2 cannot be adsorbed on bare GCN due to high ΔE adsorption energy (0.48 eV) (Fig. 19e), while defective GCN can easily bind O_2 due to negative ΔE adsorption energy of −5.99 eV. Thus, at N-vacant sites, molecular oxygen dissociated and was easily reduced to $^{\bullet}O_2^{-}$ radicals by photoinduced electrons (Fig. 19f). Similarly, NO with high adsorption energy ($\Delta E = 0.29$ eV) was unable to bind with unbroken GCN (Fig. 19g) as compared to N-vacant GCN with less adsorption energy ($\Delta E = -5.91$ eV) as shown in Fig. 19h. Therefore, N-vacancies simultaneously accelerated adsorption abilities of O_2 and NO and stimulated photo-removal kinetics. In a similar study, Liao *et al.* also designed N-vacancy engineered GCN (represented as Nd-g-C_3N_4) with superior NO removal efficiency and the sample obtained at 600 °C with optimal N-vacancies showed the maximum NO removal rate which was 2.6 times higher than that of pristine GCN.[160] From theoretical DFT analysis, NO adsorption energies, as well as N–O bond length, were investigated to study NO removal kinetics (Fig. 19i and j). As can be seen from Fig. 19j, NO adsorption energy significantly decreased from −0.13 to −0.88 eV from bare GCN to Nd-g-C_3N_4 with elongation in the N–O bond angle from 1.17 to 1.20 Å. Thus, N-vacancies at the GCN surface promoted NO adsorption and converted it into NO^{+} (intermediate), while the reactive $^{\bullet}O_2^{-}$ radicals further transformed NO^{+} into NO_3^{-}. Consequently, generation of N-vacancies in GCN not only provides optimal reaction sites but also trap electrons for the generation of reactive species which in turn participate in photocatalytic oxidation of pollutants. Other than N-vacancies, C-vacancy modified GCN also exhibited

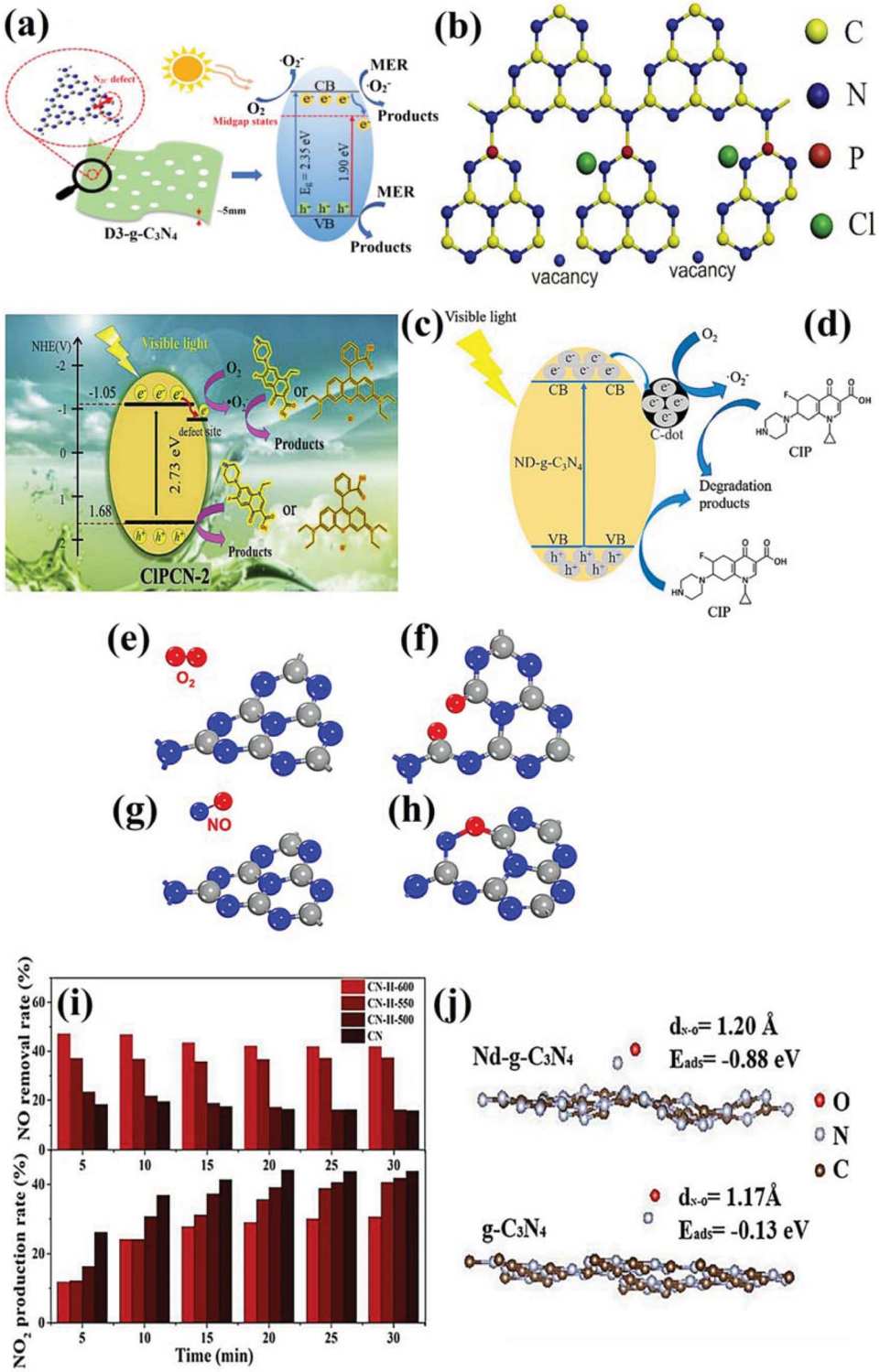

Fig. 19 (a) Schematic illustration of a possible photocatalytic mechanism for porous GCN nanosheets containing nitrogen defects (D3-g-C_3N_4) for enhanced photocatalytic removal of meropenem (adapted with permission under license no. 4852460048773, Copyright 2020 Elsevier).[78] (b) Schematic representation of possible existence of P and Cl in the structural network of GCN and (c) Mechanistic insight into the photocatalytic mechanism scheme of ClPCN-2 sample under the exposure of visible light (adapted with permission under license no. 4815761013178, Copyright 2020 Elsevier).[155] (d) Possible photocatalytic mechanism depicting CIP degradation process by C-dot@ND-g-C_3N_4 under visible light illumination (adapted with permission under license no. 4815761355787, Copyright 2019 Elsevier).[156] Schematic illustration of models of O_2 adsorption on (e) GCN and (f) N-deficient GCN after geometry optimization; Models of NO adsorbed on (g) GCN and (h) vacancy induced GCN after geometry optimization (adapted with permission, Copyright 2019 American Chemical Society).[159] Schematic illustration of (i) photocatalytic NO removal efficiency and rate of NO_2 production during NO oxidation under visible light exposure; and (j) Optimised adsorption of NO over Nd-CN and GCN samples (adapted with permission under license no. 4821200816869, Copyright 2020 Elsevier).[160]

considerable photocatalytic performance for the degradation of pollutants owing to the improved catalytic sites which facilitate adsorption and degradation of surface adsorbed pollutants. For instance, combining the porous ultrathin structure (0.9 nm thickness) with confined surface C-vacancy defects in GCN helped to improve the dissociation and transference of carriers from bulk to surface leading to improved photocatalytic degradation of RhB (96.2% after 120 min exposure of visible light).[161] The presence of C-vacancies was analysed by increased the ESR intensity and tuned bandgap alignment as observed by the XPS VBM technique. Moreover, the free radicals involved in the degradation of RhB changed from superoxide radicals for untreated GCN to superoxide as well as hydroxyl radicals for C-vacancy modified GCN. In a similar study, C-vacancy modified GCN (V_C-C_3N_4) showed an improved rate of bisphenol A degradation due to the accelerated adsorption prompted by electrostatic interaction between negatively charged molecules of bisphenol A and C-defective sites.[162] Also, the electron-deficient C-vacancy sites trapped the photoinduced electrons and fostered their migration for surface photoreactions. Thus, C-vacancies served as efficient conversion centres to capture photoexcited electrons which further reacted with surface adsorbed O_2 to produce $^{\bullet}O_2^-$ radicals, the major reactive species responsible for bisphenol A degradation. Thus, defect engineering seems to be a fascinating method to increase the generation of reactive species as well as to manoeuvre overall photocatalytic efficacy. However, the limited number of studies explaining the role of intrinsic C-/N-vacancy creation in GCN for photocatalytic pollutant degradation is still challenging for an in-depth understanding.

5.5 H_2O_2 production

Other than environmental remediation and solar energy conversions, defect engineered GCN has also been used for the photocatalytic production of hydrogen peroxide (H_2O_2), since H_2O_2 is a versatile agent widely used in various biological processes, a potent oxidant in environmental recovery applications, chemical synthetic processes, textile bleaching and in the production of detergents.[163–165] Currently, industrial production of H_2O_2 involves highly costly and non-efficient methods like anthraquinone autoxidation, different electrochemical synthesis and oxidation of alcohols.[69,166] Such processes require a large number of chemicals and high energy consumption to synthesise H_2O_2 which are hardly considered to be green methods. Therefore, photocatalytic synthesis routes driven by visible light seem to be an efficacious approach to produce H_2O_2. The photoassisted production of H_2O_2 using H_2O and O_2 is a thermodynamically uphill reaction which involves a change of 117 kJ mol^{-1} of standard Gibbs free energy. The mechanism involved in the photocatalytic H_2O_2 production is given by eqn (32)–(38) as follows:

$$2H_2O + 4h^+ \rightarrow O_2 + 4H^+ \quad (32)$$

$$O_2 + e^- \rightarrow O_2^{\bullet -} \quad (33)$$

$$O_2 + H^+ \rightarrow HO_2^{\bullet -} \quad (34)$$

$$HO_2^{\bullet -} + e^- \rightarrow HO_2^- \quad (35)$$

$$HO_2^{\bullet -} + H^+ \rightarrow H_2O_2 \quad (36)$$

$$O_2 + 2H^+ + 2e^- \rightarrow H_2O_2 \quad (37)$$

$$2H_2O + O_2 + h\nu \rightarrow 2H_2O_2,\ \Delta G^0 = 117\ \text{kJ mol}^{-1} \quad (38)$$

Thus, a photocatalytic system with suitable band edge positions and a surface structure can facilitate efficient photocatalytic H_2O_2 production. For instance, Li *et al.* smartly utilised a dielectric barrier discharge (DBD) plasma method to design N-vacancy rich GCN (PLCN-*x*) and evaluated its performance for photoassisted H_2O_2 production.[167] Experimental studies inferred that the use of plasma treatment remarkably modulated the surface morphology (by increasing surface area), optical absorption and structural features of the as-synthesised defective samples. Moreover, defect engineered N-vacant sites acted as active reaction sites which promoted adsorption of molecular oxygen and accelerated the photoreduction reaction between trapped photoelectrons and oxygen molecules for the subsequent generation of H_2O_2 (O_2 + $2H^+$(from water) + $2e^- \rightarrow H_2O_2$). Out of all the synthesised defect induced samples, PLCN-30 exhibited the highest rate of H_2O_2 production, which was 11 times more than bare GCN. Furthermore, this increased H_2O_2 production rate was attributed to exposed N-vacancy sites at an increased surface area which substantially nurtured the reduction of more oxygen molecules at the same time. In another report, Li *et al.* systematically investigated the rate of H_2O_2 production over C-vacancy modified GCN, which was found to be 14 times higher than that of pristine GCN.[69] The presence of C-vacancies in the GCN framework helped electron delocalisation by reducing the symmetry of GCN. As a consequence, the tuned bandgap (narrowed) with higher excitation of photocarriers resulted in exceptional photocatalytic performance. Also, C-vacancies in GCN not just aided as adsorption sites for molecular oxygen but also enhanced the H_2O_2 production route from two-step indirect reduction (single electron) to one-step direct reduction (two electrons) routes. Hence, the use of defect induced GCN for photoassisted production of H_2O_2 seems to be a practical and green alternative route. Several other recent examples of vacancy defect engineered GCN for various photocatalytic applications are summarised in Table 2.

In summary, rational control of vacancy defect generation in GCN seems to be particularly important as it plays a crucial role in visibly driven photocatalysis. Of note, controlled defects at the surface of GCN not only acted as active adsorption sites but also captured photoexcited electrons to stimulate the photocatalytic reactions. Through appropriate synthetic techniques, characterisation processes and a unique combination of theoretical as well as experimental results, defect engineering can be implemented smartly to utilise its potential for various environmental and energy applications.

Table 2 Recent studies on defective GCN photocatalysts for various photocatalytic applications

Sample	Designing strategy	Defect type	Characterisation	Mechanism	Application	Reaction conditions	Light source	Photoefficiency	AQE	Ref.
Defect induce GCN	Hydrogen treatment	N-Vacancy	XPS, elemental analysis (EA), and DFT	Narrowed bandgap and enhanced solar absorption	H_2 production	Aqueous triethanolamine solution (20 vol%) over 1 wt% Pt, 420 nm cut-off filter	Xe-lamp with 400 nm cutoff filter	Rate of H_2 production (defect induced GCN) = 4.8 × pristine GCN		168
g-C_3N_4–M_xU_y (M = melamine, U = Urea)	Thermal polycondensation	N-Vacancy	PL, femtosecond time-resolved DSR	Mesoporous structure with e^- trapping sites for improved charge separation	H_2 production	50 mg catalyst in 50 mL aqueous solution containing 20 vol% TEOA with $H_2PtCl_6 \cdot 6H_2O$	Xe-lamp with 400 nm cutoff filter	Rate of H_2 production (g-C_3N_4–M_1U_2) = 3.1 mmol g^{-1} h^{-1}	AQE = 74%	169
Porous GCN nanosheets with N-defects and oxygen doping (PNV-CN)	Thermal polymerisation	N-Vacancy and cyano groups	XPS, photocurrent responses, EIS, and UV-vis DRS	Improved charge migration and separation, extended optical absorption, increased active sites	H_2 production	0.05 g of PNV-CN in 100 mL aqueous solution containing 10 vol% TEOA with 3 wt% Pt	300 W Xe lamp with 420 nm cutoff filter	Rate of H_2 production (PNV-CN) = 62.4 μmol h^{-1}, 17.3 × bulk GCN	AQE = 4.0%,	170
Nanocage-like 3D porous GCN with N-defects (DCN)	Hydrothermal copolymerization	N-Vacancy	XPS and time-resolved PL	Broad visible-light response, active responsive range with more exposed active lateral edges and active sites	H_2 production	50 mg of DCN in 100 mL aqueous solution containing 10 vol% TEOA with 3 wt% Pt	300 W Xe lamp with 420 nm cutoff filter	Rate of H_2 production (DCN-550) = 92.57 μmol h^{-1}, 20.3 × pristine GCN	AQE = 3.01% at 420 nm, 2.72% at 450 nm, and 2.00% at 500 nm	171
Nitrogen-deficient graphitic carbon nitride (g-C_3N_{4-x})	Hydrothermal treatment	N-Vacancy	XPS, EA, EPR, UV-vis DRS and PL	Improved charge migration and separation and extended optical absorption	H_2 production	0.1 g of g-C_3N_{4-x} in 100 mL aqueous solution containing 10 vol% TEOA with 1 wt% Pt	300 W Xe arc lamp with 420 nm cutoff filter	Rate of H_2 production (g-C_3N_{4-x}) = 31.6 μmol h^{-1}, 3 × pristine GCN	—	172
Defect modulated GCN (CNQT)	Thermal treatment	N-Vacancy and introduction of cyano groups	XPS and theoretical calculation models	Narrowed bandgap showed red shift in the light absorption edge due to cyano groups	H_2 production	50 mg of CNQT in 300 mL aqueous solution containing 10 vol% TEOA with 3 wt% Pt	300 W Xe lamp (λ > 400 nm for 1 h)	Rate of H_2 production (CNQT) = 21.5 × pristine GCN	AQY = Ne/Np*100% = 2MNAhc/SPtλ*100%	173
	LiOH treatment and heat etching	N-Vacancy	XPS, EPR and EA	Large surface area and improved	H_2 production	50 mg of CNQT in 100 mL lactic acid		Rate of H_2 production (CN-	—	174

Table 2 (*Contd.*)

Sample	Designing strategy	Defect type	Characterisation	Mechanism	Application	Reaction conditions	Light source	Photoefficiency	AQE	Ref.
Porous CN nanostructure (CN-LT)				isolation of photoinduced excitons		solution 10 vol% with 1.5 wt% Pt	300 W Xe lamp (λ > 400 nm for 60 min)	LT) = 1.54 mmol g^{-1} h^{-1}, 19.25 × pristine GCN		
Defect modified g-C_3N_4 (CN*x*)	Thermal etching method	N-Vacancy	XPS and EA	Narrowed bandgap, increased surface area and improved charge separation	H_2 production	50 mg photocatalyst in 10 wt% TEOA solution with 3 wt% Pt	300 W Xe lamp (λ > 400 nm at 10 °C)	Rate of H_2 production (CN2) = 100 μmol h^{-1}, 11 × pristine CN	AQY = 10.38% at 420 nm and 0.53% at 550 nm	175
Cl surface defective GCN (g-$C_3N_{4-x}CL_x$)	Microwave etching	N-Vacancy and Cl doping	XPS and DFT calculations	Spongy structure with abundant surface sites and superior dissociation of radiative carriers	Photodegradation of diclofenac sodium (DCF), bisphenol A (BPA), phenol (phOH) and MB	25 mg photocatalyst into 50 mL aqueous solution containing: [MB] = 1 × 10^{-5} mol L^{-1}, [phOH] = [BPA] = [DCF] = 5 ppm	1000 W Xe lamp (λ > 400 nm)	Photodegradation rates: DCF = 100%, BPA = 88.2%, phOH = 85.7%, MB = 97%	—	176
Defect modified reduced GCN (NV-g-C_3N_4)	Thermal treatment	N-Vacancy and introduction of cyano groups	EA, FTIR and XPS	Superior visible light absorption due to downshift in VB and high oxidation efficiency	DCF degradation	50 mL of 4 mg L^{-1} DCF solution with 1 mg L^{-1} photocatalyst subjected under	350 W Xe lamp irradiation (λ > 400 nm at 25 °C)	Photodegradation of DCF = 63.9% under 180 min of light exposure	—	177
Z scheme g-C_3N_x/Bi_2WO_6	Hydrothermal method	N-Vacancy	EA and XPS	Improved visible light absorption and charge separation	MB degradation	50 mg photocatalyst into 100 mL aqueous solution containing [MB] = 1 × 10^{-5} mol L^{-1}	500 W Xe lamp	Photodegradation of MB = 83% under Xe lamp irradiation	—	178
Vacancy induced 2D mesoporous GCN (NVCN)	Two-step thermal treatment method	N-Vacancy	XPS, UV-vis DSR, AFM, ESR and PL	Extended visible light absorption and charge separation	RhB degradation	100 mg photocatalyst into 50 mL aqueous solution of RhB (5 mg·L^{-1})	18 W LED	Photocatalytic degradation of RhB by NVCN = 80% after 25 min irradiation	—	179
$DyVO_4$/nitrogen deficient g-C_3N_4 (DVO/CN*x*)	Precipitation-calcination method	N-Vacancy	XPS, UV-vis and PL	Improved visible light absorption and photocarriers separation	TC degradation	50 mg photocatalyst into 100 mL aqueous solution of TC (10 mg L^{-1})	300 W Xe lamp with 420 nm cut off filter	Photocatalytic degradation of TC by DVO/CN*x* = 92% after 1 h irradiation	—	180
Bi_2O_3 nanoparticles/2D g-C_3N_4	Hydrothermal method	N-Vacancy	XPS, FESEM, ESR, AFM and PL	Redshift in the visible light absorption edge	MB degradation	20 mg photocatalyst into 10 mL aqueous	18 W LED	Photocatalytic degradation of MB by 2BiON/CNN =	—	181

Table 2 (*Contd.*)

Sample	Designing strategy	Defect type	Characterisation	Mechanism	Application	Reaction conditions	Light source	Photoefficiency	AQE	Ref.
nanosheets (BiON/CNN)				and improved charge separation		solution of MB (10 mg L^{-1})		92% after 60 min irradiation		
Nitrogen-deficient GCN (CNK)	Hydrothermal followed by calcination	N-Vacancy	XPS, UV-vis DRS and PL	Broadening of visible light absorption with improved charge separation	RhB degradation	0.1 g catalyst sample into 100 mL of RhB solution (10 mg L^{-1})	300 W Xe lamp with 420 nm cutoff filter	Photocatalytic degradation of RhB by CNK0.01 = 100% after 30 min irradiation	—	182
N-Vacancy enriched g-C_3N_4 (DCN3-m)	One-step NaN_3-deflagration	N-Vacancy	XPS, EPR and DFT calculation	Broad optical absorption due to narrowed bandgap and efficient charge separation	RhB degradation	0.1 g catalyst into 300 mL RhB solution (50 mg L^{-1}, 50 ppm)	300 W Xe lamp with 420 nm optical filter	Photocatalytic degradation of RhB by DCN3-0.4 = 90% after 120 min irradiation	—	183
Flower-like GCN nanosheets (Fx)	Calcination	N-Vacancy	AFM, XPS and EPR	π–π layer stacking with breakage of H-bonds due to N-vacancy resulted in broad optical absorption and improved charge separation	NO removal	0.2 g of photocatalyst deposited on a glass dish and moved into a reactor, 1.01 min^{-1} flow rate of NO	150 W LED lamp with 400 nm cutoff filter	Photocatalytic removal of NO by F10 = 59.7%	—	184
Nitrogen-deficient GCN (FH-g-C_3N_4)	Liquid phase chemical reduction method	N-Vacancy	EA, EPR, XPS and EDS	Strong light absorption, more negative CB potential and a high reduction efficiency	Cr(VI) reduction and H_2 production	Cr(VI) reduction: $K_2Cr_2O_7$ solution (10 mg L^{-1} of Cr(VI)), 30 mg of photocatalyst added into 50 mL of Cr(VI) solution	Cr(VI) reduction: 400 W halide lamp (λ = 380–800 nm)	Photocatalytic Cr(VI) reduction by FH-g-C_3N_4 = 58% higher than H-g-C_3N_4	—	185
						H_2 production: 50 mg catalyst added into 80 mL of water containing 20 mL methanol and introduced into 250 mL reactor	H_2 production: 300 W Xe lamp	A photocatalytic H_2 production rate of HF-g-C_3N_4 = 1.323 mmol g^{-1} h^{-1}		
N-defects and K-modified g-C_3N_4	Thermal copolymerisation	N-Vacancy and K-doping	EA, EPR and XPS	Strong electron-withdrawing ability of N-defects and enhanced electron transport due to K-bridging	H_2O_2 production	30 mg of photocatalyst and 30 mL aqueous IPA solution (10 vol%) in 50 mL quartz tube at pH = 3	500 W xenon lamp and a cutoff filter	Rate of H_2O_2 production = 704 μM g^{-1} h^{-1}, 12 × unmodified g-C_3N_4	—	186

Table 2 (*Contd.*)

Sample	Designing strategy	Defect type	Characterisation	Mechanism	Application	Reaction conditions	Light source	Photoefficiency	AQE	Ref.
KOH modified GCN (CNK_x)	Thermal treatment in the presence of KOH	N-Vacancy	EA, EPR and XPS	Narrowed bandgap, negatively charged high specific surface area and improved charge separation	H_2O_2 production	0.1 g photocatalyst in methanol/water mixture (9/1 v/v, 100 mL) with 0.125 mmol DMPO	300 W xenon lamp with a 420 nm cutoff filter	Rate of H_2O_2 production = 101 μmol h^{-1}, 30 × unmodified g-C_3N_4	—	187

6. Summary and outlook

In the present review article, we have summarised the fundamentals of vacancy generation in GCN to manoeuvre its photocatalytic performance by highlighting distinct defect designing strategies and discussing the role of appropriate characterisation techniques to investigate their presence. Vacancy creation in GCN has conspicuously amended its photocatalytic performance by generating midgap states and altered its bandgap energy to store and convert photon energy with a long wavelength. As a result, the charge carrier kinetics in PCN is substantially modulated since vacancy defects serve as effective shallow capturing sites for photocarriers to foster charge isolation and migration. Of note, the 2D characteristic of GCN facilitates the creation of defect rich surfaces owing to relatively small surface escape energy and deprived bulk reassembly centres. Besides, vacancy creation can stimulate the introduction of both acceptor and donor sites leading to exceptional dissociation of photocarriers.

Despite various recent advances reviewed in this article, related research of vacancy defect induced GCN is still in an early stage surrounded by several opportunities and challenges in the field of fabrication, characterisation and implementation as discussed below:

(i) Rational construction of defects is a critical strategy which dramatically determines the synergism between different photocatalytic steps since the generation of defects can remarkably improve one step of photocatalysis and can hinder the other. Because the creation of defects is a double-edged sword, it becomes essential to select a synthesis method which synergistically balances the critical steps involving optical absorption, charge isolation and surface photoreactions. Thus, exploration of appropriate modifiers (preferably non-toxic and earth-abundant) with a facile and efficient tailoring approach for vacancy defect generation in GCN is highly anticipated.

(ii) Defect generation can significantly amend the charge migration efficacy but for spatial separation and superior redox ability of photocarriers, hybridising GCN with other semiconductor materials is highly recommended. By forming heterojunctions of vacancy defect modified GCN the challenge of mismatched energy levels and loose interface junctions can be overcome, which can expedite the space charge isolation phenomenon. However, there are very few reports which signify the generation of defects in GCN and its simultaneous coupling with appropriate semiconductor photocatalysts without affecting its properties. Precisely, current methods do not exhibit the controlled generation of defects in hybrid photocatalytic systems.

(iii) For an atomic level understanding and insight of the correlation between a generation of the defect along with its impact on photocatalytic behaviour, advanced characterisation techniques with *in situ* observations are required. Use of more appropriate characterisation tools with high spatial, spectral and temporal resolutions is highly desirable for developing an in-depth understanding of defects. For instance, the use of positron annihilation spectroscopy (PAS) provides the confirmation of position and concentration of defects along with distinction between surface and volume defects. On the other hand, time-resolved

photoluminescence spectroscopy (TRPLS) and transient absorption spectroscopy (TAS) examines the charge carrier kinetics while deep level transient spectrometry (DLTS) evaluates the atomic interface-state of defects.

(iv) Generally, vacancy defect generation with distinct morphologies of GCN leads to a substantially increased surface area, pore volume and exposed sites which can promote the surface adsorption/desorption kinetics of GCN. The modified molecular porous structure with vacancy defects can also expedite the most crucial step involving adsorption/activation of CO_2 and N_2 on the surface of GCN which can further be reduced by captured charge carriers at defective sites. However, in the case of photocatalytic environmental remediation, the adsorption of pollutants and degraded products could inactivate the catalytic sites. However, these issues could be overcome by designing dual-functional GCN photocatalysts with improved adsorption and photocatalytic ability. Thus, the significant role of morphology modulation and vacancy generation in GCN is worth exploring since the effect of adsorption/desorption kinetics is still not clear.

(v) So far, C/N vacancy induced GCN has been utilised for various environmental and energy applications. However, the role of a particular vacancy (C or N) generation in GCN for realising a specific application is still not described. For instance, surface carbon vacancy and ubiquitous amino group decorated GCN prompted CO_2 reduction kinetics due to superior adsorption of CO_2 and subsequent activation by surface-induced charge carriers. Similarly, generation of 2-fold coordinated N-vacancies with a corrugated structure not only activate $n \rightarrow \pi^*$ transitions causing a significant red-shift but also enhance the N_2 adsorption/activation kinetics resulting in improved photoactivity. Nevertheless, for the photocatalytic water splitting reaction, no such results have been exploited, and significantly less research work is carried out on C-vacancy modified GCN, which could be because of more structural deformations caused by C-vacancies. Thus, combining DFT calculation studies with the experimental examination to evaluate the effect of different vacancy generation in GCN for various photocatalytic applications can be a real breakthrough for achieving efficient photocatalytic performance.

Thus we believe this comprehensive study can stimulate more remarkable research efforts for the designing of more efficient defect rich metal-free GCN photocatalysts with broad research prospects for sustainable development.

Conflicts of interest

There are no conflicts to declare.

Abbreviations

AOP	Advanced oxidation process
AFM	Atomic force microscopy
BPA	Bisphenol A
CIP	Ciprofloxacin
CB	Conduction band
CBM	Conduction band minimum
DS	Defect states
DFT	Density functional theory
DBD	Dielectric barrier discharge
DRS	Diffusion reflectance spectroscopy
EPR	Electron paramagnetic resonance
e^-	Electrons
EA	Elemental analysis
FTIR	Fourier transformation infra-red
g-C_3N_4	GCN
HPHT	High pressure and high temperature
HOMO	Highest occupied molecular orbitals
h^+	Holes
$^{\bullet}OH$	Hydroxyl radicals
LSV	Linear sweep voltammetry
NPs	Nanoparticles
NCDs	N-Doped carbon quantum dots
NOR	Norfloxacin
PL	Peroxymonosulfate
PL	Photoluminescence
POM	Polyoxometalate
RhB	Rhodamine B
SEM	Scanning electron microscopy
STEM	Scanning transmission electron microscopy
SPV	Surface photovoltage
TA	Tartaric acid
TPD	Temperature-programmed desorption
TEM	Transmission electron microscopy
TEOA	Triethanolamine
VB	Valence band
XRD	X-ray diffraction
XPS	X-ray photoelectron spectroscopy

References

1 J. Kosco, M. Bidwell, H. Cha, T. Martin, C. T. Howells, M. Sachs, D. H. Anjum, S. Gonzalez Lopez, L. Zou, A. Wadsworth, W. Zhang, L. Zhang, J. Tellam, R. Sougrat, F. Laquai, D. M. DeLongchamp, J. R. Durrant and I. McCulloch, *Nat. Mater.*, 2020, **19**, 559–565, DOI: 10.1038/s41563-019-0591-1.

2 A. Kumar, P. Raizada, P. Singh, R. V. Saini, A. K. Saini and A. Hosseini-Bandegharaei, *Chem. Eng. J.*, 2020, **391**, 123496.

3 Y. Zhao, S. Zhang, R. Shi, G. I. N. Waterhouse, J. Tang and T. Zhang, *Mater. Today*, 2020, **34**, 78–91.

4 S. Sharma, V. Dutta, P. Singh, P. Raizada, A. Rahmani-Sani, A. Hosseini-Bandegharaei and V. K. Thakur, *J. Cleaner Prod.*, 2019, **228**, 755–769, DOI: 10.1016/j.jclepro.2019.04.292.

5 P. Thakur, P. Raizada, P. Singh, A. Kumar, A. A. P. Khan and A. M. Asiri, *Arabian J. Chem.*, 2020, DOI: 10.1016/j.arabjc.2020.04.026.

6 Y. Li, D. Zhang, X. Feng and Q. Xiang, *Chin. J. Catal.*, 2020, **41**, 21–30, DOI: 10.1016/S1872-2067(19)63427-3.

7 N. Chandel, K. Sharma, A. Sudhaik, P. Raizada, A. Hosseini-Bandegharaei, V. K. Thakur and P. Singh, *Arabian J. Chem.*, 2020, **13**, 4324–4340, DOI: 10.1016/j.arabjc.2019.08.005.

8 S. A. Sajjadi, A. Meknati, E. C. Lima, G. L. Dotto, D. I. Mendoza-Castillo, I. Anastopoulos, F. Alakhras, E. I. Unuabonah, P. Singh and A. H. Bandegharaei, *J. Environ. Manage.*, 2019, **236**, 34–44, DOI: 10.1016/j.jenvman.2019.01.087.
9 V. Dutta, S. Sharma, P. Raizada, A. Hosseini-Bandegharaei, J. Kaushal and P. Singh, *Mater. Lett.*, 2020, **270**, 127693, DOI: 10.1016/j.matlet.2020.127693.
10 L. Zhang, J. Ran, S. Z. Qiao and M. Jaroniec, *Chem. Soc. Rev.*, 2019, **48**, 5184–5206, DOI: 10.1039/C9CS00172G.
11 Q. Chen, H. Wang, Q. Luan, R. Duan, X. Cao, Y. Fang, D. Ma, R. Guan and X. Hu, *J. Hazard. Mater.*, 2020, **385**, 121527, DOI: 10.1016/j.jhazmat.2019.121527.
12 M. S. Nasir, G. Yang, I. Ayub, S. Wang, L. Wang, X. Wang, W. Yan, S. Peng and S. Ramakarishna, *Appl. Catal., B*, 2019, **257**, 117855.
13 X. Li, J. Xiong, X. Gao, J. Huang, Z. Feng, Z. Chen and Y. Zhu, *J. Alloys Compd.*, 2019, **802**, 196–209.
14 P. Singh, P. Shandilya, P. Raizada, A. Sudhaik, A. Rahmani-Sani and A. Hosseini-Bandegharaei, *Arabian J. Chem.*, 2020, **13**, 3498–3520, DOI: 10.1016/j.arabjc.2018.12.001.
15 K. Maeda, *J. Photochem. Photobiol., C*, 2011, **12**, 237–268, DOI: 10.1016/j.jphotochemrev.2011.07.001.
16 J. Ran, J. Zhang, J. Yu, M. Jaroniec and S. Z. Qiao, *Chem. Soc. Rev.*, 2014, **43**, 7787–7812, DOI: 10.1039/C3CS60425J.
17 X. Zhang, X. Yuan, L. Jiang, J. Zhang, H. Yu, H. Wang and G. Zeng, *Chem. Eng. J.*, 2020, **390**, 124475, DOI: 10.1016/j.cej.2020.124475.
18 D. Jamwal, G. Kaur, P. Raizada, P. Singh and P. Thakur, *J. Phy. Chem. C,*, 2015, **119**, 5062–5073, DOI: 10.1021/jp510428z.
19 P. Singh, B. Priya, P. Shandilya, P. Raizada, N. Singh, B. Pare and S. B. Jonnalagadda, *Arab J. Chem.*, 2019, **12**, 4627–4645, DOI: 10.1016/j.arabjc.2016.08.005.
20 P. Raizada, A. Sudhaik, S. Patial, V. Hasija, A. A. Parwaz Khan, P. Singh, S. Gautam, M. Kaur and V. H. Nguyen, *Arabian J. Chem.*, 2020, **13**(11), 8424–8457, DOI: 10.1016/j.arabjc.2020.06.031.
21 Y. Yu, C. Cao, W. Li, P. Li, J. Qu and W. Song, *Nano Res.*, 2012, **5**, 434–442.
22 X. Sun, X. Zhang and Y. Xie, *Matter*, 2020, **2**, 842–861.
23 S. Bai, N. Zhang, C. Gao and Y. Xiong, *Nano Energy*, 2018, **53**, 296–336, DOI: 10.1016/j.nanoen.2018.08.058.
24 B. Henkel, T. Neubert, S. Zabel, C. Lamprecht, C. Selhuber-Unkel, K. Rätzke, T. Strunskus, M. Vergöhl and F. Faupel, *Appl. Catal., B*, 2016, **180**, 362–371, DOI: 10.1016/j.apcatb.2015.06.041.
25 Y. Kang, Y. Yang, L. C. Yin, X. Kang, G. Liu and H. M. Cheng, *Adv. Mater.*, 2015, **27**, 4572–4577, DOI: 10.1002/adma.201501939.
26 Z. Li, C. Xiao, H. Zhu and Y. Xie, *J. Am. Chem. Soc.*, 2016, **138**, 14810–14819, DOI: 10.1021/jacs.6b08748.
27 T. Bora, P. Sathe, K. Laxman, S. Dobretsov and J. Dutta, *Catal. Today*, 2017, **284**, 11–18, DOI: 10.1016/j.cattod.2016.09.014.
28 J. Ding, W. Xu, H. Wan, D. Yuan, C. Chen, L. Wang, G. Guan and W. L. Dai, *Appl. Catal., B*, 2018, **221**, 626–634, DOI: 10.1016/j.apcatb.2017.09.048.
29 C. Mao, J. Wang, Y. Zou, H. Li, G. Zhan, J. Li, J. Zhao and L. Zhang, *Green Chem.*, 2019, **21**, 2852–2867, DOI: 10.1039/C9GC01010F.
30 E. Lira, S. Wendt, P. Huo, J. Hansen, R. Streber, S. Porsgaard, Y. Wei, R. Bechstein, E. Lægsgaard and F. Besenbacher, *J. Am. Chem. Soc.*, 2011, **133**, 6529–6532, DOI: 10.1021/ja200884w.
31 X. Hao, Y. Wang, J. Zhou, Z. Cui, Y. Wang and Z. Zou, *Appl. Catal., B*, 2018, **221**, 302–311, DOI: 10.1016/j.apcatb.2017.09.006.
32 F. Zuo, L. Wang, T. Wu, Z. Zhang, D. Borchardt and P. Feng, *J. Am. Chem. Soc.*, 2010, **132**, 11856–11857, DOI: 10.1021/ja103843d.
33 S. Wang, C. Y. Huang, L. Pan, Y. Chen, X. Zhang, Fazal-e-Aleem and J. J. Zou, *Catal. Today*, 2019, **335**, 151–159, DOI: 10.1016/j.cattod.2018.10.059.
34 B. Dong, T. Liu, C. Li and F. Zhang, *Chin. Chem. Lett.*, 2018, **29**, 671–680, DOI: 10.1016/j.cclet.2017.12.002.
35 G. Zhang, Z. Hu, M. Sun, Y. Liu, L. Liu, H. Liu, C. P. Huang, J. Qu and J. Li, *Adv. Funct. Mater.*, 2015, **25**, 3726–3734, DOI: 10.1002/adfm.201501009.
36 C. Lv, G. Chen, X. Zhou, C. Zhang, Z. Wang, B. Zhao and D. Li, *ACS Appl. Mater. Interfaces*, 2017, **9**, 23748–23755, DOI: 10.1021/acsami.7b05302.
37 P. Raizada, A. Sudhaik, P. Singh, A. Hosseini-Bandegharaei, V. K. Gupta and S. Agarwal, *Desalin. Water Treat.*, 2019, **171**, 344–355, DOI: 10.5004/dwt.2019.24774.
38 H. Gao, R. Cao, X. Xu, S. Zhang, H. Yongshun, H. Yang, X. Deng and J. Li, *Appl. Catal., B*, 2019, **245**, 399–409, DOI: 10.1016/j.apcatb.2019.01.004.
39 J. Liu, Y. Liu, N. Liu, Y. Han, X. Zhang, H. Huang, Y. Lifshitz, S. T. Lee, J. Zhong and Z. Kang, *Science*, 2015, **347**, 970–974, DOI: 10.1126/science.aaa3145.
40 C. Li, Y. Xu, W. Tu, G. Chen and R. Xu, *Green Chem.*, 2017, **19**, 882–899, DOI: 10.1039/C6GC02856J.
41 D. Masih, Y. Ma and S. Rohani, *Appl. Catal., B*, 2017, **206**, 556–588, DOI: 10.1016/j.apcatb.2017.01.061.
42 X. Wang, K. Maeda, A. Thomas, K. Takanabe, G. Xin, J. M. Carlsson, K. Domen and M. Antonietti, *Nat. Mater.*, 2009, **8**, 76–80, DOI: 10.1038/nmat2317.
43 P. Raizada, P. Thakur, A. Sudhaik, P. Singh, V. K. Thakur and A. Hosseini-Bandegharaei, *Arabian J. Chem.*, 2020, **13**, 4538–4552, DOI: 10.1016/j.arabjc.2019.10.001.
44 P. Raizada, A. Sudhaik, P. Singh, A. Hosseini-Bandegharaei and P. Thakur, *Sep. Purif. Technol.*, 2019, **227**, 115692, DOI: 10.1016/j.seppur.2019.115692.
45 V. Hasija, P. Raizada, A. Sudhaik, P. Singh, V. K. Thakur and A. A. P. Khan, *Solid State Sci.*, 2020, **100**, 106095, DOI: 10.1016/j.solidstatesciences.2019.106095.
46 Y. He, Y. Wang, L. Zhang, B. Teng and M. Fan, *Appl. Catal., B*, 2015, **168-169**, 1–8, DOI: 10.1016/j.apcatb.2014.12.017.
47 X. Bai, L. Wang, Y. Wang, W. Yao and Y. Zhu, *Appl. Catal., B*, 2014, **152-153**, 262–270, DOI: 10.1016/j.apcatb.2014.01.046.

48 A. Kumar, P. Raizada, P. Singh, A. Hosseini-Bandegharaei and V. K. Thakur, *J. Photochem. Photobiol., A*, 2020, **397**, 112588, DOI: 10.1016/j.jphotochem.2020.112588.
49 S. Cao and J. Yu, *J. Phys. Chem. Lett.*, 2014, **5**, 2101–2107, DOI: 10.1021/jz500546b.
50 V. Hasija, P. Raizada, A. Sudhaik, K. Sharma, A. Kumar, P. Singh, S. B. Jonnalagadda and V. K. Thakur, *Appl. Mater. Today*, 2019, **15**, 494–524, DOI: 10.1016/j.apmt.2019.04.003.
51 G. Liu, P. Niu, C. Sun, S. C. Smith, Z. Chen, G. Q. Lu and H. M. Cheng, *J. Am. Chem. Soc.*, 2010, **132**, 11642–11648, DOI: 10.1021/ja103798k.
52 H. Yu, R. Shi, Y. Zhao, T. Bian, Y. Zhao, C. Zhou, G. I. N. Waterhouse, L. Z. Wu, C. H. Tung and T. Zhang, *Adv. Mater.*, 2017, **29**, 1605148, DOI: 10.1002/adma.201605148.
53 X. Liu, B. Jing, G. Lun, Y. Wang, X. Wang, C. Fang, Z. Ao and C. Li, *Chem. Commun.*, 2020, **56**, 3179–3189, DOI: 10.1039/d0cc00280a.
54 Y. Sun, S. Gao, F. Lei and Y. Xie, *Chem. Soc. Rev.*, 2015, **44**, 623–636, DOI: 10.1039/C4CS00236A.
55 C. Ren, Y. Zhang, Y. Li, Y. Zhang, S. Huang, W. Lin and K. Ding, *J. Phy. Chem. C*, 2019, **123**, 17296–17305, DOI: 10.1021/acs.jpcc.9b03511.
56 H. Liu, S. Ma, L. Shao, H. Liu, Q. Gao, B. Li, H. Fu, S. Fu, H. Ye, F. Zhao and J. Zhou, *Appl. Catal., B*, 2020, **261**, 118201, DOI: 10.1016/j.apcatb.2019.118201.
57 Q. Liang, Z. Li, Z. Huang, F. Kang and Q. Yang, *Adv. Funct. Mater.*, 2015, 6885–6892, DOI: 10.1002/adfm.201503221.
58 J. Di, J. Xia, X. Li, M. Ji, H. Xu, Z. Chen and H. Li, *Carbon*, 2016, **107**, 1–10, DOI: 10.1016/j.carbon.2016.05.028.
59 X. Wang, L. Wu, Z. Wang, H. Wu, X. Zhou, H. Ma, H. Zhong, Z. Xing, G. Cai, C. Jiang and F. Ren, *Sol. RRL*, 2019, **12**, 1730–1750, DOI: 10.1002/solr.201800298.
60 J. Liu, W. Fang, Z. Wei, Z. Qin, Z. Jiang and W. Shangguan, *Appl. Catal., B*, 2018, **238**, 465–470, DOI: 10.1016/j.apcatb.2018.07.021.
61 X. Du, X. Bai, L. Xu, L. Yang and P. Jin, *Chem. Eng. J.*, 2020, **384**, 123245, DOI: 10.1016/j.cej.2019.123245.
62 Q. Wang, Y. Lei, D. Wang and Y. Li, *Energy Environ. Sci.*, 2019, **12**, 1730–1750.
63 J. Liu, Z. Wei and W. Shangguan, *ChemCatChem*, 2019, **11**, 6177–6189, DOI: 10.1002/cctc.201901579.
64 L. Ran, J. Hou, S. Cao, Z. Li, Y. Zhang, Y. Wu, B. Zhang, P. Zhai and L. Sun, *Sol. RRL*, 2020, **4**, 1900487, DOI: 10.1002/solr.201900487.
65 S. Bai, N. Zhang, C. Gao and Y. Xiong, *Nano Energy*, 2018, **53**, 296–336.
66 J. Xiong, J. Di, J. Xia, W. Zhu and H. Li, *Adv. Funct. Mater.*, 2018, **28**, 1801983, DOI: 10.1002/adfm.201801983.
67 N. Sun, Y. Liang, X. Ma and F. Chen, *Chem. Eur. J.*, 2017, **23**, 15466–15473, DOI: 10.1002/chem.201703168.
68 Y. Li, M. Gu, T. Shi, W. Cui, X. Zhang, F. Dong, J. Cheng, J. Fan and K. Lv, *Appl. Catal., B*, 2020, **262**, 118281, DOI: 10.1016/j.apcatb.2019.118281.
69 S. Li, G. Dong, R. Hailili, L. Yang, Y. Li, F. Wang, Y. Zeng and C. Wang, *Appl. Catal., B*, 2016, **190**, 26–35, DOI: 10.1016/j.apcatb.2016.03.004.
70 K. Chu, Q. qing Li, Y. ping Liu, J. Wang and Y. hua Cheng, *Appl. Catal., B*, 2020, **267**, 118693, DOI: 10.1016/j.apcatb.2020.118693.
71 H. Zhang and A. Yu, *J. Phys. Chem. C*, 2014, **118**(22), 11628–11635, DOI: 10.1021/jp503477x.
72 Y. Zhang, J. Gao and Z. Chen, *J. Colloid Interface Sci.*, 2019, **535**, 331–340, DOI: 10.1016/j.jcis.2018.10.012.
73 G. Zhang, G. Li, Z. A. Lan, L. Lin, A. Savateev, T. Heil, S. Zafeiratos, X. Wang and M. Antonietti, *Angew. Chem., Int. Ed.*, 2017, **129**, 13630–13634, DOI: 10.1002/anie.201706870.
74 H. Shi, S. Long, J. Hou, L. Ye, Y. Sun, W. Ni, C. Song, K. Li, G. G. Gurzadyan and X. Guo, *Chem.–Eur. J.*, 2019, **25**, 5028–5035, DOI: 10.1002/chem.201805923.
75 C. Q. Xu, K. Li and W. De Zhang, *J. Colloid Interface Sci.*, 2017, **495**, 27–36, DOI: 10.1016/j.jcis.2017.01.111.
76 M. Wu, X. He, B. Jing, T. Wang, C. Wang, Y. Qin, Z. Ao, S. Wang and T. An, *J. Hazard. Mater.*, 2020, **384**, 121323, DOI: 10.1016/j.jhazmat.2019.121323.
77 J. Wang, B. Gao, M. Dou, X. Huang and Z. Ma, *Environ. Res.*, 2020, **184**, 109339, DOI: 10.1016/j.envres.2020.109339.
78 W. Lin, K. Lu, S. Zhou, J. Wang, F. Mu, Y. Wang, Y. Wu and Y. Kong, *Appl. Surf. Sci.*, 2019, **474**, 194–202, DOI: 10.1016/j.apsusc.2018.03.140.
79 Y. Jiang, Z. Sun, C. Tang, Y. Zhou, L. Zeng and L. Huang, *Appl. Catal., B*, 2019, **240**, 30–38, DOI: 10.1016/j.apcatb.2018.08.059.
80 G. Xu, J. Shen, S. Chen, Y. Gao, H. Zhang and J. Zhang, *Phys. Chem. Chem. Phys.*, 2018, **20**, 17471–17476, DOI: 10.1039/c8cp01986j.
81 Z. Zhou, K. Li, W. Deng, J. Li, Y. Yan, Y. Li, X. Quan and T. Wang, *J. Hazard. Mater.*, 2020, **387**, 122023, DOI: 10.1016/j.jhazmat.2020.122023.
82 Y. Liu, X. Guo, Z. Chen, W. Zhang, Y. X. Wang, Y. Zheng, X. Tang, M. Zhang, Z. Peng, R. Li and Y. Huang, *Appl. Catal., B*, 2020, **261**, 118624, DOI: 10.1016/j.apcatb.2020.118624.
83 S. L. James, C. J. Adams, C. Bolm, D. Braga, P. Collier, T. Friić, F. Grepioni, K. D. M. Harris, G. Hyett, W. Jones, A. Krebs, J. MacK, L. Maini, A. G. Orpen, I. P. Parkin, W. C. Shearouse, J. W. Steed and D. C. Waddell, *Chem. Soc. Rev.*, 2012, **41**, 413–447, DOI: 10.1039/C1CS15171A.
84 S. Bai, J. Jiang, Q. Zhang and Y. Xiong, *Chem. Soc. Rev.*, 2015, **44**, 2893–2939, DOI: 10.1039/c5cs00064e.
85 W. Shi, K. Shu, X. Huang, H. Ren, M. Li, F. Chen and F. Guo, *J. Chem. Technol. Biotechnol.*, 2020, **95**, 1476–1486, DOI: 10.1002/jctb.6338.
86 Y. Li, W. Ho, K. Lv, B. Zhu and S. C. Lee, *Appl. Surf. Sci.*, 2018, **430**, 380–389, DOI: 10.1016/j.apsusc.2017.06.054.
87 R. Mo, J. Li, Y. Tang, H. Li and J. Zhong, *Appl. Surf. Sci.*, 2019, **476**, 552–559, DOI: 10.1016/j.apsusc.2019.01.085.
88 X. Liu, W. Kang, W. Zeng, Y. Zhang, L. Qi, F. Ling, L. Fang, Q. Chen and M. Zhou, *Appl. Surf. Sci.*, 2020, **499**, 143994, DOI: 10.1016/j.apsusc.2019.143994.

89 H. Che, G. Che, P. Zhou, C. Liu, H. Dong, C. Li, N. Song and C. Li, *Chem. Eng. J.*, 2020, **382**, 122870, DOI: 10.1016/j.cej.2019.122870.
90 K. Sharma, V. Dutta, S. Sharma, P. Raizada, A. Hosseini-Bandegharaei, P. Thakur and P. Singh, *J. Ind. Eng. Chem.*, 2019, **78**, 1–20, DOI: 10.1016/j.jiec.2019.06.022.
91 Y. Li, M. Zhou, B. Cheng and Y. Shao, *J. Mater. Sci. Technol.*, 2020, **56**, 1–17, DOI: 10.1016/j.jmst.2020.04.028.
92 X. Pan, M. Q. Yang, X. Fu, N. Zhang and Y. J. Xu, *Nanoscale*, 2013, **5**, 3601–3614, DOI: 10.1039/C3NR00476G.
93 Z. Yang, D. Chu, G. Jia, M. Yao and B. Liu, *Appl. Surf. Sci.*, 2020, **504**, 144407, DOI: 10.1016/j.apsusc.2019.144407.
94 D. Zhao, C. L. Dong, B. Wang, C. Chen, Y. C. Huang, Z. Diao, S. Li, L. Guo and S. Shen, *Adv. Mater.*, 2019, **31**, 1903545, DOI: 10.1002/adma.201903545.
95 W. Iqbal, B. Yang, X. Zhao, M. Rauf, I. M. A. Mohamed, J. Zhang and Y. Mao, *Catal. Sci. Technol.*, 2020, **10**, 549–559, DOI: 10.1039/c9cy02111f.
96 H. Yaghoubi, Z. Li, Y. Chen, H. T. Ngo, V. R. Bhethanabotla, B. Joseph, S. Ma, R. Schlaf and A. Takshi, *ACS Catal.*, 2015, **5**, 327–335, DOI: 10.1021/cs501539q.
97 P. Raizada, A. Aslam Parwaz Khan and P. Singh, *Sep. Purif. Technol.*, 2020, **247**, 116957, DOI: 10.1016/j.seppur.2020.116957.
98 J. Fu, J. Yu, C. Jiang and B. Cheng, *Adv. Energy Mater.*, 2018, **8**, 1701503.
99 S. Ould-Chikh, O. Proux, P. Afanasiev, L. Khrouz, M. N. Hedhili, D. H. Anjum, M. Harb, C. Geantet, J. M. Basset and E. Puzenat, *ChemSusChem*, 2014, **7**, 1361–1371, DOI: 10.1002/cssc.201300922.
100 Y. Xue, Y. Guo, Z. Liang, H. Cui and J. Tian, *J. Colloid Interface Sci.*, 2019, **556**, 206–213, DOI: 10.1016/j.jcis.2019.08.067.
101 J. Liao, W. Cui, J. Li, J. Sheng, H. Wang, X. Dong, P. Chen, G. Jiang, Z. Wang and F. Dong, *Chem. Eng. J.*, 2020, **379**, 122282, DOI: 10.1016/j.cej.2019.122282.
102 F. Niu, L. S. Zhang, C. Q. Chen, W. Li, L. Li, W. G. Song and L. Jiang, *Nanoscale*, 2010, **2**, 1480–1484, DOI: 10.1039/C0NR00182A.
103 F. Song, W. Li and Y. Sun, *Inorganics*, 2017, **5**, 40, DOI: 10.3390/inorganics5030040.
104 Q. Tay, X. Wang, X. Zhao, J. Hong, Q. Zhang, R. Xu and Z. Chen, *J. Catal.*, 2016, **342**, 55–62, DOI: 10.1016/j.jcat.2016.07.007.
105 C. Nguyen, M. Sakar, M. Vu and T. Do, *Ind. Eng. Chem. Res.*, 2019, **58**, 3698–3706, DOI: 10.1021/acs.iecr.8b05792.
106 X. Li, W. Zhang, J. Li, G. Jiang, Y. Zhou, S. C. Lee and F. Dong, *Appl. Catal., B*, 2019, **241**, 187–195, DOI: 10.1016/j.apcatb.2018.09.032.
107 N. M. Nursam, J. Z. Y. Tan, X. Wang, W. Li, F. Xia and R. A. Caruso, *ChemistrySelect*, 2016, **1**, 4868–4878.
108 J. H. Pan, Z. Jiang and D. W. Bahnemann, *Catal. Today*, 2019, **335**, 1–2.
109 F. Liu, Y. H. Leung, A. B. Djurišić, A. M. C. Ng and W. K. Chan, *J. Phys. Chem. C*, 2013, **117**, 12218–12228, DOI: 10.1021/jp403478q.
110 L. Liu, C. Zhao and Y. Li, *J. Phys. Chem. C*, 2012, **116**, 7904–7912, DOI: 10.1021/jp300932b.
111 H. Li, J. Shang, H. Zhu, Z. Yang, Z. Ai and L. Zhang, *ACS Catal.*, 2016, **6**, 8276–8285, DOI: 10.1021/acscatal.6b02613.
112 L. Liang, L. Shi, F. Wang, L. Yao, Y. Zhang and W. Qi, *Int. J. Hydrogen Energy*, 2019, **44**, 16315–16326, DOI: 10.1016/j.ijhydene.2019.05.001.
113 S. Cao, B. Fan, Y. Feng, H. Chen, F. Jiang and X. Wang, *Chem. Eng. J.*, 2018, **353**, 147–156.
114 S. Bai, W. Yin, L. Wang, Z. Li and Y. Xiong, *RSC Adv.*, 2016, **6**, 57446–57463, DOI: 10.1039/C6RA10539D.
115 N. Jiang, L. Lyu, G. Yu, L. Zhang and C. Hu, *J. Mater. Chem. A*, 2018, **6**, 17819–17828, DOI: 10.1039/c8ta04873h.
116 H. Liu, J. Liang, S. Fu, L. Li, J. Cui, P. Gao, F. Zhao and J. Zhou, *Colloids Surf. A Physicochem. Eng. Asp.*, 2020, **591**, 124552, DOI: 10.1016/j.colsurfa.2020.124552.
117 A. Fujishima and K. Honda, *Nature*, 1972, **238**, 37–38, DOI: 10.1038/238037a0.
118 S. Ye, R. Wang, M. Z. Wu and Y. P. Yuan, *Appl. Surf. Sci.*, 2015, 15–27, DOI: 10.1016/j.apsusc.2015.08.173.
119 M. Wang, H. Liu, J. Ma and G. Lu, *Appl. Catal., B*, 2020, **266**, 118647, DOI: 10.1016/j.apcatb.2020.118647.
120 R. C. Dante, *Int. J. Hydrogen Energy*, 2019, **44**, 21030–21036.
121 L. Yuan, C. Han, M. Q. Yang and Y. J. Xu, *Int. Rev. Phys. Chem.*, 2016, **35**, 1–36, DOI: 10.1080/0144235X.2015.1127027.
122 X. Shan, G. Ge and Z. Zhao, *ChemCatChem*, 2019, **11**, 1534–1544, DOI: 10.1002/cctc.201801803.
123 P. Wu, J. Wang, J. Zhao, L. Guo and F. E. Osterloh, *J. Mater. Chem. A*, 2014, **2**, 20338–20344, DOI: 10.1039/c4ta04100c.
124 Y. Wang, S. Zhao, Y. Zhang, J. Fang, W. Chen, S. Yuan and Y. Zhou, *ACS Sustainable Chem. Eng.*, 2017, **5**, 9614–9618, DOI: 10.1021/acssuschemeng.8b01499.
125 X. Wang, Q. Li, L. Gan, X. Ji, F. Chen, X. Peng and R. Zhang, *J. Energy Chem.*, 2021, **53**, 139–146, DOI: 10.1016/j.jechem.2020.05.001.
126 S. Guo, Y. Tang, Y. Xie, C. Tian, Q. Feng, W. Zhou and B. Jiang, *Appl. Catal., B*, 2017, **218**, 664–671, DOI: 10.1016/j.apcatb.2017.07.022.
127 D. Li, M. Kassymova, X. Cai, S. Q. Zang and H. L. Jiang, *Coord. Chem. Rev.*, 2020, **412**, 213262, DOI: 10.1016/j.ccr.2020.213262.
128 Y. Bo, C. Gao and Y. Xiong, *Nanoscale*, 2020, **12**, 12196–12209, DOI: 10.1039/D0NR02596H.
129 W. Zhang, A. R. Mohamed and W.-J. Ong, *Angew. Chem., Int. Ed.*, DOI: 10.1002/anie.201914925.
130 P. Raizada, A. Kumar, V. Hasija, P. Singh, V. K. Thakur and A. A. P. Khan, *J. Ind. Eng. Chem.*, 2020, **93**, 1–27, DOI: 10.1016/j.jiec.2020.09.006.
131 M. Khalil, J. Gunlazuardi, T. A. Ivandini and A. Umar, *Renewable Sustainable Energy Rev.*, 2019, **113**, 109246.
132 Z. Sun, H. Wang, Z. Wu and L. Wang, *Catal. Today*, 2018, **300**, 160–172, DOI: 10.1016/j.cattod.2017.05.033.
133 J. Y. Tang, X. Y. Kong, B. J. Ng, Y. H. Chew, A. R. Mohamed and S. P. Chai, *Catal. Sci. Technol.*, 2019, **9**, 2335–2343, DOI: 10.1039/c9cy00449a.
134 K. Wang, J. Fu and Y. Zheng, *Appl. Catal., B*, 2019, **254**, 270–282, DOI: 10.1016/j.apcatb.2019.05.002.

135 H. Shi, S. Long, J. Hou, L. Ye, Y. Sun, W. Ni, C. Song, K. Li, G. G. Gurzadyan and X. Guo, *Chem.–Eur. J.*, 2019, **25**, 5028–5035.
136 W. Ma, N. Wang, Y. Guo, L. Yang, M. Lv, X. Tang and S. Li, *Chem. Eng. J.*, 2020, **388**, 124288, DOI: 10.1016/j.cej.2020.124288.
137 M. Shen, L. Zhang, M. Wang, J. Tian, X. Jin, L. Guo, L. Wang and J. Shi, *J. Mater. Chem. A*, 2019, **7**, 1556–1563.
138 Z. Sun, S. Wang, Q. Li, M. Lyu, T. Butburee, B. Luo, H. Wang, J. M. T. A. Fischer, C. Zhang, Z. Wu and L. Wang, *Adv. Sustainable Syst.*, 2017, **1**, 1700003, DOI: 10.1002/adsu.201700003.
139 X. Xue, R. Chen, C. Yan, P. Zhao, Y. Hu, W. Zhang, S. Yang and Z. Jin, *Nano Res.*, 2019, **12**, 1229–1249, DOI: 10.1007/s12274-018-2268-5.
140 Y. Zhao, Y. Zhao, G. I. N. Waterhouse, L. Zheng, X. Cao, F. Teng, L. Z. Wu, C. H. Tung, D. O'Hare and T. Zhang, *Adv. Mater.*, 2017, **29**, 1703828, DOI: 10.1002/adma.201703828.
141 M. Li, H. Huang, J. Low, C. Gao, R. Long and Y. Xiong, *Small Methods*, 2019, **3**, 1800388, DOI: 10.1002/smtd.201800388.
142 H. Li, C. Mao, H. Shang, Z. Yang, Z. Ai and L. Zhang, *Nanoscale*, 2018, **10**, 15429–15435, DOI: 10.1039/C8NR04277B.
143 X. Chen, N. Li, Z. Kong, W. J. Ong and X. Zhao, *Mater. Horiz.*, 2018, **5**, 9–27, DOI: 10.1039/C7MH00557A.
144 X. H. Li, W. L. Chen, P. He, T. Wang, D. Liu, Y. W. Li, Y. G. Li and E. B. Wang, *Inorg. Chem. Front.*, 2019, **6**, 3315–3326, DOI: 10.1039/c9qi01093a.
145 J. Ge, L. Zhang, J. Xu, Y. Liu, D. Jiang and P. Du, *Chin. Chem. Lett.*, 2020, **31**, 792–796, DOI: 10.1016/j.cclet.2019.05.030.
146 G. Dong, W. Ho and C. Wang, *J. Mater. Chem. A*, 2015, **3**, 23435–23441, DOI: 10.1039/c5ta06540b.
147 Y. Zhang, J. Di, P. Ding, J. Zhao, K. Gu, X. Chen, C. Yan, S. Yin, J. Xia and H. Li, *J. Colloid Interface Sci.*, 2019, **553**, 530–539, DOI: 10.1016/j.jcis.2019.06.012.
148 P. T. Lum, K. Y. Foo, N. A. Zakaria and P. Palaniandy, *Mater. Chem. Phys.*, 2020, **241**, 122405, DOI: 10.1016/j.matchemphys.2019.122405.
149 B. Pare, P. Singh and S. B. Jonnalgadda, *J. Sci. Ind. Res.*, 2009, **68[2009]**, 724–729, DOI: nopr.niscair.res.in/handle/123456789/5300.
150 V. Hasija, P. Raizada, A. Hosseini-Bandegharaei, P. Singh and V. H. Nguyen, *Top. Catal.*, 2020, **63**, 1030–1045, DOI: 10.1007/s11244-020-01359-z.
151 A. Sudhaik, P. Raizada, S. Thakur, A. K. Saini, P. Singh, A. Hosseini-Bandegharaei, J. H. Lim, D. Y. Jeong and V. H. Nguyen, *Appl. Nanosci.*, 2020, **10**, 4115–4137, DOI: 10.1007/s13204-020-01529-1.
152 A. Sudhaik, P. Raizada, S. Thakur, R. V. Saini, A. K. Saini, P. Singh, V. Kumar Thakur, V. H. Nguyen, A. A. P. Khan and A. M. Asiri, *J. Taiwan Inst. Chem. Eng.*, 2020, **113**, 142–154, DOI: 10.1016/j.jtice.2020.08.003.
153 U. I. Gaya and A. H. Abdullah, *J. Photochem. Photobiol., C*, 2008, **9**, 1–12, DOI: 10.1016/j.jphotochemrev.2007.12.003.
154 D. Chen, Y. Cheng, N. Zhou, P. Chen, Y. Wang, K. Li, S. Huo, P. Cheng, P. Peng, R. Zhang, L. Wang, H. Liu, Y. Liu and R. Ruan, *J. Cleaner Prod.*, 2020, **268**, 121725, DOI: 10.1016/j.jclepro.2020.121725.
155 Y. Yang, H. Jin, C. Zhang, H. Gan, F. Yi and H. Wang, *J. Alloy Compd.*, 2020, **821**, 153439, DOI: 10.1016/j.jallcom.2019.153439.
156 H. Zhang, W. Wu, Y. Li, Y. Wang, C. Zhang, W. Zhang, L. Wang and L. Niu, *Appl. Surf. Sci.*, 2019, **465**, 450–458, DOI: 10.1016/j.apsusc.2018.09.183.
157 Y. Huang, Y. Liang, Y. Rao, D. Zhu, J. J. Cao, Z. Shen, W. Ho and S. C. Lee, *Environ. Sci. Technol.*, 2017, **51**, 2924–2933, DOI: 10.1021/acs.est.6b04460.
158 Z. Wang, S. Yan, Y. Sun, T. Xiong, F. Dong and W. Zhang, *Appl. Catal., B*, 2017, **214**, 148–157, DOI: 10.1016/j.apcatb.2017.05.040.
159 Z. Wang, Y. Huang, M. Chen, X. Shi, Y. Zhang, J. Cao, W. Ho and S. C. Lee, *ACS Appl. Mater. Interfaces*, 2019, **11**, 10651–10662, DOI: 10.1021/acsami.8b21987.
160 J. Liao, W. Cui, J. Li, J. Sheng, H. Wang, P. Chen, G. Jiang, Z. Wang and F. Dong, *Chem. Eng. J.*, 2020, **379**, 122282, DOI: 10.1016/j.cej.2019.122282.
161 J. Di, J. Xia, X. Li, M. Ji, H. Xu, Z. Chen and H. Li, *Carbon*, 2016, **107**, 1–10, DOI: 10.1016/j.carbon.2016.05.028.
162 X. Liang, G. Wang, X. Dong, G. Wang, H. Ma and X. Zhang, *ACS Appl. Nano Mater.*, 2019, **2**, 517–524, DOI: 10.1021/acsanm.8b02089.
163 Y. Cui, Z. Ding, P. Liu, M. Antonietti, X. Fu and X. Wang, *Phys. Chem. Chem. Phys.*, 2012, **14**, 1455–1462, DOI: 10.1039/c1cp22820j.
164 C. Prat, M. Vicente and S. Esplugas, *Water Res.*, 1988, **22**, 663–668, DOI: 10.1016/0043-1354(88)90176-5.
165 R. Hage and A. Lienke, *Angew. Chem., Int. Ed.*, 2006, **45**, 206–222, DOI: 10.1002/anie.200500525.
166 V. R. Choudhary, A. G. Gaikwad and S. D. Sansare, *Angew. Chem., Int. Ed.*, 2001, **40**, 763–766, DOI: 10.1002/1521-3773(20010504)40:9<1776::AID-ANIE17760>3.0.CO;2-C.
167 X. Li, J. Zhang, F. Zhou, H. Zhang, J. Bai, Y. Wang and H. Wang, *Chin. J. Catal.*, 2018, **39**, 1090–1098, DOI: 10.1016/S1872-2067(18)63046-3.
168 Q. Tay, P. Kanhere, C. F. Ng, S. Chen, S. Chakraborty, A. C. H. Huan, T. C. Sum, R. Ahuja and Z. Chen, *Chem. Mater.*, 2015, **27**, 4930–4933, DOI: 10.1021/acs.chemmater.5b02344.
169 D. Ruan, S. Kim, M. Fujitsuka and T. Majima, *Appl. Catal., B*, 2018, **238**, 638–646, DOI: 10.1016/j.apcatb.2018.07.028.
170 X. Shan, G. Ge and Z. Zhao, *Energy Technol.*, 2019, **7**, 1800886, DOI: 10.1002/ente.201800886.
171 M. Wu, Y. Gong, T. Nie, J. Zhang, R. Wang, H. Wang and B. He, *J. Mater. Chem. A*, 2019, **7**, 5324–5332, DOI: 10.1039/c8ta12076e.
172 Z. Hong, B. Shen, Y. Chen, B. Lin and B. Gao, *J. Mater. Chem. A*, 2013, **1**, 11754–11761, DOI: 10.1039/c3ta12332d.
173 P. Niu, M. Qiao, Y. Li, L. Huang and T. Zhai, *Nano Energy*, 2018, **44**, 73–81, DOI: 10.1016/j.nanoen.2017.11.059.
174 Q. Zeng, X. Wang, M. Jin, E. M. Akinoglu, G. Zhou and L. Shui, *J. Colloid Interface Sci.*, 2020, **578**, 788–795, DOI: 10.1016/j.jcis.2020.06.023.

175 G. Dong, Y. Wen, H. Fan, C. Wang, Z. Cheng, M. Zhang, J. Ma and S. Zhang, *RSC Adv.*, 2020, **10**, 18632–18638, DOI: 10.1039/d0ra01425g.
176 X. Bai, X. Wang, X. Lu, Y. Liang, J. Li, L. Wu, H. Li, Q. Hao, B. J. Ni and C. Wang, *J. Hazard. Mater.*, 2020, **398**, 122897, DOI: 10.1016/j.jhazmat.2020.122897.
177 X. Jin, Y. Wu, Q. Zhang, F. Wang, P. Chen, H. Liu, S. Huang, J. Wu, N. Tu, W. Lv and G. Liu, *Chemosphere*, 2020, **258**, 127343, DOI: 10.1016/j.chemosphere.2020.127343.
178 Y. Gao, S. Liu, Y. Wang, P. Zhao, K. Li, J. He and S. Liu, *J. Colloid Interface Sci.*, 2020, **579**, 177–185, DOI: 10.1016/j.jcis.2020.06.018.
179 U. Ghosh and A. Pal, *J. Photochem. Photobiol., A*, 2020, **397**, 112582, DOI: 10.1016/j.jphotochem.2020.112582.
180 K. Shu, F. Chen, W. Shi, F. Guo, Y. Tang, H. Ren and M. Li, 2020, **124**, 1–9.
181 U. Ghosh and A. Pal, *Appl. Surf. Sci.*, 2020, **507**, 144965, DOI: 10.1016/j.apsusc.2019.144965.
182 H. G. Zhang, L. J. Feng, C. H. Li and L. Wang, *J. Fuel Chem. Technol.*, 2018, **46**, 871–878, DOI: 10.1016/s1872-5813(18)30036-7.
183 J. Tang, Y. Liu, Y. Hu, J. Huang, B. Wang, C. Yang and G. Yang, *J. Power Sources*, 2019, **434**, 226731, DOI: 10.1016/j.jpowsour.2019.226731.
184 Y. Duan, X. Li, K. Lv, L. Zhao and Y. Liu, *Appl. Surf. Sci.*, 2019, **492**, 166–176, DOI: 10.1016/j.apsusc.2019.06.125.
185 X. Ma, Z. Zhang, C. Yu, Q. Fan and L. Wei, *Mater. Res. Bull.*, 2020, **129**, 110909, DOI: 10.1016/j.materresbull.2020.110909.
186 H. Zhang, L. Jia, P. Wu, R. Xu, J. He and W. Jiang, *Appl. Surf. Sci.*, 2020, **527**, 146584, DOI: 10.1016/j.apsusc.2020.146584.
187 Y. Wang, D. Meng and X. Zhao, *Appl. Catal., B*, 2020, **273**, 119064, DOI: 10.1016/j.apcatb.2020.119064.